LANGMUIR PROBE MEASUREMENTS IN THE IONOSPHERE

by

Aroh Barjatya

A dissertation submitted in partial fulfillment
of the requirements for the degree

of

DOCTOR OF PHILOSOPHY

in

Electrical Engineering

Approved:

Dr. Charles M. Swenson Major Professor	Dr. Gardiner S. Stiles Committee Member
Dr. Bela G. Fejer Committee Member	Dr. Todd Moon Committee Member
Dr. Edmund A. Spencer Committee Member	Dr. Byron R. Burnham Dean of Graduate Studies

UTAH STATE UNIVERSITY
Logan, Utah

2007

Abstract

Langmuir Probe Measurements in the Ionosphere

by

Aroh Barjatya, Doctor of Philosophy

Utah State University, 2007

Major Professor: Dr. Charles M. Swenson
Department: Electrical and Computer Engineering

Electric probes have been the primary instruments for the in situ investigation of plasma parameters in the Earth's ionosphere. This dissertation is a compendium of three papers, each dealing with a separate spacecraft that carried one or more instruments based on the electric probe technique.

The first paper presents data from the Sudden Atom Layer sounding rocket that carried an RF Impedance Probe, a DC fixed-bias Langmuir Probe (DCP), and an Electric Field Probe. The combined dataset indicates a case of payload surface charging, the causes of which are investigated within the paper. A generic circuit model is developed to analyze payload charging and behavior of Langmuir-type instruments. Our analysis indicates that the anomalous charging event was an outcome of triboelectrification of the payload surface from neutral dust particles present in the Earth's mesosphere. These results suggest caution in interpreting observations from the Langmuir class of instrumentation within dusty environments.

The second paper presents data from the Floating Potential Measurement Unit (FPMU) that is deployed on the International Space Station. The FPMU instrument suite consists of three different Langmuir-type probes and a Plasma Impedance Probe (PIP). We first give a

brief overview of the instrumentation, and then describe the algorithm used to reduce Langmuir probe I-V curves to plasma parameters. It is shown that the derived temperatures agree well with International Reference Ionosphere (IRI) model, while the derived density matches better with the USU-Global Assimilation of Ionospheric Measurement model.

The third paper presents the dataset from the EQUIS II sounding rocket campaign. The rocket payloads carried a PIP, a DCP, and an internally heated Sweeping Langmuir Probe. The ratio of the payload surface area to the cumulative area of the instrument and its guard was about 250. We show that on small sounding rocket payloads the DCP technique of relative electron density measurement is not very accurate. We further show that the ion saturation region analysis of the I-V curve produces absolute ion density that matches very well with the absolute electron density derived from the PIP, and the derived temperatures agree reasonably well with the IRI model.

(123 pages)

To my father Ashok and mother Rajeshwari, and especially to my little sister Apurva.

Acknowledgments

I first and foremost thank my advisor, Dr. Charles M. Swenson. I will forever be indebted to him for having taken the pains of working with a foreign student. My educational journey under his supervision has been a multifaceted adventure. Having no solitary project to fund my graduate studies at Utah State, he gave me the opportunity and guidance to work on several different projects. He has not only mentored me in several aspects of engineering and space physics, but most importantly in "looking at the big picture."

I am also indebted to several people whom I have closely worked with over the past several years. In particular, I would like to thank Wayne Sanderson and Chad Fish who have suffered my ignorant questions and patiently helped me through all three projects that make up my dissertation. I would also like to thank several of my student colleagues and friends: Prashanth Gujjeti, Jeff Ward, Albert Hummel, Tim Campbell, and Sid Henderson. They have been my sounding boards and provided a constant voice of sanity. I am grateful to Dr. Kenneth H. Wright from the University of Alabama in Huntsville who provided the FPMU dataset and has been a helpful source of insight during FPMU data analysis.

I also acknowledge the contribution of the faculty and staff of the ECE Department, and the employees of Space Dynamics Laboratory and USU Center for Space Engineering. They have all helped enhance my experience as a graduate student. I give particular thanks to my PhD committee, especially to Dr. Bela Fejer from the Physics Department.

Finally, I would not have survived graduate school were it not for the constant support of my family and their faith in my abilities. While my father has been the infinite source of philosophy, my mother has kept me rooted in reality, and it has been my sister who has always made me look at the perky side of life when the graduate student life got monotonous and depressing. To them I dedicate my thesis.

Aroh Barjatya

Contents

List of Tables

List of Figures

Chapter 1

Introduction

The development of radio in the early 20^{th} century led to the discovery of a conducting region in the Earth's atmosphere that reflected radio waves. This region the lies roughly between 80 km to 1000 km is now known to be ionized gas, a plasma, and is referred to as the ionosphere [1, 2]. This plasma results from photoionization of the neutral atmosphere by ultraviolet, x-ray, and other short wavelength radiation from the Sun. Its production within this altitude range is in equilibrium with electron-ion recombination and diffusive transport. For lower altitudes the loss processes dominate due to higher neutral particle density, and thus little plasma exists below about 60 km.

Figure 1.1 shows typical mid-latitude daytime and nighttime electron density profiles during solar maximum and minimum conditions. The data was generated using the International Reference Ionosphere (IRI) model calculated over Logan, Utah (Lat. 41 44' 7", Lon. -111 50' 3"). Figure 1.2 shows the IRI model temperature for electrons, ions, and neutrals. The ionosphere can be thought of as being composed of a series of overlapping layers in altitude, with each layer having an altitude of maximum density. These various regions differ in their primary ion constituents and absorbed UV wavelengths. The D-region is predominant in hydrated ions, the E-region in NO^+ and O_2^+, and the F-region in O^+. The D-region does not exist at night due to absence of solar ionization. The ionospheric density and temperature profiles differ with latitude, longitude, and season due to variation in zenith angle of the incident UV and the Earth's geomagnetic field.

Ionospheric models like the IRI only provide average climatologies of the ionosphere parameterized by solar activity, season, and geomagnetic activity indices. The actual day-to-day variability of the ionosphere in geomagnetically quiet conditions can approach up to 30% of the model provided averages [3], and becomes worse for geomagnetically disturbed

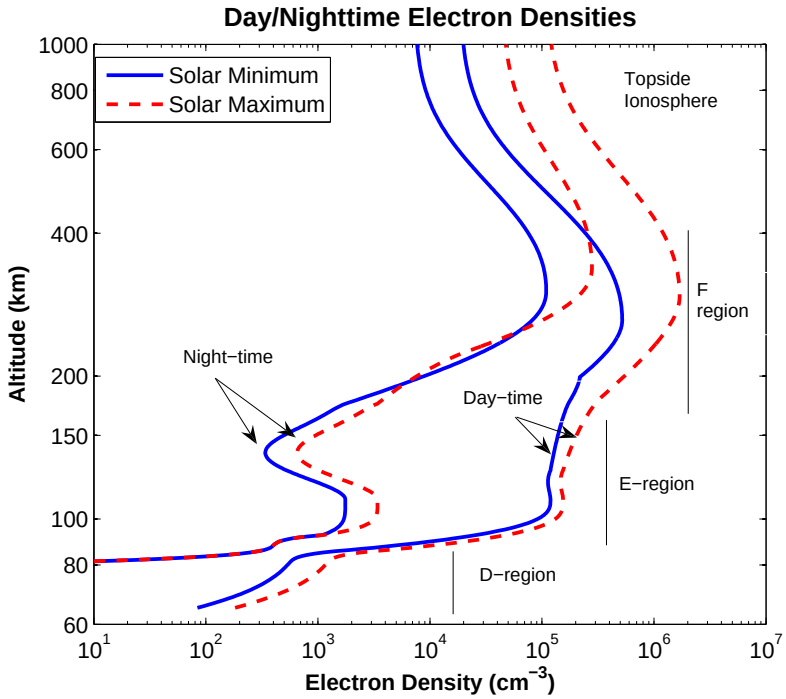

Fig. 1.1: Typical mid-latitude daytime and nighttime electron density profiles showing the D-, E-, and F-regions of the ionosphere.

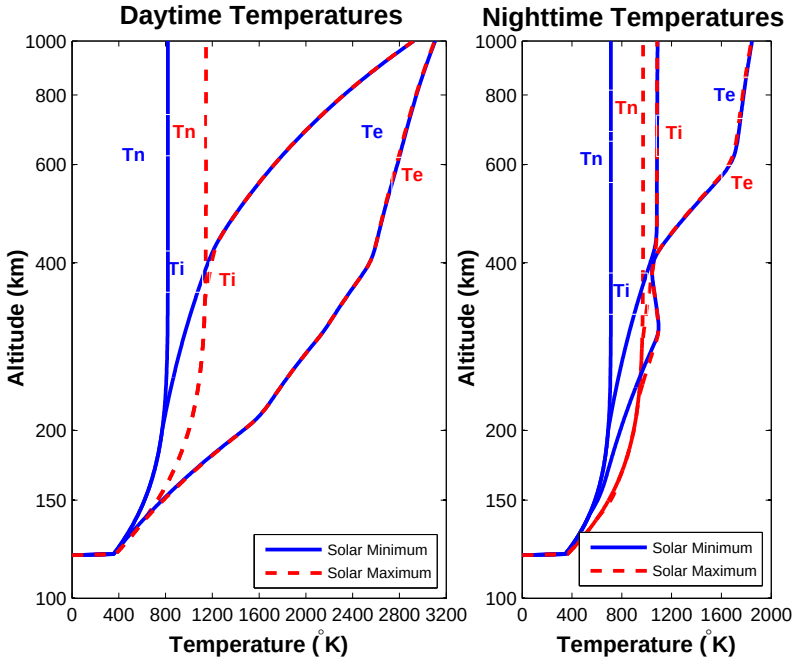

Fig. 1.2: Typical mid-latitude neutral, ion, and electron temperature profiles.

conditions. Thus, in situ instrumentation becomes important for providing high resolution spatial and temporal observations of local plasma parameters such as density and temperature. These measurements are imperative to study ionospheric phenomena (such as sporadic-E layers and spread-F) and can also be fed into the more advanced physics-based assimilative models such as Utah State University's Global Assimilation of Ionospheric Measurements (USU-GAIM) model [4] used for ionospheric specification.

Electric probes were the first in situ instruments for the measurement of ionospheric plasma density. Irving Langmuir in the early 20^{th} century [5,6] was a pioneer in using electric probes for plasma chamber diagnostics, consequently, electric probes are also generalized as Langmuir probes. Since their first use in the 1920s, the Langmuir class of electric probes has been used on many sounding rockets, satellites, and inter-planetary spacecrafts to perform in situ measurements of electron density (n_e) and temperature (T_e), ion density (n_i), and as an indicator for spacecraft charging [7,8]. Although the Langmuir probe technique itself is simple enough, the devil lies in the details of the theory and the theory's limitations in applications to real world observations. In the first section of this chapter we present an overview of the basic theory behind the operation of a Langmuir probe, followed by a list of the limitations to the basic theory that complicate the accurate analysis of I-V curves. We subsequently present various implementation techniques of a Langmuir type electric probe, and conclude the section with the challenges in its implementation. The second section presents the details of three different ionospheric research projects undertaken at Utah State University in the past decade. We conclude the chapter with an outline of the dissertation research.

1.1 Langmuir Probe Review

The Langmuir probe technique involves applying a voltage to a metallic conductor immersed in plasma and observing the collected current. The observed total current, I, is a summation of various currents such as electron and ion thermal currents, photoelectron current, secondary electron currents, etc. The benefits of the simplicity of this technique, however, are offset by the complexity of the theory required to analyze the obtained current

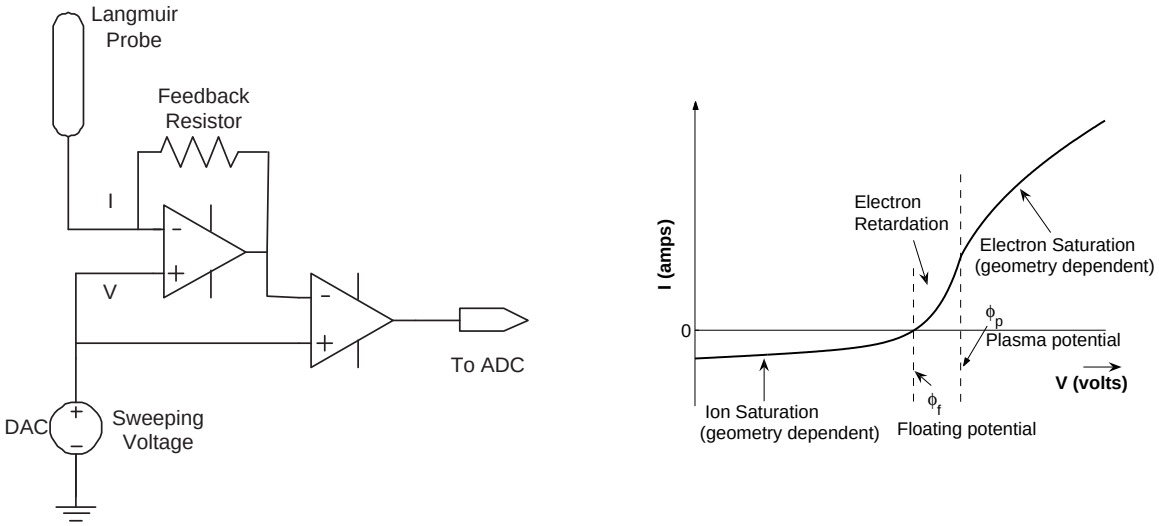

Fig. 1.3: A basic transimpedance amplifier-based Langmuir probe circuit used as a front-end to an analog-to-digital convertor, and an I-V curve that such a probe would observe in plasma.

vs. potential, or I-V, curves. Figure 1.3 depicts a typical operational amplifier based circuit diagram of a Langmuir probe and a typical I-V curve observed by such an instrument in a plasma with a Maxwellian velocity distribution. The ion current has been exaggerated by an order of magnitude to ease the viewing of the plot. Note that the current "from" the probe to the plasma (i.e. electron collection current) is considered positive. The observed I-V curve along with a complete model of all the current contributions to the probe can then be used to determine various plasma parameters such as density and temperature.

1.1.1 Basic Theory of Operation

For a Maxwellian distribution of particle velocities, the average magnitude of the velocity component in a single direction (say x) is given by

$$\overline{|\vec{v_x}|} = \sqrt{\frac{2k_BT}{\pi m}}, \tag{1.1}$$

where k_B is Boltzmann constant, and T and m are the particle species' temperature and mass, respectively. The random thermal current to a probe in a Maxwellian plasma of

charge species q_j, primarily depends on the density n_j and the surface area A of the probe, and is given by

$$I_{th_j} = \frac{1}{2} n_j q_j A \overline{|\vec{v_x}|} = n_j q_j A \sqrt{\frac{k_B T_j}{2\pi m_j}}, \tag{1.2}$$

where only half the particles in the plasma have velocities directed towards the surface of the probe to be collected [9,10]. Equation 1.2 governs the random current collected by any conducting surface that is at the same potential as the surrounding charged particles. A typical Langmuir probe is operated to collect current over a range of potentials applied on the probe's surface relative to the particles being collected. The I-V curve thus obtained can be divided into three regions of operation: electron retardation, ion saturation, and electron saturation (as illustrated figure 1.3). These regions are named after the dominant collected charged species over that range of applied potentials and are divided by the plasma potential and the floating potential. The plasma potential, ϕ_p, is the potential at which no electric fields exist between the probe surface and the surrounding quasineutral ($n_e \cong n_i$) plasma. The only current collected at this potential is the random thermal current of the charge species as given by equation 1.2. As $m_e \ll m_i$ and $T_e \approx T_i$, the one directional mean electron velocity $(2k_B T_e/\pi m_e)^{1/2}$ is at least 50 times the mean ion velocity $(2k_B T_i/\pi m_i)^{1/2}$, resulting in the electron random thermal current being larger than the ion random thermal current. At steady state the currents to a surface must balance, thus ϕ_p is not an equilibrium potential for an isolated body in a plasma. The floating potential, ϕ_f, is the equilibrium potential attained by an isolated probe, such that the total current due to electrons and ions to the conducting surface sums to zero. This potential is a few tenths of a volt negative relative to ϕ_p in the ionosphere, so as to repel the excess electron thermal current.

For a probe at any potential besides ϕ_p there exist electric fields between the probe surface and the surrounding plasma, such that the quasineutrality of the plasma around the probe is violated and the net local charge density, $\rho = e(n_i - n_e)$, is no longer zero. A qualitative depiction for a probe at negative potential $-\phi_0$, relative to ϕ_p, is shown in figure 1.4 . This non-neutral region around a biased probe is known as a "sheath" and extends

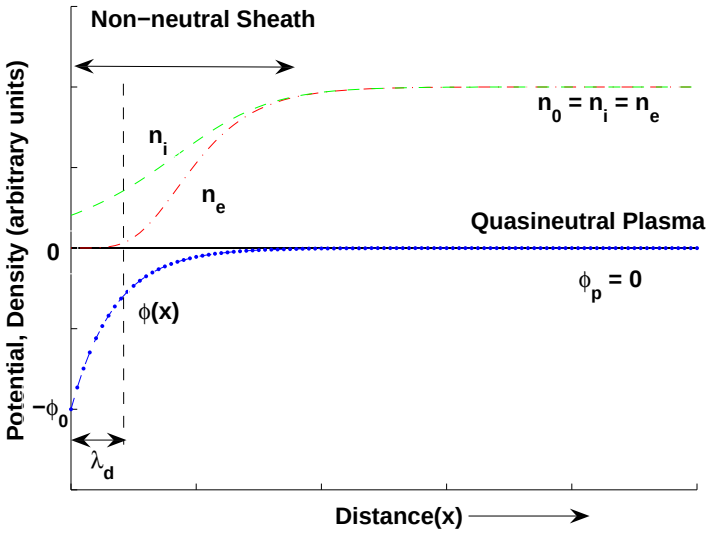

Fig. 1.4: The plasma potential (ϕ_p) is referenced as zero and the plasma density at ϕ_p is taken as $n_0 = n_e = n_i$. The sheath is few Debye lengths thick and the plasma is quasineutral outside the sheath.

over several Debye lengths, where a Debye length, λ_d, is defined by

$$\lambda_d = \sqrt{\frac{\epsilon_0 k_B T_e}{2\pi m_e}}, \tag{1.3}$$

and ϵ_0 is the free-space permittivity. Essentially, the Debye length is the length scale over which the charge on a biased probe is shielded in the plasma. Although the Debye length is independent of the bias on the probe surface, the non-neutral sheath around the probe surface increases in size as the bias on a probe is increased.

As is seen in figure 1.4, for a negatively biased probe relative to ϕ_p, there is a net positive charge density (ρ) within the sheath. The electric field within the sheath points from the plasma to the probe as the potential profile $\phi(x)$ rises from $-\phi_0$ on the probe surface to 0 several Debye lengths away. This potential structure acts like a "hill" for the electrons and a "valley" for the ions; i.e. the electrons need additional kinetic energy to overcome the potential hill or else they get reflected back, whereas the ions get accelerated to the probe surface as they descend into the valley.

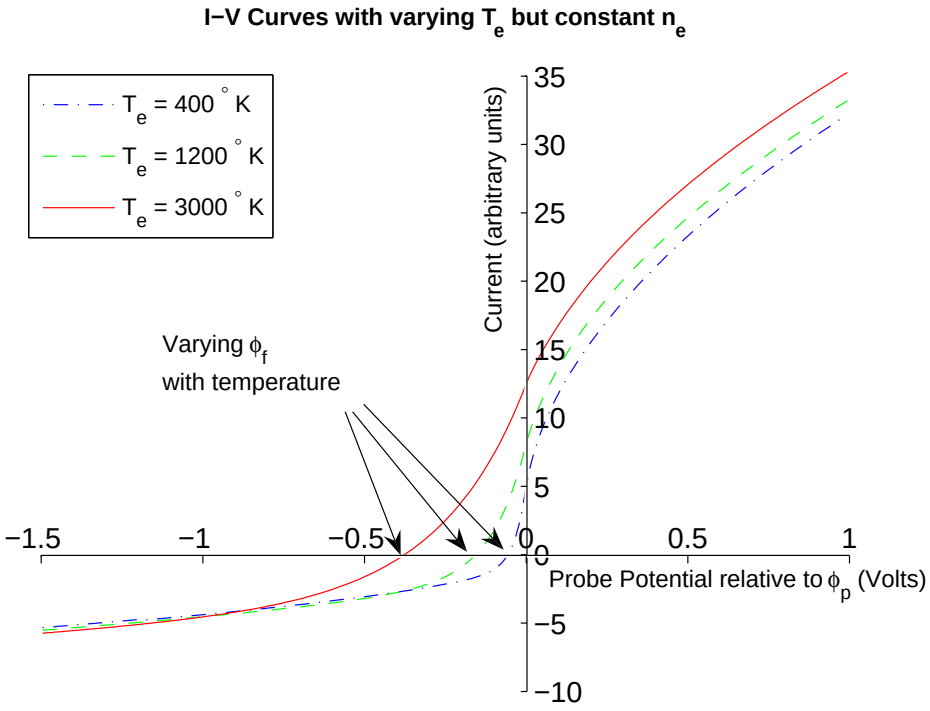

Fig. 1.5: I-V curves for a cylindrical Langmuir probe for various plasma temperatures and constant density.

This region is called the electron retardation region and the curve is dependent on the average energy, or temperature, of the the electrons. For a Maxwellian population of electrons, the electron current in the retardation region decreases exponentially and is given by

$$I_e(\phi) = I_{th_e} \exp\left(\frac{e(\phi - \phi_p)}{k_B T_e}\right), \tag{1.4}$$

where ϕ is the potential applied to the probe, e is the fundamental electron charge and I_{th_e} is the electron thermal current given by equation 1.2. Figure 1.5 depicts the variation in the retardation region of the I-V curve as the temperature varies with a constant plasma density [11]. Once again the ion current has been exaggerated from its true value by an order of magnitude. It is important to note that the floating potential varies with temperature.

A logarithmic plot of the electron retardation current has a slope that is proportional

to the electron temperature, as is evident from equation 1.4. Thus, if we subtract the ion current contribution from the total observed current, then the resultant electron retardation current can be used to determine the electron temperature. The highest measurable temperature is governed by the range of the sweep voltage, and the lowest measurable temperature is governed by the sweep step size such that sufficient observations are made to resolve an exponential curve. Although the ions are being attracted when the applied potential is less than ϕ_p, the ion current magnitude is negligibly smaller than the electron retardation current until the applied negative potential approaches ϕ_f. At this point the diminishing electron current becomes smaller than the ion current and the total current flips polarity (refer to figure 1.3).

When the potential is greater than ϕ_p or much less than ϕ_f, the I-V curve enters the saturation current regions. These two saturation current regions are where current due to either one of the plasma species is predominant. The currents collected in the saturation regions are strongly influenced by the geometry of the probe, the sheath size, and the velocity of the probe relative to the surrounding plasma.

In the case of a plane probe at a potential $\phi_0 > \phi_p$, the electron density near the planar probe surface will be greater than the ambient plasma density n_0 due to attractive potentials. However, the maximum collected current will be determined by the random crossing of electrons from quasineutral plasma into the sheath. Thus, the plate saturation current will have a maximum value as given by random thermal current (equation 1.2).

For the curved probes (cylindrical and spherical), sheath size determines the magnitude of the collected saturation current. If the sheath size is much smaller than the probe radius, then irrespective of the geometry all the current crossing the sheath boundary is collected. In other words, all probes behave like a planar probe and no more current than the plasma thermal current crossing the sheath boundary is collected. This condition is referred to as thin sheath in the literature [9, 12]. When the sheath size is comparable or larger than the probe radius (i.e. thick sheath) not all particles entering the sheath are collected. Rather the collection of individual particles is dependent on their impact parameter p which determines

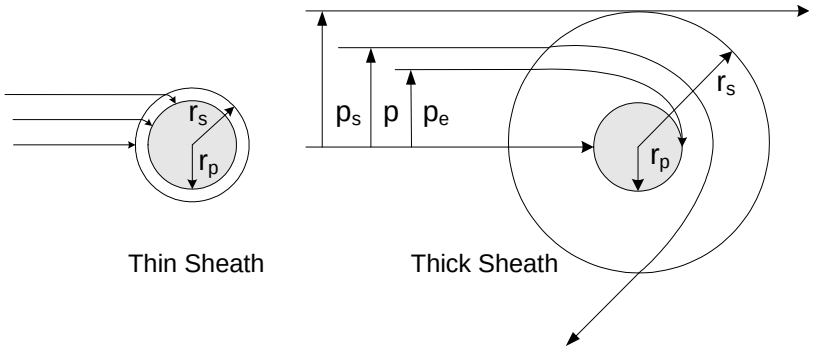

Fig. 1.6: Particle orbits for current collection in two different scenarios, thin sheath and thick sheath. "p" is the impact parameter. In the case of thick sheath, the probe effective radius increases ($p_e > r_p$) with increase in applied voltage due to particle orbit motion.

the orbital motion of the particles around the curved probe surface. For this reason the thick sheath current theory is also known as Orbital Motion Limited (OML) theory [9, 12]. The thin and thick sheath situations are pictorially depicted in figure 1.6. The OML collection current is determined by integrating over all impact parameters that result in particle orbits intersecting the surface of the probe. As the sheath size increases with the applied potential, the cross-sectional area of impact parameters intersecting the probes surface also increases, thus giving a new larger effective collecting area for the probe in the saturation region. An approximated general expression for the current in the saturation region [9] is given by

$$I_j(\phi) = I_{th_j}\left(1 + \frac{q_j(\phi - \phi_p)}{k_B T_j}\right)^{\beta}, \tag{1.5}$$

where

$\beta = 0$ Flat plate probe,

$\beta = 1/2$ Cylindrical probe,

$\beta = 1$ Spherical probe.

The parentheses expression in equation 1.5 signifies increase in collection current with the growth in effective collection area as the potential structure around curved probes changes when $|\phi - \phi_p| > 0$. It is important to differentiate this effective collection area from the term A in equation 1.2 which represents the physical surface area of the probe in

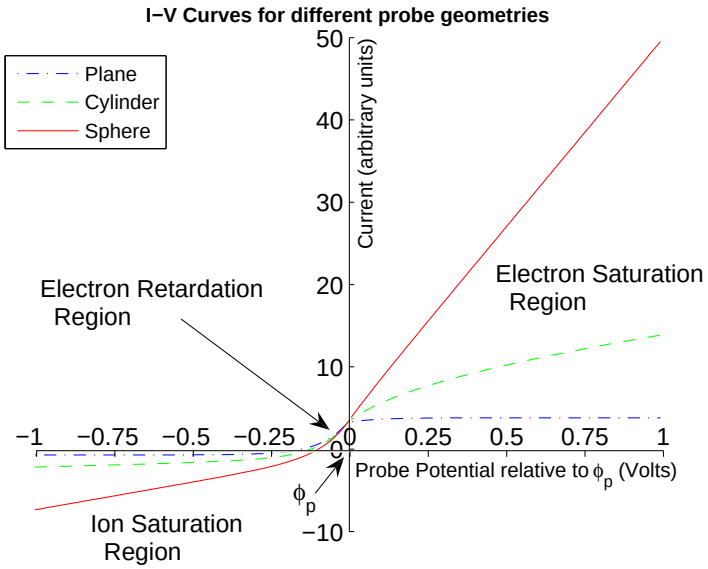

Fig. 1.7: I-V curves for planar, cylindrical, and spherical probe geometries at constant temperature and density. The floating potential is geometry dependent under thick sheath conditions.

contact with the plasma.

A plot of current for different geometries is shown in figure 1.7, with the ion current once again exaggerated by an order of magnitude to accentuate that saturation region. As is evident the saturation current for cylindrical and spherical geometries increases with an increase in applied voltage. Assuming quasi-neutrality, either one of the saturation regions (ion or electron) in principle can be used to determine plasma density. Figure 1.8 depicts the variation in the saturation region of the I-V curve as the density varies with a constant temperature.

1.1.2 Complications to the Basic Theory

Although the Langmuir probe current equations presented in section 1.1.1 contribute significantly towards understanding probe behavior, they are only valid for non-drifting, unmagnetized, and collisionless plasma that is being probed with an ideal sensor. The accuracy of the plasma parameters derived from a Langmuir probe is thus suspect unless all the non-ideal factors are suitably accounted for. This section presents an overview of the

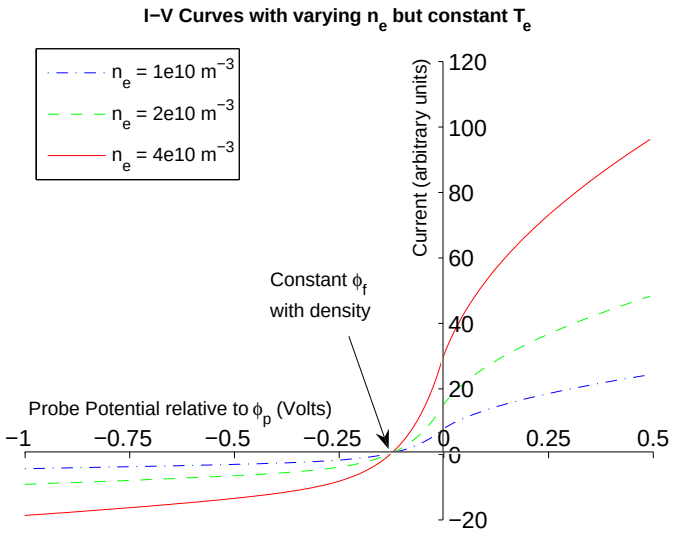

Fig. 1.8: Changes in the cylindrical Langmuir probe I-V curve with change in plasma density.

complications involved with understanding Langmuir probe measurements. For detailed theory see references [7, 9, 12–14].

Additional Current Sources

There are several other potential current sources to a probe in addition to the particle thermal currents discussed in the section 1.1.1 that effect the I-V curve. The contributions of these additional currents must be identified and subtracted out before the various equations presented in section 1.1.1 can be used to derive plasma parameters.

The first current is the photoelectron current, which is a result of exposure of the probe surface to the solar UV radiation. The emission of photoelectrons from a surface is a function of the surface material, the solar UV spectrum, cross-sectional area, and the surface potential relative to the thermal plasma. The energy of the electron leaving the surface is the difference between the surface work function and the energy of the incoming photon. As the strongest UV component of the solar spectrum is Lyman-α, the population of photoelectrons leaving the probe surface is somewhat monoenergetic. This represents a constant current "to" the probe. For a surface more negative than ϕ_p, all emitted photoelectrons will escape,

while for positive potentials some of them might be collected back. Thus, this current affects the I-V curve in the ion saturation and the electron retardation region as a constant offset. It also affects the electron saturation region until the applied probe potentials are large enough to attract all the photoelectrons back to the surface. In the high density environment of low earth orbit this current is small enough to be ignored, but at higher altitudes, such as geosynchronous orbit, where the plasma densities are lower it dominates the ion saturation region and has to be taken into account in order to determine accurate ion density. Furthermore, as this current is emitted only on the sunlit side of the probe/spacecraft, the resultant anisotropic effect makes the I-V curve analysis and the spacecraft charging problem difficult.

When an energetic charge species such as an electron strikes a probe surface three things can happen. It can get collected by the surface, it may collide with the atoms in the material and eventually reverse direction and backscatter out, or it may loose its energy exciting other electrons that then escape the material leading to secondary emission of charged particles [15]. The backscatter process primarily leads to reduction in the collected current by a fixed constant. Secondary electron emission due to incident ions leads to a current enhancement in the ion saturation region, i.e. enhancement in current "to" the spacecraft. Secondary electron emission due to incident electrons is complex in nature being a function of incident energy and the specific material impacted. The ratio of electrons emitted to incident on the surface can be greater than one with an emission distribution that peaks near 0.2 to 1KeV (refer figure 5.2 of [15]) which is an average charging level for satellites in geosynchronous orbits. Both the back scatter current as well as the secondary emission current significantly effect the observed I-V curves in high altitude orbits where the plasma densities (hence the thermal currents) are low. Thus, a knowledge of the surface properties of the probe is of utmost importance to create a complete model of current collection process.

Another source of current to a surface is through triboelectric charge transfer. If two metals with different work functions come merely in contact with each other and then

separate, the metal surface with lower work function loses an electron to the surface with higher work function [16]. This type of charge transfer is referred to as "contact charging" as it is entirely contact initiated and is not affected by the velocity of separation or by frictional sliding of metal surfaces during separation [17]. On the other hand, two objects built of insulating material will charge each other when they are rubbed asymmetrically, where the sign of charge is not only dependent on the difference in work function but also correlated with the nature of rubbing experienced by the piece of material in question [16]. This type of charge transfer is referred to as "frictional charging." These two types of charging processes are collectively referred to as triboelectric charging. Of the two, contact charging is the more important mechanism for Langmuir probes in dusty environments. Frictional charging becomes significant only when the rubbing is sufficiently vigorous and at least one of the objects being rubbed is insulating in nature. Although triboelectrification of surfaces is known to commonly occur under various conditions in the neutral planetary atmosphere (for example terrestrial dust storms [18, 19]), it has not been reported to date as one of the mechanisms for spacecraft charging and is the subject of Chapter 2 of this dissertation.

Mesothermal Plasma

In the case of spacecraft motion through plasma (i.e. plasma drift relative to probe) the thermal speed of ions is usually less than the spacecraft speed while the electron thermal speed is higher than the spacecraft speed. This situation is generally referred to as "mesothermal" plasma and primarily affects the ion saturation region as the ions are largely collected in the ram direction of the spacecraft in a sweeping motion. An approximate equation [7, 20] for the ion saturation current is given by

$$I_i(\phi) = I_{th_i}\left(\frac{m_i v^2}{2k_B T_i} + \frac{1}{2} + \frac{q_i(\phi - \phi_p)}{k_B T_i}\right)^{\frac{1}{2}}, \tag{1.6}$$

where v is the spacecraft velocity, and ϕ is the applied probe potential.

The first term is the ion "ram" current and is the dominant term at orbital velocities and

should be taken into account in order to accurately determine electron retardation current. The other two terms refer to thermal motion and increase in collection due to attractive potentials, respectively. At orbital velocities the mesothermal condition creates a rarefied wake region behind the probe. The collected ion current will change as the projected area of the probe in the ram direction changes. It also changes when the probe passes through the spacecraft's wake. This has direct influence on appropriate probe placement within the spacecraft orbital orientation. For example, a radial probe on a spinning satellite will see a "spin modulation" as it goes in and out of satellite wake, where as an axial probe will not.

Although one would expect that the electrons (having a much higher speed than the spacecraft) can still approach the probe from all directions, this is generally not so. The electrons can only penetrate into the ion wake region as much as ambipolar diffusion would allow, thus the mesothermal condition affects even electron collection current. Katz et al. [21] have reported that for a mesothermal plasma a spherical probe collecting in the electron saturation region fits equation 1.5 with $\beta = 0.5$, which is unlike the value of β that OML theory predicts. Similarly, Piel et al. [22] also report that their spherical probe observations aboard a sounding rocket fit equation 1.5 the best with $\beta = 0.58$. Thus, in essence, mesothermal effects on electron collection current seem unpredictable and are not currently understood.

Magnetized Plasma

With the addition of a magnetic field, the charged particles are constrained to gyrate about the magnetic lines of force, thereby giving them different velocities parallel and across the field lines. This gyromotion along the field lines and the existence of a sheath around the probe where electric fields exist between the plasma and the probe surface leads to a situation that is best described as a "magnetic bottle" (see figure 6 of Rubinstein and Laframboise [23]). This affects the collected current as the orientation of the probe changes w.r.t. the local magnetic field.

Parker and Murphy [24] first tackled the problem of current collection in magnetized plasma by neglecting particle thermal motion in addition to the assumption of non-drifting

collisionless plasma. This effectively gives a canonical upper bound to the collected saturation current and is given by

$$I_j(\phi) = \frac{I_{th_j}}{2}\left(1 + \left(\frac{8\left|q_j(\phi - \phi_p)\right|}{m_j\omega_j^2 r^2}\right)^{\frac{1}{2}}\right), \tag{1.7}$$

where ω_j is the particle gyrofrequency and r is the probe radius. The calculation of the upper bound that includes the particle thermal motion is further complicated and was done by Rubinstein and Laframboise [23]. A simplified version in the limit of large attractive potentials is given by

$$I_j(\phi) = I_{th_j}\left(\frac{1}{2} + \frac{1}{2}\left(\frac{8\left|q_j(\phi - \phi_p)\right|}{m_j\omega_j^2 r^2}\right)^{\frac{1}{2}} + \frac{k_B T_j}{m_j\omega_j^2 r^2}\right). \tag{1.8}$$

The first two terms are the same as Parker and Murphy equation. The last term is a result of orbital motion of the particles and vanishes for strong magnetic fields.

The problem is further complicated in the case of mesothermal magnetized plasma. Thompson's work on electrodynamics of conducting tethers in LEO [25] has treated this problem with a collisionless assumption, and shows that drifting effects cannot be ignored for electrons even if their thermal motion is much faster than the drift speed. There is presently no theory capable of making quantitative calculations of collected current in mesothermal magnetized plasma [26], short of a computer Particle-In-Cell (PIC) simulation. However, as will be shown in this dissertation work, various assumptions can be made based on the expected plasma conditions that make the data analysis problem tractable.

Collisional Plasma

In the presence of collisions probe theory becomes extremely complicated. Presented here are two limiting cases and how they affect the current collection equations described earlier. First, if the mean free path of the particles, h, is less than the sheath extent, then the equation of motion for particles within the sheath is different from the free-fall collisionless

equations used to derive OML current collection equations. Due to these collisions the potential profile within sheath is affected. The collected current increases as the orbital motion of the particles are disrupted. In the limit of small h compared with sheath size but significantly larger than the probe radius, the increase in collected thermal current can be approximated by a factor of h/r, where r is the radius of the probe [9].

Second, if the mean free path is not significantly larger than the probe radius, then due to particles blocked by the probe, the distribution of particle velocity at a distance of h from probe surface will defer from the collisional region farther away from the probe. This depletion of plasma close to the probe surface can only be exhaustively numerically calculated, possibly via a PIC simulation.

An asymptotic analysis of the effect of collisions in a non-drifting magnetized plasma has been done by Sanmartin [27]. However, due to the complexity involved, collisions in a magnetized plasma are generally ignored. Early computer simulation programs (NASCAP /LEO and POLAR) have shown the collisionless approximation to be good to within 5% [28] under low Earth orbit ionospheric conditions.

1.1.3 Instrument Implementations

An electric probe can be implemented in different ways, each having a certain advantage in deriving a particular plasma property. Three different types are reviewed here and shown conceptually in figure 1.9.

Sweeping Langmuir Probe

A Sweeping Langmuir Probe (SLP) applies a range of voltages, measuring the collected current at every step, thus generating an I-V curve. From this curve all of the plasma properties can be reduced. The disadvantage is that a sweep, consisting of many observations along the I-V curve, produces only one measurement of n_e, T_e, n_i, ϕ_f, and ϕ_p. In other words the temporal resolution (hence spatial resolution, in case of a high velocity spacecraft) is low. Furthermore, the probe relies on the assumption that the plasma parameters are not changing around the probe as the I-V sweep is made. This may not necessarily be

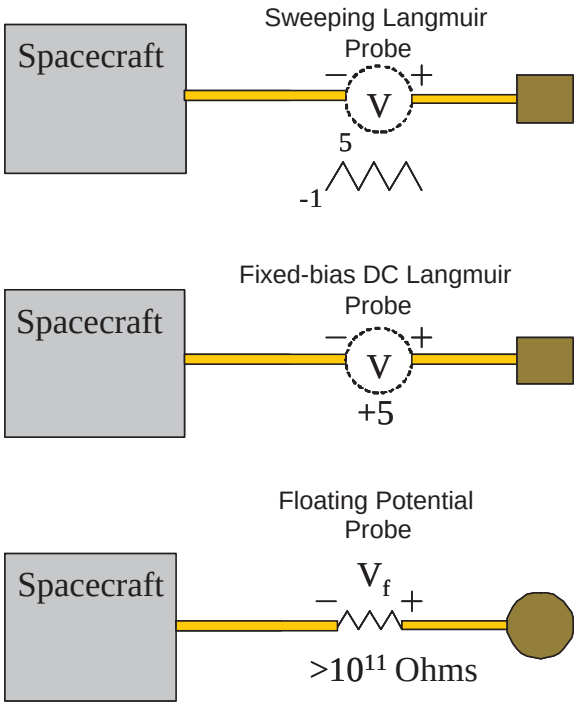

Fig. 1.9: Three different implementations of Langmuir class of electric probes.

true for a slow sweep on an orbital spacecraft. The SLP is usually deployed on a boom such that it is at least a few Debye lengths away from the spacecraft surface. The geometry of the sensors deployed for this type of probe are usually cylindrical or spherical in shape, although some flat probes have been used on 3-axis controlled spacecrafts.

Fixed-bias DC Langmuir Probe

A fixed-bias DC Langmuir Probe (DCP) measures the collected current only in the saturation regions by applying a single voltage relative to spacecraft chassis ground. As the saturation current is directly proportional to plasma density, the advantage of this technique is the high resolution measurement of plasma density. The disadvantage is that this technique measures only relative change in density and not the absolute density. Furthermore, this technique is also susceptible to shifts in spacecraft floating potential as explained in the next section. Finally, for this technique to be useful a separate instrument has to measure absolute electron density to which the DCP observed relative density can be normalized.

This is by far the most common probe flown due to its simplicity of construction and data analysis.

Floating Potential Probe

A Floating Potential Probe (FPP) measures the voltage difference between an isolated floating sphere and the spacecraft chassis ground. The floating sphere is isolated from the payload by a high impedance resistor (typically $> 10^{11}$ ohms). The idea here is that the floating probe sensor sits at the floating potential and hence to within a few eV of the plasma potential. The floating potential of a spacecraft can be different from that of a typical floating probe sensor due to its uneven geometry, different surface properties, exposed current collecting potentials, etc. The measured potential difference between a single FPP sphere and the spacecraft chassis ground is given by

$$\phi_{FPP} = (\phi_{sphere} - \phi_{sc}) - \left(\vec{E_0} + \vec{v_{sc}} \times \vec{B}\right) \cdot \vec{d} + \phi_{instr}, \tag{1.9}$$

where ϕ_{sphere} and ϕ_{sc} are the floating potentials of the probe and the spacecraft surface relative to plasma potential, $\vec{E_0}$ is the ambient electric field in the plasma, $\vec{v_{sc}} \times \vec{B}$ is the electric field generated by the motion of the probe through plasma, $\vec{v_{sc}}$ is the spacecraft velocity across the ambient magnetic field $\vec{B}$, $\vec{d}$ is the length of the boom, and ϕ_{instr} represents non-geophysical instrumentation contributions such as work function differences. The contributions of the electric fields within the ϕ_{FPP} measurement can be canceled by adding a similar measurement from another FPP sphere deployed 180° apart from the first sphere, and dividing the total by two. This is because the vector $\vec{d}$ reverses signs on the opposite boom. A high resolution FPP measurement is a good indicator of changes within the spacecraft floating potential, a.k.a. the spacecraft charging level.

1.1.4 Instrument Implementation Issues

Although the Langmuir probe technique itself is straightforward, and the theory complex yet arguably well understood to make meaningful measurements, building a probe for

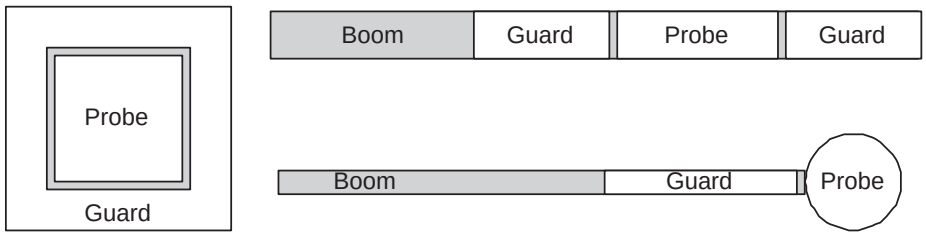

Fig. 1.10: Langmuir probe guarding schemes. The guards are kept at the same potential as the probes.

measuring the space environment that behaves in an expected way poses further challenges for the experimentalist [7, 9]. Only the most important challenges in implementation are presented here.

The theory outlined in section 1.1.1 is for infinite planar and cylindrical probes and does not take into account any end effects around the actual probe's finite edges. The current collected by an actual probe will thus deviate from the expected. This is marginally countered by placing electrically isolated guard electrodes around the actual probe that are driven at the same potential as the probe. Figure 1.10 depicts some guarding schemes. It is also important to select an appropriate size for the probe to make sure that it operates in the regime (thin sheath or thick sheath) that the experimentalist is desiring.

Work function patchiness leads to hysteresis in the I-V curve as a probe sweeps up and down. This is known to affect T_e measurements [22, 29]. Figure 1.11 depicts such a hysteresis. This patchiness in the work function of the probes surface can come via two means. First, the metal surface of the probe can have inherent work function patchiness, such as in the case of steel. This is usually countered by uniformly coating the probe with inert metals or alloys such as Gold, titanium nitride [30], rhenium, or molybdenum [7]. Another approach that has been used in the past is to make the probe uniformly "dirty" by coating it with aquadag or aerodag, which are just water or alcohol based carbon coatings, respectively. Secondly, surface contamination due to adsorption of impurities also imparts an insulating patchiness to the probe even if the potential of the underlying metallic probe is highly uniform. This can be countered in several ways. A probe can be thoroughly cleaned, sealed in an air tight container, and released once the spacecraft reaches space.

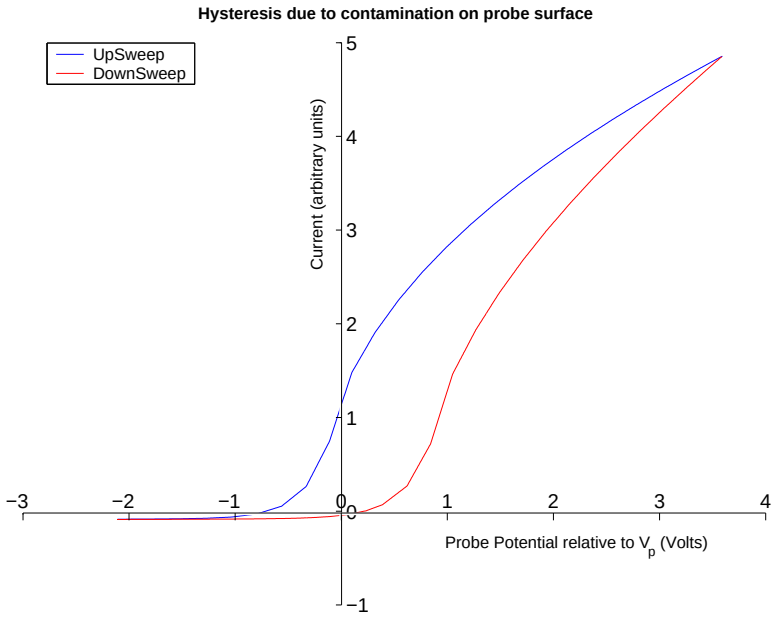

Fig. 1.11: Hysteresis in the I-V curve when the probe surface has a non-uniform work function.

Or it can employ an in-flight cleaning method, such as internal heating (to boil off the contaminants) [31] or by applying high potentials for short periods of time (thus using electron bombardment or ion sputtering to kick off impurities) [32, 33].

It is also important to realize that the plasma probe and the spacecraft ground are a closed current loop. Thus, if the probe collects additional electron current by operating in electron saturation region, the spacecraft surface closes the loop by collecting additional ions and fewer electrons. But as the ion current is more than an order of magnitude smaller than the electron current, the surface area of the spacecraft has to be much larger than that of the Langmuir probe in order to prevent the floating potential of the spacecraft from varying significantly. If the area ratio of spacecraft surface to probe surface is not on the order of 1000 or greater, then the spacecraft floating potential will change significantly during probe operation [34]. In the case of a Sweeping Langmuir Probe this will lead to oscillations in the spacecraft ground potential as the probe performs its sweep from negative to positive potential and then back to negative potential. It is thus important that when one designs a

probe a large enough ratio of spacecraft surface area to probe area be carefully considered. The area of the probe also determines the magnitude of current collected, which in turn dictates the sensitivity of the electronics required. Analyzing data in the presence of this shifting potential is difficult and is the subject of Chapter 4 of this dissertation.

In the case of a rocket trajectory, extending from the mesosphere to the F-region ionosphere, it is desirable to be able to measure densities over six orders of magnitude. Thus, the electrical design of the instrument should either have a dynamic range wide enough (with enough resolution) or should employ adaptive circuitry. Another approach taken is to measure the current in multiple channels with different current gain ranges. While this gives enough resolution in the observed I-V curves, it comes at the expense of higher downlink bandwidth. The performance of electrical printed circuit boards also varies with the board temperature. In order to account for these variations, an accurate calibration is required over the expected temperature ranges. The calibration efforts become harder for probes that have small surface areas and are expecting to measure currents in picoAmps. Such an instrument must be designed in a way to eliminate board leakage currents to critical measurement circuits.

Finally, it's important to note that all of the theoretical expressions presented above incorporate the applied probe potential relative to ϕ_p. In reality, the potential applied by the instrument to the probe is relative to the spacecraft ground which is floating at ϕ_f. This has two implications. First implication is that the Langmuir probe is sensitive to the spacecraft floating potential which changes both with probe-to-area ratio as well as temperature (refer to section 2.1 figure 1.4). Consider that a sweeping Langmuir probe is operated from -1 volts to +5 volts, where the potential to the probe is applied relative to the spacecraft chassis ground, i.e. the spacecraft floating potential. Spacecrafts are known to charge several kiloVolts negative in geosynchronous orbit. Thus, if the spacecraft floating potential was more negative than -6 volts w.r.t. ϕ_p, then the observed I-V curve will never even record the electron saturation region. While a SLP can still record the ion saturation region and hence derive absolute plasma density, a DCP designed to operate in the electron saturation region

will be adversely affected by the negative shift in spacecraft floating potential. The second implication is that it is of utmost importance to first accurately determine ϕ_p within the SLP I-V curve before any of the above presented equations can be used to reduce SLP data to absolute density and temperature. Thus, before any probe is designed for a particular mission, it is imperative to acknowledge the range of floating potential the spacecraft is expected to experience.

1.2 Programs at Utah State University

Utah State University's Space Dynamics Laboratory (USU/SDL) and its predecessors have been involved in sounding rocket investigations for over four decades [35]. Almost all of the USU rocket payloads have included a Langmuir probe and a radio frequency (RF) probe. The operating principles of a typical RF probe can be found in the work done by Balmain [36, 37]. Presented in this section is an overview of two separate sounding rocket investigations which carried different designs of similar instruments. Also presented is an overview of a USU built instrument suite that is now deployed on the International Space Station.

1.2.1 Sudden Atom Layer

The NASA Sudden Atom Layer (SAL) sounding rocket (21.117) was launched as part of the COQUI II campaign from Puerto Rico on February 15, 1998 at 20:09 LT. The rocket's main scientific purpose was the probing of sporadic sodium layers (Na_s). These are thin (1 km) layers of neutral atomic metal that form in the mesosphere, primarily within an altitude range of 90-100 km. The nighttime ground based lidar observations of these layers show them appearing almost explosively (within several minutes) and lasting for a few hours over the course of the night.

USU contributed two instruments for electron density measurement to SAL: a radio frequency Swept Impedance Probe (SIP) for absolute electron density measurement and a cylindrical fixed-bias DC Langmuir Probe (DCP) for high resolution relative electron density measurement. Besides these two instruments the payload also included a charged

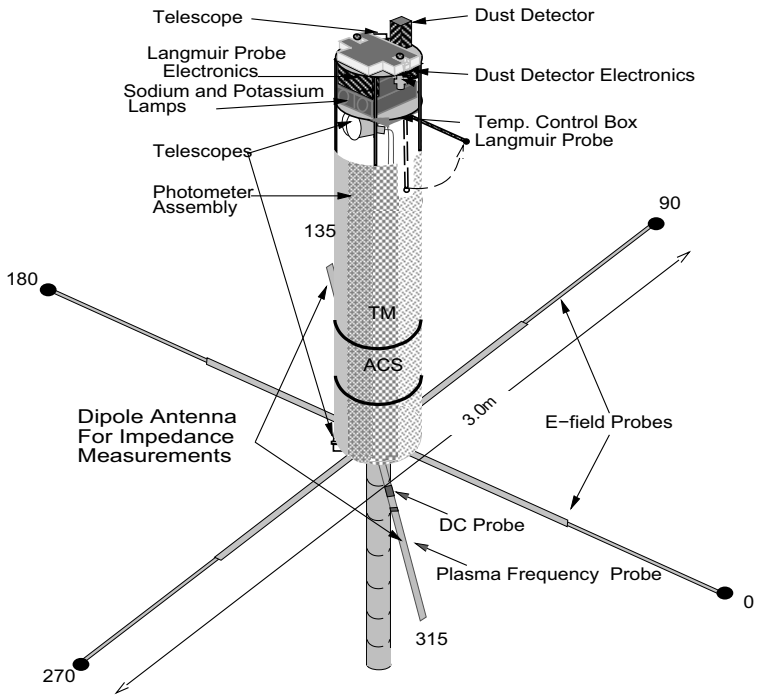

Fig. 1.12: Sudden Atom Layer (SAL) conceptual instrument layout.

dust detector, a Langmuir probe operating as Fast Temperature Probe to measure electron temperature, telescopes to measure sodium airglow, photometers and lamps to measure neutral sodium density, and four floating spheres used for E-field measurement. Figure 1.12 shows a conceptual layout of the instrumented payload. The analysis of the non-USU built instruments has been published elsewhere [38–40].

The SIP consisted of two booms deployed 180 degrees apart with a 2-meter tip-to-tip length and a 2.54 cm diameter. The instrument used the last 52.5 cm of the booms as active elements of the antenna. The antenna was differentially driven with a 1-Volt sinusoidal signal, with a frequency sweep at 40 fixed frequencies ranging over 0.2 - 12 MHz, at the rate of 96 sweeps per second. The magnitude of current flowing to the antenna was monitored using an RF current transformer. The antenna was electrically short at the driving frequencies with a free space capacitance of $C_0 = 2.6$ pF. The DCP made use of two 5 cm long cylinders near the base of both the booms of the SIP antenna. The probe was fixed bias +3 volts relative to the payload skin to operate in the electron saturation region.

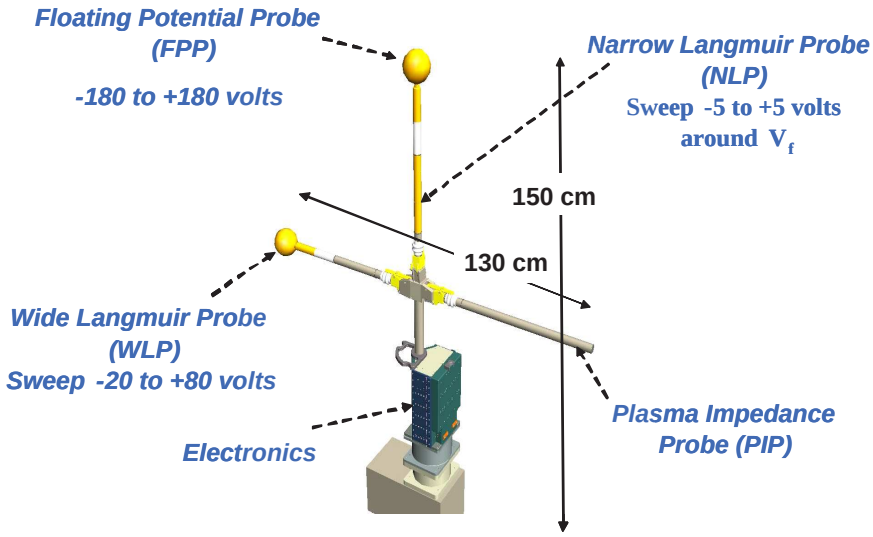

Fig. 1.13: Floating Potential Measurement Unit (FPMU) conceptual instrument layout.

1.2.2 Floating Potential Measurement Unit

USU/SDL was contracted by NASA to develop the Floating Potential Measurement Unit (FPMU) as a tool to study surface charging of the International Space Station (ISS) [41]. The FPMU was developed under intense oversite and reporting requirements as it was deemed critical for ISS safety operations.

The FPMU instrument suite is comprised of four separate instruments as illustrated in Figure 1.13: a Floating Potential Probe to measure the floating potential of the ISS, a Wide-sweeping Spherical Langmuir probe, a Narrow-sweeping Cylindrical Langmuir Probe, and a Plasma Impedance Probe operating as a Plasma Frequency Probe that tracked the plasma upper hybrid frequency and a Plasma Sweeping Probe that measured the impedance of a short dipole antenna from 100 KHz to 20 MHz. To avoid any interference between individual instruments the probe surfaces were set at least two Debye lengths apart for a worst-case rarified and cold ionospheric plasma. The tip-to-tip distance from WLP to the PIP is 130 cm and the whole instrument stands about 150 cm tall.

The Floating Potential Probe (FPP) is a gold plated sphere of radius 5.08 cm. The sphere is isolated from chassis ground by a high impedance circuit, approximately $10^{11}\Omega$. The FPP can measure the ISS floating potential within -180 to +180 V range.

The Wide-Sweeping Langmuir Probe (WLP) is also a gold plated sphere of radius 5.08 cm and is swept with a triangular wave from 20 to 80 V relative to chassis ground (i.e. ISS structure) at 1/2 Hz. This gives one I-V curve every second. An individual sweep is comprised of three parts: steps of 250 mV from 20 to 0 V, steps of 25 mV from 0 to 50 V, and steps of 250 mV from 50 to 80 V. This pattern was chosen as a balance between available telemetry space and the amount of data necessary to derive the required parameters. The current resulting from the applied voltage sweep is measured on two different 12-bit channels. The low-gain channel has a resolution of 700 nA/count and the high gain channel has a resolution of 3.5 nA/count. The high-gain channel has sufficient sensitivity to observe both photo emission and ion collection currents where as the low-gain channel is suited for observing thermal electron currents. The WLP can also be internally heated with a small halogen lamp inside the hollow sensor sphere that can be powered on and off. The temperature of the WLP surface is a function of solar beta angle to the ISS. Without internal heating the temperature of the WLP surface will range from -58°C for low beta to 118°C for high beta. When the internal heater is turned on the temperature of the probe will approach 350°C after several orbits. This should be sufficient to drive off many types of contaminates from the probe surface and provide a uniform work function.

The Narrow-Sweeping Langmuir Probe (NLP) is a gold plated cylinder with radius 1.43 cm and length 5.08 cm. The NLP is placed mid-way on the boom supporting the FPP and is guarded on each side by gold-plated cylinders with radius 1.43 cm and length 10.2 cm, which are swept in synchrony with the NLP. A sweep from 4.9 to +4.9 V, in steps of about 12 mV, is applied to the NLP during one second, followed by a sweep down from +4.9 to 4.9 V the next second. This sweep voltage is referenced to the floating potential as measured by the FPP. Thus, even a sweep range this small should cover the electron retardation region and some electron saturation region, enabling determination of n_e and T_e at 1 Hz. The resulting current is again measured on two different 12-bit channels: the low-gain channel with a resolution of 87.5 nA/count and the high gain channel with a resolution of 0.44 nA/count. The NLP is not internally heated and thus has no active cleaning mode.

The Plasma Impedance Probe (PIP) consists of an electrically short dipole antenna that is electrically isolated from the ISS and physically placed at 90° angle to the FPP boom and is 48.26 cm long with 2.86 cm diameter. The PIP is operated in two different modes. In the Plasma Sweeping Probe (PSP) mode, the instrument measures the electrical impedance (magnitude and phase) of the antenna at 256 fixed frequencies spread over a 100 KHz to 20 MHz range. Electron density, electron-neutral collision frequency, and magnetic field strength can potentially be deduced from these impedance measurements. In the Plasma Frequency Probe (PFP) mode, the antenna is used to track the frequency at which an electrical resonance associated with the upper-hybrid frequency occurs. From this resonance the absolute plasma density can be determined at 512 Hz rate with great accuracy. It should be noted that the PIP is considered an experimental instrument and has no formal NASA requirements for operation.

The performance of the FPMU instruments to measure the ISS floating potential (ϕ_f), the local plasma density (n_e), and Temperature (T_e), are summarized in Table 1.1 [41]. The FPMU instrument suite was deployed on STS-121 shuttle mission in August 2006 on the starboard (S1) truss of the ISS. It interfaces with the ISS through the Video Distribution System (VDS) similar to an External TV Camera Group on ISS. Thus, essentially the structural, electrical and communication interfaces of the FPMU with ISS replicate an external video camera. There have been several data acquisition campaigns to date: August 3-9, 2006, January 22-30, 2007, March 1-3, 2007, and May 3-4, 2007.

Table 1.1: The measured parameters, rates, and effective ranges for the FPMU instrumentation.

Sensor	Measured Parameter	Rate (Hz)	Effective Range
FPP	ϕ_f	128	-180 to +180V
WLP	n_e , T_e , ϕ_f	1	10^9 m^{-3} to 5×10^{12} m^{-3} , 500 to 3000 °K , -20 to 80 V
NLP	n_e , T_e , ϕ_f	1	10^9 m^{-3} to 5×10^{12} m^{-3} , 500 to 3000 °K , -180 to +180 V
PIP	n_e	512	1.1×10^{10} m^{-3} to 4×10^{12} m^{-3}

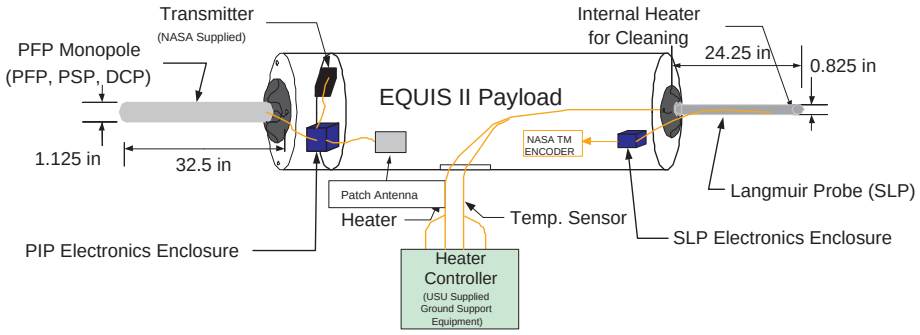

Fig. 1.14: EQUIS II conceptual instrument layout.

1.2.3 EQUIS II

The dual rocket investigation "Scattering Layer in the Bottomside Equatorial F-region Ionosphere" was part of the NASA Equatorial Ionospheric Study (EQUIS) II campaign in 2004. It was an investigation of the electrodynamics of the postsunset equatorial F-region ionosphere and the bearing this has on thin scattering layers that form here. Coherent scatter from such layers has been observed at Jicamarca Radio Observatory in Peru for many years and generally occurs as a precursor to more fully developed Equatorial Spread-F (ESF).

Two salvos of sounding rockets were launched from Roi Namur in Kwajalein on August 7^{th} and 15^{th} of 2004 at 20:52 LT and 20:21 LT, respectively. Each of the salvos consisted of one instrumented and two chemical release payloads. The instruments consisted of a cylindrical Sweeping Langmuir Probe (SLP), a cylindrical fixed bias DC Langmuir Probe (DCP), a Plasma Impedance Probe (PIP) consisting of a Plasma Frequency Probe (PFP), and a Plasma Sweeping Probe (PSP). All of these instruments were built at USU [42–44]. A conceptual layout is shown in figure 1.14. The instrument suite also included an Electric Field Probe built by Penn State University. The payload actively controlled its attitude to have its axis parallel to the local magnetic field. The rocket trajectory was almost perpendicular to the local magnetic field and the SLP and PIP probes were never in the payload wake.

The SLP was built out of aluminium with a length of 6 cm and a diameter of 2.22 cm. It was guarded on one side with a guarding probe of same dimensions, being applied the

same potential as the SLP. The combined probe and guard assembly was at the end of a 62 cm boom. The SLP internally heated for several hours before launch at 150 degrees C to remove any surface contamination and was launched hot. It was swept from -1 to +5 volts in triangular waveform pattern at 25 Hz, giving 50 I-V curves every second. The instrument used 16-bit A-to-D converters and measured the current in two different channels: High-Gain channel at a resolution of 57.9 pA/count with a range of 1.897μA and Low-Gain channel at a resolution of 5.85 nA/count with a range of 191.6μA.

The PIP too was built out of aluminium. The entire PIP boom was 92 cm long, and 2.85 cm thick. The PIP antenna was a monopole with a length of about 50 cm, making it electricaly short for frequencies below 600 MHz. The antenna was used in two different instrumentation functions of the PIP. As a PFP, the instrument was used to track the upper hybrid resonance of plasma with a phase-locked loop at a time resolution of 0.28 ms and a frequency resolution of 1 KHz. As a PSP, the instrument swept over a frequency range of 0.1 MHz to 20 MHz in 257 steps and measured the impedance. The entire sweep was completed in 70 ms.

1.3 Dissertation Overview

Although the Langmuir probe technique has been around for almost eight decades there is no single unified theory that can explain such a probe's behavior in every plasma condition. Theories have been developed for specialized limiting conditions and there still remain questions that limit the accuracy of the physical parameters deduced using these theories. The objective of this dissertation research is to carefully describe discrepancies between observation and theory while analyzing data from several flight experiments.

This dissertation is a compendium of work on three distinct projects, each culminating into a separate paper. Consequently, some Langmuir probe material as well as programmatic overview of projects presented in the current introductory chapter is repeated in each paper. Chapter 2 represents the dissertation work on SAL sounding rocket and has been published in Journal of Geophysical Research [45], while Chapter 3 represents the dissertation work done on the FPMU dataset and will soon be submitted to Reviews of Scientific Instruments.

Chapter 4 encompasses the work done on the EQUIS II sounding rockets and will also be submitted to a suitable journal. We now present a brief overview of these papers.

USU contributed a fixed-bias DC Langmuir Probe (DCP) and a Sweeping Impedance Probe (SIP) to the NASA SAL payload to observe the local plasma density along the payload trajectory. As the instrumented rocket payload flew through a region of dusty plasma it experienced an anomalous charging event. The first part of this dissertation research will make use of the datasets from the DCP and the SIP to investigate the possibility of triboelectric charging of the payload surface. Specifically, the research task for the SAL project shall include: derivation of absolute plasma density from the SIP, DSMC simulation of the payload wake effects, development of a spacecraft charging model using Langmuir probe theory, and finally the application of the model to investigate triboelectric effects on the payload and on the Langmuir probe dataset.

Chapter 3 of this dissertation encompasses the work done on the FPMU dataset. The present literature on Langmuir probes has a deficit of work that analyzes collected probe current in a magnetized and drifting plasma, a situation that is seen by the Langmuir probes of the FPMU instrument suite deployed on the ISS. Although one can use the various limiting specialized theories to reduce the Langmuir probe data to physical parameters, the results generally do not agree between different instruments. The objective of this second part of the dissertation research shall be to develop an algorithm to determine various plasma parameters from a sweeping Langmuir probe and subsequently analyze the dataset from the FPMU. The comparison of derived plasma parameters from two different geometries of Langmuir probes shall provide the validation for the algorithm. Furthermore, the derived parameters will also be compared with electron density derived from the Plasma Impedance Probe, as well as with two different ionospheric models: IRI and USU-GAIM.

Chapter 4 of this dissertation shall present the analysis of the EQUIS II dataset. As a participant in the EQUIS II sounding rocket investigation, USU provided a Sweeping Langmuir Probe (SLP), a fixed-bias DC Langmuir Probe (DCP) and a Plasma Impedance Probe (PIP). Due to the nature of the sounding rocket sub-orbital trajectory, the Langmuir

probes experienced a varying plasma drift speed that subjected them from operating in mesothermal plasma to thermal plasma and then back to mesothermal plasma. This is in contrast to the FPMU aboard the ISS which experiences a large mesothermal but constant drift speed. Furthermore, the observed Langmuir probe I-V curves on the EQUIS II sounding rockets were also marginally distorted due to excessive measurement currents collected by the SLP that charged the vehicle. A simplistic analysis of the Langmuir probe data gives plasma densities that do not agree with the results derived from the PIP. The third part of this dissertation research shall analyze the effect of payload ground potential swing on the observed I-V curves and eventually derive the the plasma parameters. The charging model developed for SAL will be used to study the effects of payload potential swing on the I-V curves and the algorithm developed for the FPMU data analysis will be used (with possible variations) to derive the plasma parameters. The accuracy of the derived parameters will be ascertained by comparison with the density as derived by the PIP. Thus, in essence, this third part of the dissertation research will be an application of techniques developed for the two previous research topics.

Finally, Chapter 5 contains a summary of the dissertation and the new insights into Langmuir probe data analysis as put forward by this dissertation. We conclude with some thoughts and recommendations for future work.

Chapter 2

Observations of Triboelectric Charging Effects on Langmuir Type Probes in Dusty Plasma[1]

Earth's mesosphere is a site of many phenomena associated with dust and aerosols such as sporadic atom layers, polar mesospheric summer echoes, and noctilucent clouds. Over the last few decades, these phenomena have been studied via modeling theory, remote observations, as well as in situ investigation using sounding rockets. One of the most important and ubiquitously used instruments for in situ investigation of electron density and temperature is the Langmuir-type probe, where a DC current is monitored from a voltage biased surface. This class of instrumentation is known to be sensitive to vehicle floating potential, ratio of payload surface area to probe surface area, and contamination of the probe surface, among other things [7; and references therein]. With all of their shortcomings, it is important that the data from this class of instrumentation be scrutinized for instrument and payload charging effects, so as to separate them from effects due to the phenomena under study.

The 80-100 km mesospheric altitude range presents a different surface charging environment than the one present at satellite orbital altitudes, which have been extensively studied [15, 46]. One difference is manifested by the enormous amount of meteoric ablation that condenses into dust particles and is suspended in the Earth's mesosphere between 80-100 km. The presence of dust at such a low altitude where the Debye length is greater than the average distance between dust particles constitutes a "dusty plasma", as compared to the "dust in plasma" at higher satellite orbital altitudes [47]. Charging of metallic surfaces by charge transfer from dust particles due to the difference in work functions or due to

[1]Barjatya, A., and C.M. Swenson (2006), Observations of triboelectric charging effects on Langmuir type probes in dusty plasma, *J. Geophys. Res., 111*, A10302, doi:10.1029/2006JA011806. Published [2006] American Geophysical Union. Reproduced by permission of American Geophysical Union.

frictional contact is known as triboelectric charging. Although this is known to commonly occur under various conditions in the neutral planetary atmosphere, it has not been reported to date as one of the mechanisms for spacecraft charging. Within this paper we present evidence for a triboelectric charging event as a sounding rocket payload passed through a mesospheric dusty plasma.

We first give an overview of the NASA Sudden Atom Layer sounding rocket payload, followed by the instrument description and data analysis of three of the onboard instruments: a radio frequency Swept Impedance Probe (SIP) for electron density measurement, a fixed bias (DC) Langmuir Probe (DCP) for relative electron density measurements, and a Floating Potential Probe (V1S) that observed the voltage difference between the payload skin and a deployed floating sphere. We present an anomaly in the DCP and the V1S dataset that points to a case of strong and sudden payload surface charging coincident with the mesospheric dust. We then develop a simple circuit model for spacecraft surface charging and Langmuir-type electric probe analysis. This model is subsequently applied to the SAL data and we conclude with a discussion of the surface charging event and its implications regarding probe behavior and the mesospheric neutral dust environment.

2.1 Sudden Atom Layer Investigation

The NASA Sudden Atom Layer (SAL) sounding rocket (21.117) was launched as a part of the COQUI II campaign from Puerto Rico on February 19, 1998 at 20:09 LT. The rocket's main scientific purpose was the probing of sporadic sodium layers (Na_s). These are thin (1 km) layers of neutral atomic metal that form in the mesosphere (as observed by lidar), roughly within an altitude range of 90-100 km [48]. Besides the three instruments whose data are the subject of this paper, the payload also included a charged dust detector, a Langmuir probe operating as Fast Temperature Probe to measure electron temperature, telescopes to measure sodium airglow, and photometers and lamps to measure neutral sodium density, the analysis of which have been published elsewhere [38–40]. Figure 2.1 depicts the payload instrument configuration.

The payload reached a maximum altitude of 115.5 km and flew through two thin Na_s

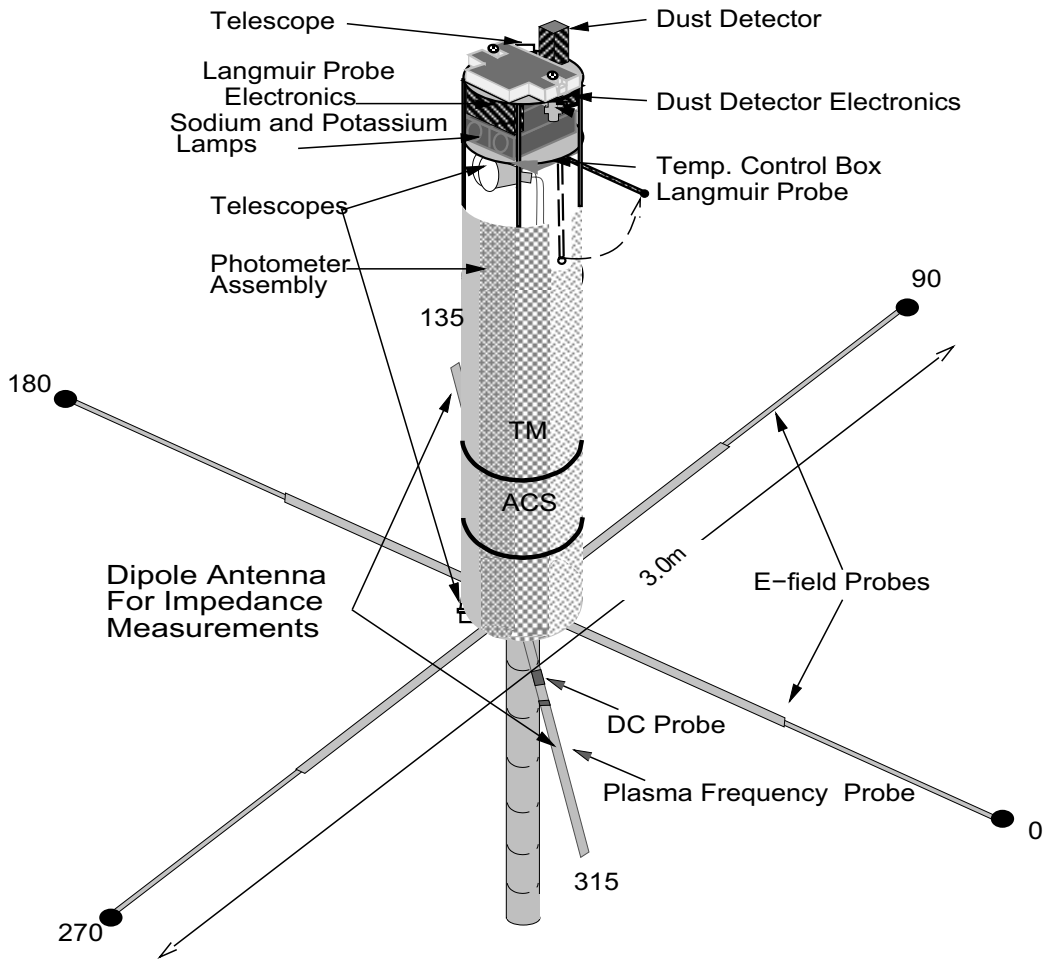

Fig. 2.1: The Sudden Atom Layer (SAL) payload.

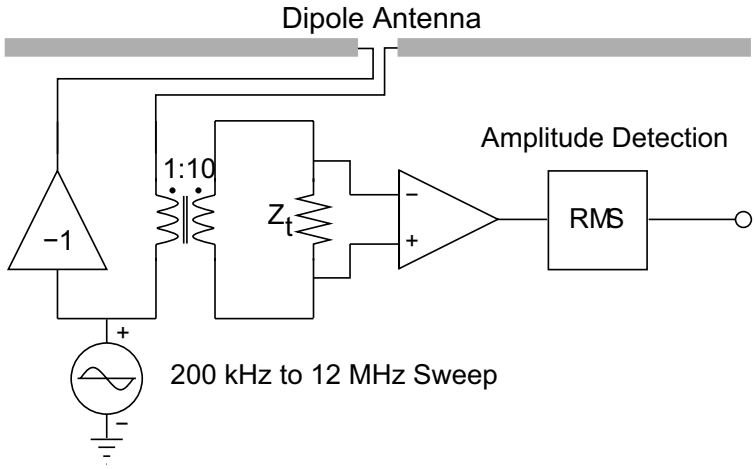

Fig. 2.2: The SIP circuit.

layers at 94 km and 97 km, with peak densities of 6000 cm^{-3} and 4000 cm^{-3}, as determined by the ground based sodium lidar. Also, a sporadic-E (E_s) layer at 92.5 km was detected by the Arecibo radar. The charged dust detector was mounted on the nose of the payload and an attitude control system was used to point the nose in the ram direction for the upleg, as well as the downleg, portion of the flight. It observed a 5 km thick, positively charged dust layer accompanying the lower Na_s layer. This dataset is presented in figures 2 and 3 within the paper by Gelinas et al. [38]. The in situ photometer data has been presented in figure 2 within the paper by Hecht et al. [39].

2.1.1 Swept Impedance Probe (SIP)

The impedance characteristics of an antenna immersed in an ionospheric plasma have been used to determine electron density for over 30 years [49–52]. The SIP consisted of two booms deployed 180 degrees apart with a 2-meter tip-to-tip length and a 2.54 cm diameter. The instrument used the last 52.5 cm of the booms as active elements of the antenna. The antenna was differentially driven with a 1-Volt sinusoidal signal, with a frequency sweep at 40 fixed frequencies ranging over 0.2 - 12 MHz, at the rate of 96 sweeps per second. The magnitude of current flowing to the antenna was monitored using an RF current transformer as illustrated in figure 2.2. Although the impedance probe was driven in a dipole configuration, the current was monitored on only one half of the antenna. The

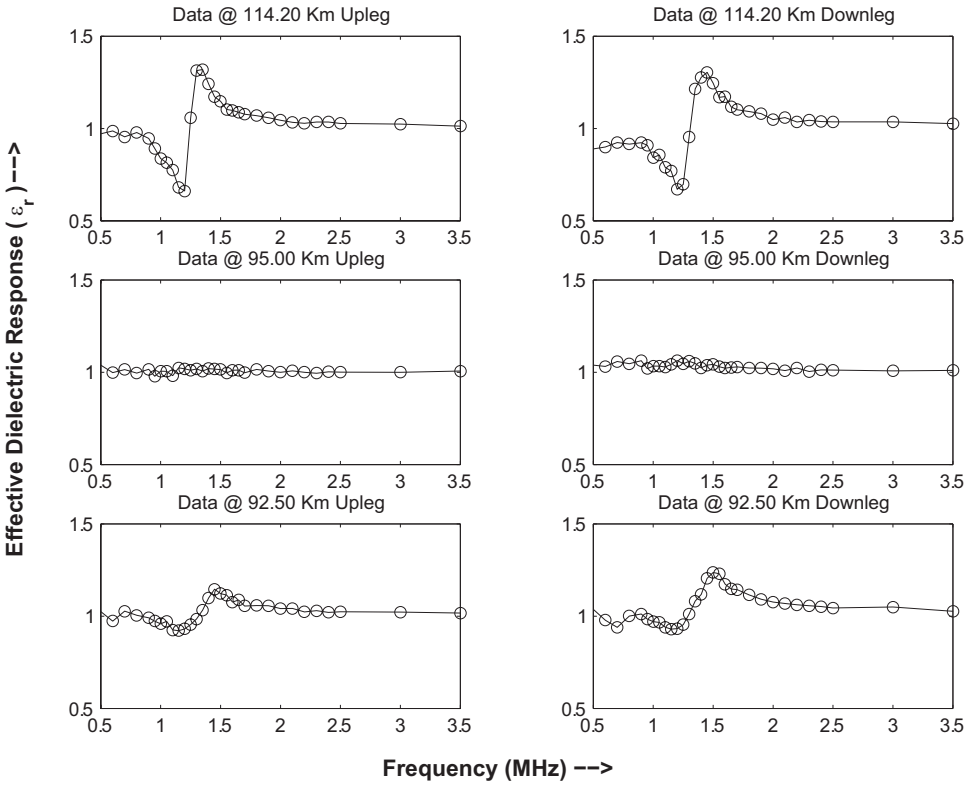

Fig. 2.3: Effective dielectric response of the SIP antenna on the upleg and the downleg. Top and bottom panels show response of instrument within the E_s layer and the middle panel shows observations in low density plasma.

antenna was electrically short at the driving frequencies with a free space capacitance of $C_0 = 2.6$pf.

The observed current magnitudes were converted to impedance magnitudes using pre-flight calibrations. We compute the effective dielectric response of the plasma surrounding the antenna, ϵ_r, as a function of frequency by

$$|\epsilon_r(f)| = \frac{Z_{plasma}(f)}{Z_0(f)}, \tag{2.1}$$

where Z_0 is the observed magnitude of the free space antenna impedance and Z_{plasma} is the measured impedance magnitudes over the swept frequency range. Figure 2.3 shows the computed effective dielectric response for three different altitudes. The figure clearly shows that SAL flew through two distinct layers of high electron density, one at about 92.5 km

and the other at 114.2 km. The center panel shows the low signal to noise ratio condition associated with low plasma density.

In order to derive electron densities from this data, we compare the computed effective dielectric response to the theoretical effective dielectric response generated from Balmain's model for a monopole antenna in a cold collisional magnetized plasma [36, 37]. Balmain's model gives us the antenna impedance as a function of five parameters: the plasma frequency ω_p, the electron cyclotron frequency ω_c, the electron-neutral collision frequency ν_{en}, the angle with respect to magnetic field θ, and the ion sheath size S. We fit our data to Balmain's theory for frequencies above that of the upper hybrid resonance where the sheath resonances and the angle to magnetic field do not play an important role and are thus neglected. We used the IGRF (International Geomagnetic Reference Field) model to determine ω_c, which was found to be within 1% of 1.06 MHz during the entire flight. We also used electron momentum transfer collision frequencies [2, 53] and neutral densities from the MSIS (Mass Spectrometer, Incoherent Scatter Radar Extended) model to find ν_{en} for the altitude profile of the rocket. The absolute electron density thus computed from the least-squares fit to SIP data for ω_p is shown in figure 2.4. The modulation in the derived electron density at the rocket spin rate is expected as the SIP antenna moved in and out of rocket wake at 1 Hz.

2.1.2 Fixed Bias Langmuir Probe (DCP)

The DCP made use of two 5 cm long cylinders near the base of both the booms of dipole antenna (refer figure 2.1). As the instrument response was combined from two cylindrical probes deployed on booms that were 180 degrees apart, the spin modulation effect is thus subdued, but not eliminated. The probe was fixed bias +3 volts relative to the payload skin to measure the electron saturation current. The DCP relative density data, normalized to the SIP data at 114 km, is shown in figure 2.4. The DCP was at its noise floor limit of 16×10^{-9} amperes in the lower altitude range of 90-94 km. This current after normalization with SIP data corresponds to an electron density of about 150 cm^{-3}.

The main theme of this paper is the investigation of the fact that the lower E_s layer

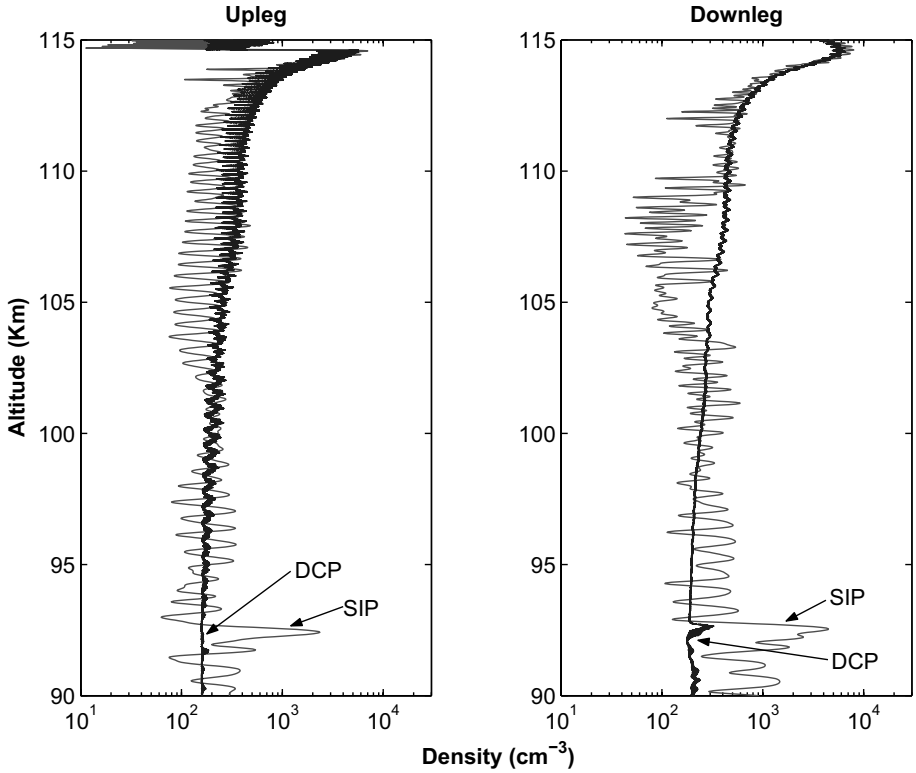

Fig. 2.4: Comparison of density profiles from DCP and SIP. DCP data is normalized to SIP density at 114 km.

observed by ground-based radar and also by the SIP is not present in the DCP data. We can be certain that this was not an instrument malfunction or failure, as the DCP did respond to the 114 km E_s layer and generally agrees well with the SIP data throughout the flight, especially if one takes into account a simulation of neutral wake effects to be discussed later.

2.1.3 V1S - Floating Potential Probe

The E-field experiment on SAL used sets of three meter tip-to-tip booms in the aft section of the payload to deploy four carbon-coated spheres of 7.62 cm diameter [54], as shown in figure 2.1. Besides the E-field data the payload skin potential was monitored as a voltage difference between one of the spheres and the payload skin; this measurement is designated as V1S. The data is shown in figure 2.5 as a function of rocket time of flight. The rocket passed through the 92.5 km E_s layer on the upleg at t=103 s and on the downleg

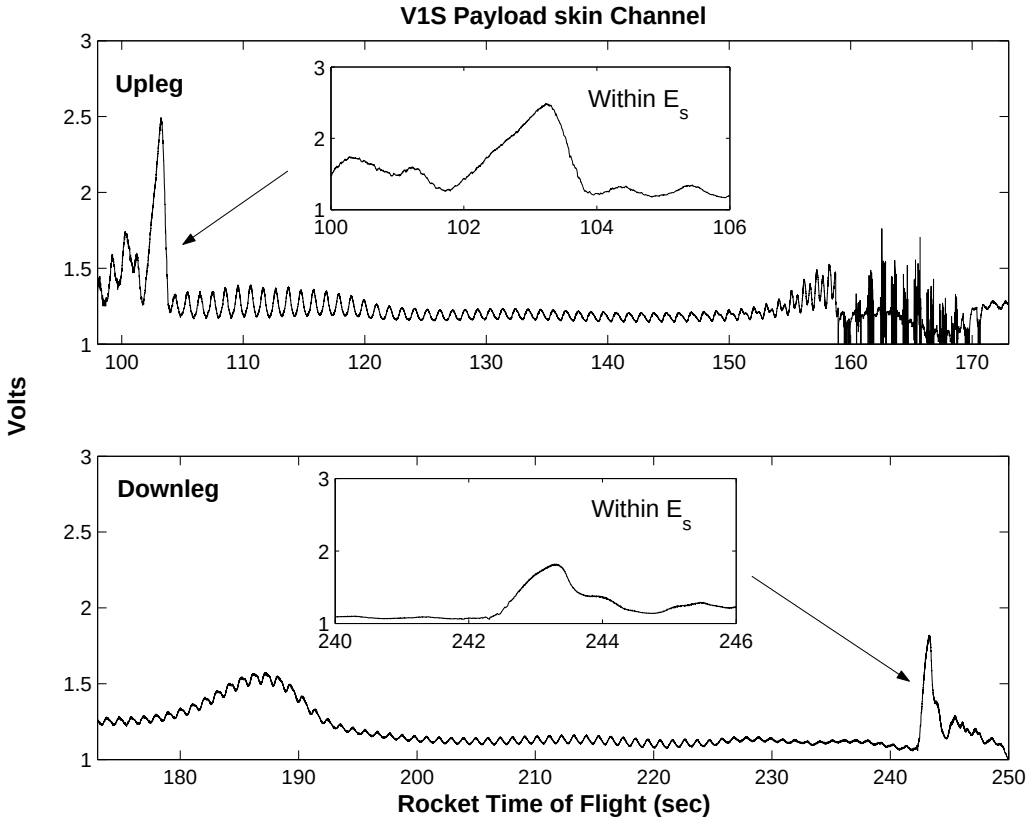

Fig. 2.5: Upleg and downleg time of flight profiles of the Floating Potential Probe (V1S).

at t=243 s. Within the layer an upwards of 2 volt difference between the payload skin and sphere was observed. The E-field within the layer was on the order of 10 mV/m [40, 54] and thus does not account for the large potential seen in the V1S skin channel. Although the V1S measurement is not a direct observation of the payload floating potential, it is nevertheless an indicator of surface charging events that occur differentially between the sensor and payload along with the minor E-field effects.

2.2 Charging Circuit Model

The typical assumption for spacecraft surface charging is that capacitive charging timescales are small compared to the timescales of interest and the process can be examined at steady state where all currents to the surface are balanced. The potential at which this balance occurs is called the floating potential when referenced to the ambient

plasma environment, which is the reference point for all potentials in this paper. We have developed a nonlinear circuit model for a current collecting surface in a plasma and implemented it in SPICE (Simulation Program with Integrated Circuit Emphasis), which is an industry standard simulation program used for simulating networks of linear and nonlinear circuit elements [55]. The numerical solvers available within SPICE are used to simultaneously calculate spacecraft floating potential and instrument response, including all the transient capacitive effects. We only consider the ion, electron, charged dust, and triboelectric currents in our model and neglect other plasma currents, since the payload was in darkness and in a low radiation environment.

The E_s layer at 92.5 km is likely to have consisted of metallic ions like Fe^+ and Mg^+ [56,57]. The Fe^+ ion thermal speed for T=180K (at 92.5 km) is about 285 m/s and the Mg^+ ion thermal speed is about 430 m/s. The rocket earth relative speed at 92.5 km altitude was determined from the rocket trajectory to be 761 m/s on upleg and 744 m/s on downleg. As the rocket velocity is within a factor of 3 of these ion thermal velocities, we chose to model the ions as a thermal current to the first order, as justified by theory [20,58].

The ion and electron thermal currents (I_i, I_e) for a cylindrical collector are given by equations (2.2) and (2.3), where the subscript represents the charged species being modeled. The current due to electrons is modeled as positive current and the current due to ions is modeled as negative current. Equation (2.2) models the electron saturation and ion retardation region, whereas equation (2.3) models the electron retardation and ion saturation regions. For a spherical collector we remove the square-root from over the last term in the saturation current equation for both species.

$$\begin{aligned} I_e(V) &= Ane\sqrt{\tfrac{k_bT_e}{2\pi me}}\sqrt{\left(1+\tfrac{eV}{k_bT_e}\right)} \\ I_i(V) &= -Ane\sqrt{\tfrac{k_bT_e}{2\pi m_i}}\exp\left(\tfrac{-eV}{k_bT_e}\right) \end{aligned} \qquad V>0, \tag{2.2}$$

$$\begin{aligned} I_e(V) &= Ane\sqrt{\tfrac{k_bT_e}{2\pi m_e}}\exp\left(\tfrac{eV}{k_bT_e}\right) \\ I_i(V) &= -Ane\sqrt{\tfrac{k_bT_e}{2\pi m_i}}\sqrt{\left(1-\tfrac{eV}{k_bT_e}\right)} \end{aligned} \qquad V\leq 0, \tag{2.3}$$

where

A	Surface area	T_e	Electron temperature
n	Plasma density	V	Surface potential
e	elementary charge	k_b	Boltzmann Constant
m_e	electron mass	m_i	ion mass.

The above equations are for unmagnetized collisionless plasma. The presence of Earth's magnetic field and the collisional behavior of the plasma in mesosphere are ignored in order to keep the model simple and tractable [9], and their exclusion should not be a major limiting factor affecting the accuracy of the model.

The dust, being at least an order of magnitude heavier than ions, is relatively immobile and is modeled as a ram current (I_{dust}). The dust particle speed distribution is very narrow around the ram speed, and therefore, the current drops as a unit step function, H, whenever the surface potential exceeds the directed ram energy. This relation is expressed by equation (2.4). As the dust observed in situ by SAL is positively charged, the current due to dust is modeled as negative current.

$$I_{dust}(V) = -A_{ram} e n_d V_{ram} H[\varepsilon - eV], \tag{2.4}$$

where

A_{ram}	ram surface area	e	fundamental charge
n_d	dust charge density	V_{ram}	ram velocity
ε	$\frac{1}{2} m_{dust} V_{ram}^2$.		

We also model a fourth current source due to triboelectric charging (I_{TE}) from the neutral dust present in the Earth's mesosphere. Triboelectric charging refers to charge buildup or deficit that occurs when two different materials come under either simple or frictional contact. If two metals come merely in contact with each other and then separate, the metal surface with lower work function loses an electron to the surface with higher work function [16]. The type of charge transfer is entirely contact initiated and is not

affected by the velocity of separation or by frictional sliding during separation [17]. The payload skin was aluminium (ϕ_{wk} = 4.2 eV), and although the composition of dust was unobserved in situ, we assume the metallic composition of the dust to be similar to that in meteorites [59, 60]. Thus the dust was most probably composed of potassium (ϕ_{wk} = 2.29 eV), sodium (ϕ_{wk} = 2.36 eV), calcium (ϕ_{wk} = 2.87 eV), magnesium (ϕ_{wk} = 3.66 eV), and iron (ϕ_{wk} = 4.67 eV). All oxidized metals behave, as far as contact charging is concerned, like a different metal with a work function equal to the depth of the acceptor levels in the adsorbed oxygen, which is about 5.5 eV and is largely independent of the nature of the metal [61, 62]. The presence of atomic sodium, as observed by lidar, leads us to believe that there was a population of dust particles with unoxidized sodium or other low work function metal adsorbed on their surface. Thus the triboelectric charging current source in the circuit model will be sourcing positive current, as each unoxidized dust particle with work function lower than 5.5 eV will leave one electron on the oxidized aluminium payload skin. The triboelectric current is modeled as

$$I_{TE}(V) = A_{ram} e N V_{ram}, \tag{2.5}$$

where N is the component of neutral dust depositing the net triboelectric current.

Each of the above current sources has been coded as a voltage-controlled-current-source (VCCS) and make up a single sub-circuit model, as shown in figure 2.6. We model the contamination present on a current collecting surface as a parallel combination of a capacitor C_d and resistor R_d [22]. The sheath is modeled as another capacitance C_s in parallel with the current sources. The current equations, including capacitive effects, are solved by SPICE simultaneously to find the floating potential of the spacecraft. The payload is modeled as a cylinder with its nose cone and aft skirt ejected and a total length of four meters and a diameter of 43 cm. The rocket was pointing to within 2° of the ram direction on the upleg and within 8° on the downleg. We meticulously calculate separate payload ram projected areas for the upleg and downleg case. Figure 2.7 shows the electrical circuit model of SAL in SPICE. Each current source shown is a complete sub-circuit of figure 2.6, incorporating

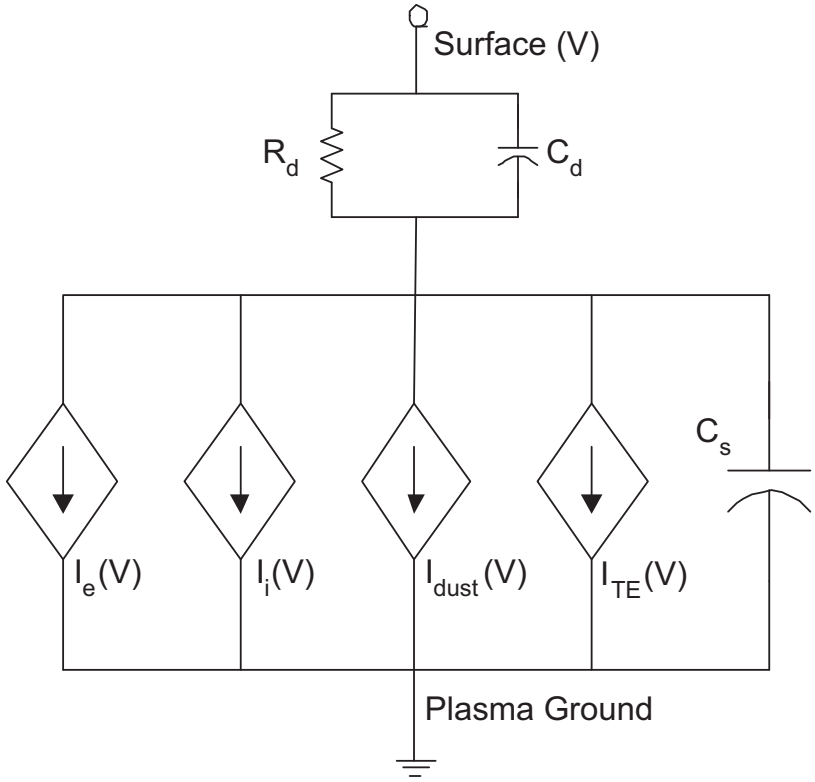

Fig. 2.6: The SPICE Voltage-Controlled-Current-Source circuit model for payload and probe surfaces.

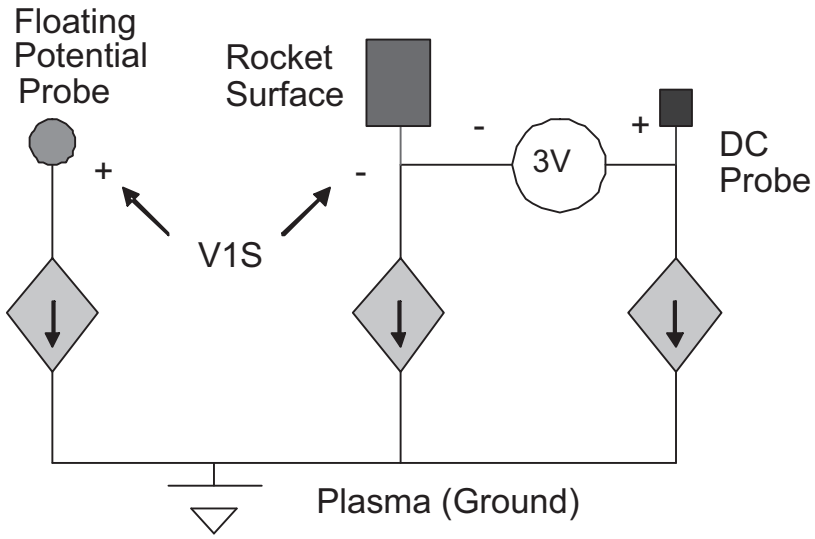

Fig. 2.7: The circuit model of the SAL payload, DC Langmuir Probe, and Floating Potential Probe.

four different current sources. The difference between the sub-circuit model used for DCP and that used for the payload collecting surface is manifested by different collecting areas, which are passed to the sub-circuit in a function call. We also model a spherical probe coated with Carbon ($\phi_{wk} = 5$ eV) for estimating the V1S channel.

As a check for the model we calculate the V1S observed potential outside the E_s layer using density as observed by the SIP. We represent the DCP and the payload skin with cylindrical surface current equations, and the V1S with spherical surface equations. Using correct DCP to payload skin area ratio, V1S simulated magnitude is 1.37 volts, which agrees quite well with the V1S channel outside the lower E_s layer (see figure 2.5).

2.3 Discussion

The wake in the neutral atmosphere around a sounding rocket at mesospheric altitudes is well known and its perturbing effects on in situ observations must be considered. The neutral wake perturbs the plasma environment through strong collisional coupling such that data from radially mounted probes spinning through this wake show "spin modulation". The radial variation in the particle density thus affects magnitude of the electron density and other measurements. We computed this wake effect for neutral particle density through a 2-D Direct Simulation Monte Carlo (DSMC) numerical calculation [63]. The simulation was done for rocket flight conditions at 92.5 km altitude, where the total neutral number density and temperature are approximated from the MSIS model to be 5.93×10^{19} particles/m^3 and 180K, respectively. We simulated three neutral species, namely O_2, N_2, and Ar. We use the same payload dimensions as in the charging model and do two separate simulations for the different angles to the ram direction on upleg and downleg. The results are shown in figure 2.8. Although the booms were not included in the simulation, they have been superimposed within the figure to show the position of SIP and DCP within the wake structure.

Figure 2.8 shows that on the upleg the density around DCP will see a minimum reduction by a factor of 2 and the SIP should see a minimum reduction by a factor of 1.25 relative to the ambient plasma density. On the downleg, although the SIP monopole should see an enhanced density as it swings into and out of the ram side of the rocket, the DCP is

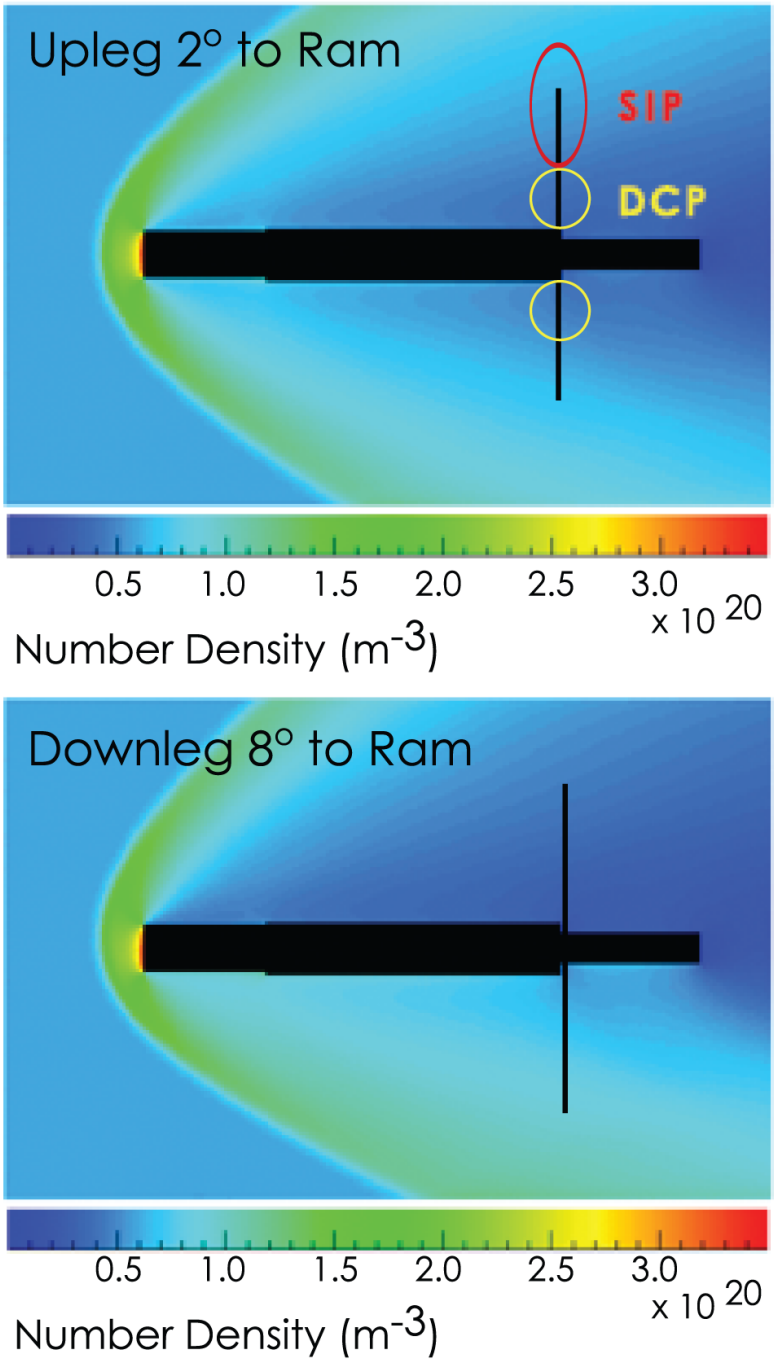

Fig. 2.8: DSMC simulations of SAL payload wake on upleg and downleg.

averaging the signal from both the booms and should see less of a density swing. All of this corresponds well with data outside the 92.5 km E_s layer, as shown in figure 2.4, where the SIP density swings up and below the DCP observed density. However, this does not explain the total absence of DCP response on the upleg and its low response on the downleg within the lower E_s layer.

Sternovsky et al. [64] have shown that the presence of charged aerosols in the mesosphere can lead to a charged rocket wake affecting E-field or floating probes. The characteristics of this charged wake are dependent on the polarity of the charge on the aerosols and the amount of charge residing on the aerosols. The DROPPS mission observed that all of the negative charge was on the heavy aerosols, which led to charge separation between the ions, embedded in the neutral flow, and the aerosols that are not affected by the flow. This created a strong potential structure within the wake, which was observed by the E-field instrument. The SAL payload saw a completely different situation, in which a relatively small amount of positively charged dust (20 particles/cm^3) was observed coincident with the lower E_s layer. Electrons, being lighter, are assumed to follow both the ions and the positively charged dust particles, with the only charge separation being that attributed to ambipolar diffusion. Thus, we do not expect a charged wake as was observed in DROPPS. This is consistent with the absence of spin modulation in V1S data. In a charged wake the potential structure around the payload is correlated to the plasma density, thus a spin modulation in V1S similar to the SIP data would have been consistent with a DROPPS like charged wake.

The reduction in current collected by the DCP in the lower E_s layer must be due to negative charging of the payload, more than the three volts bias on the probe, so as to remove the DCP from operating in the electron saturation region. Figure 2.9 focuses on the 90-93 km altitude range and presents all three instrument datasets for correlation. Once again, spin modulated SIP density data is observed within the E_s, while the DCP completely misses this layer. The V1S data suggests payload charging in the region where the DCP did not respond, with a peak differential charging at 2.5 volts on the upleg and

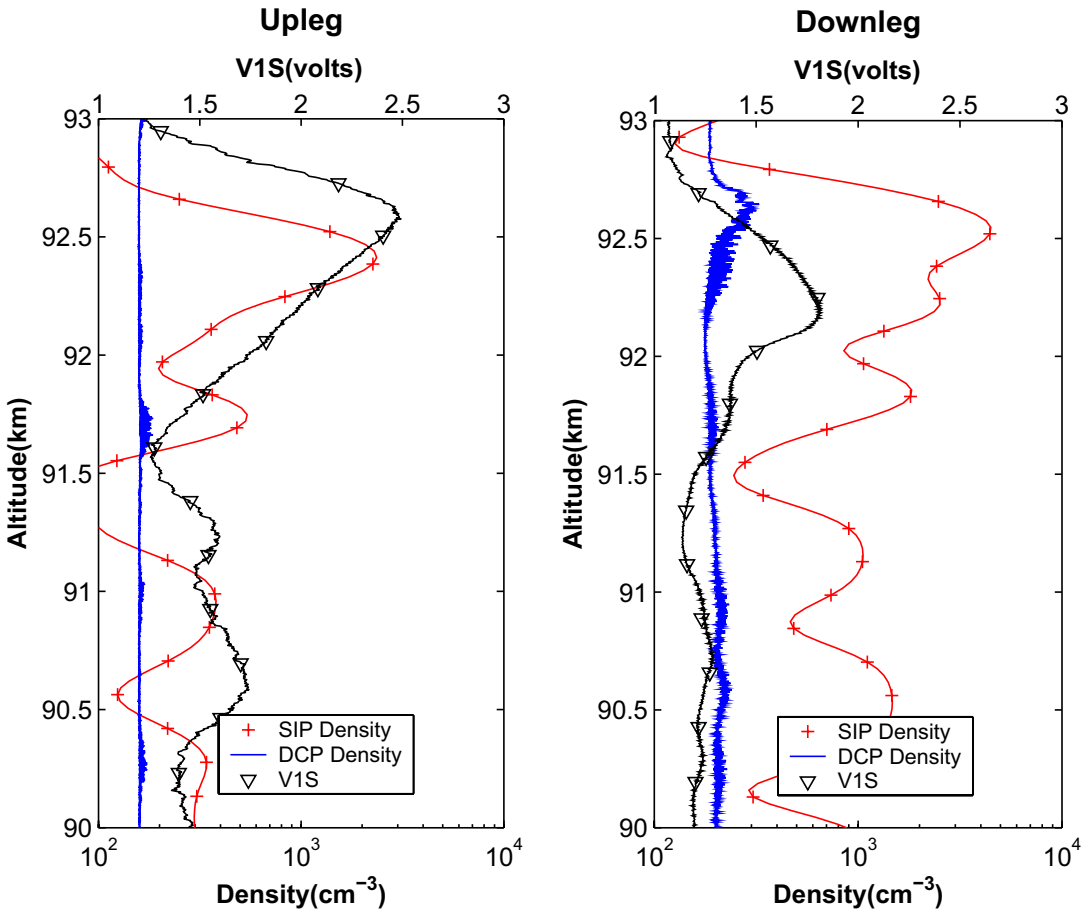

Fig. 2.9: Profiles of SIP and DCP electron densities and V1S potential between 90-93 km.

1.8 volts on the downleg. This observation, along with the indication by the DCP that the payload surface was more than three volts negative, indicates that both the carbon coated sensor and the payload surface experienced a negative charging event, with the payload surface charging more. The difference in their levels of charging could be due to differences in shape and surface work function.

We used our circuit model to simulate the charging of the payload along with the DCP and V1S instrument responses. The plasma density at the location of the DCP and the floating sphere was estimated within the wake by scaling the SIP density with the results of the DSMC simulation. We started with the simplest model, considering only ions and electrons without capacitive contamination effects, charge dust, or triboelectric current sources. This basic simulation did not show any significant levels of payload charging in the

lower E_s layer. On the other hand, modeling the ions as a pure ram current led to severe charging throughout the entire layer and did not produce the observed V1S data profile. The inclusion of various capacitance and resistance values to account for the contamination and sheath effects on the probe and payload surfaces also did not produce the observed DCP and V1S profiles. We approximated the positive charged dust density based on data from the charged dust detector and used it in the simulation. But as the charged dust density was only 20 particles/cm^3, the effect of this charged dust current source was also not enough to produce the required DCP and V1S profiles. Thus, we conclude that an additional triboelectric current source from neutral dust in the mesosphere is needed to explain the sudden payload charging within the 92.5 km layer.

Estimating the density of neutral dust responsible for triboelectrification is problematic due to the lack of observations of the dust composition. One may assume that most of the metallic dust material encountered by the payload existed in an oxidized state and thus little triboelectric charging would be expected against the payload's oxidized aluminium surface due to similar work functions. Yet, both in situ and ground based observations indicated the strong presence of atomic sodium. Sodium may have been adsorbed on the dust surface in its atomic form and could have been the reservoir for Na_s layer, as has been hypothesized elsewhere by von Zahn et al. [48]. Such dust would supply an additional current due to work function differences. There is a possibility that other higher work function metals might have supplied an opposite current, but the net current required to produce the observed charging must have come from low work function metals. The triboelectric current density required to reproduce the DCP and V1S response is presented in figure 2.10, along with the in situ observations of sodium volume-emission-rate [39]. We note that this current is located below the stronger Na_s signature and within the E_s layer observed by the SIP. This vertical separation of the atomic sodium from the neutral dust responsible for triboelectrification of the payload could be due to neutral winds or gravity waves and might also justify the separate life times of the E_s and Na_s layer [65].

The simulation results including triboelectric charging effects are shown in figure 2.11.

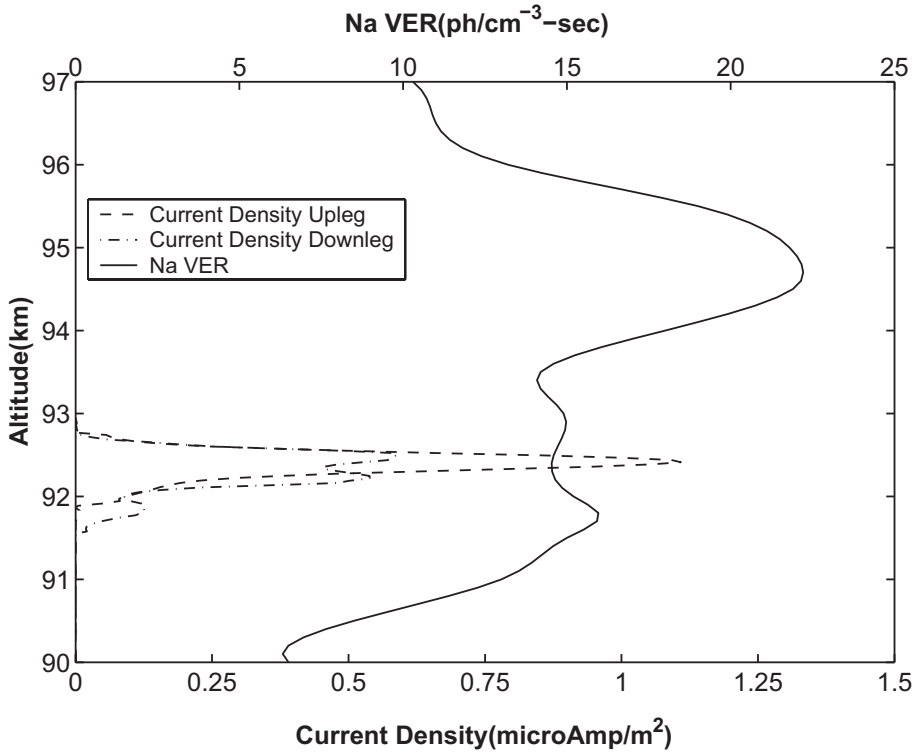

Fig. 2.10: Required triboelectric current density along with in situ observed Sodium volume-emission-rate (VER).

The factor used to normalize the flight DCP data to the SIP density at 114 km was also used to normalize the charging model's DCP current. Furthermore, we also simulated a noise floor of 16×10^{-9} amperes that shows up as the instrument sensitivity floor at about 150 e/cm^3. The V1S data from the simulation is expected to be only an approximate match to the observed data throughout the entire 90-93 km altitude region due to spin phase wake differences in ambient density seen at the V1S sphere which was deployed in a different direction than the SIP. We did not model this temporal (and thus altitude) spin phase difference for the charging calculations of the V1S sphere.

The simulation derived the additional current required to generate the observed DCP and V1S profile. If we simply correlate this triboelectric current as a single charge transfer from a solitary dust particle, then the required neutral dust layer has peak density that is on the order of several thousand particles/cm^3, which is on the same order as predicted by the Hunten model [66] for sub-nanometer mesospheric smoke particles between 90-95

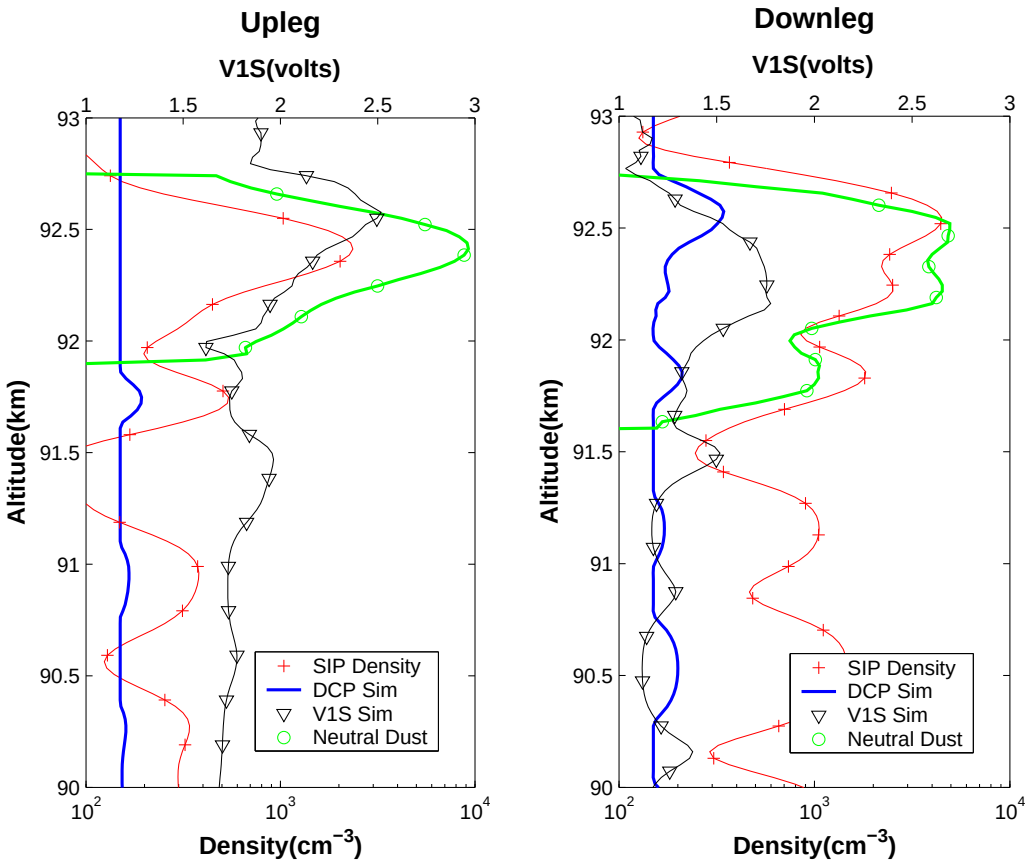

Fig. 2.11: Charging model simulation response of DCP and V1S along with effective neutral dust density producing triboelectric charging.

km. Although the model is widely accepted, these neutral smoke particles have never been directly observed and measured in situ, and their density should vary with meteoric activity and neutral winds. What is surprising is that the triboelectrically reactive component of the dust was confined to an altitudinally narrow band. The neutral dust could well have existed over a much broader altitude range, as predicted by Hunten's model, but the compositional variation of the dust could have been responsible for the thin altitude feature that we observed. This thin triboelectrically reactive neutral dust layer was within the broader (5 km) charged dust layer observed by the charged dust detector. This in turn implies that for some reason there was a higher concentration of adsorbed sodium or other low work function metal on the neutral dust, right where the E_s layer existed. The difference in the layer density and altitude spread between upleg and downleg is possible as there was

a horizontal distance of about 50 km between the two legs of the flight trajectory as the payload passed through the lower E_s layer. The absence of triboelectric charging of the payload within the 114 km layer was likely due to little or no neutral dust presence at that high an altitude, which is corroborated by the fact that no charged dust was observed around that layer.

One might ask whether or not this phenomenon has been observed before. At this point it is important to note again that contact electrification is an unpredictable process that is hard to precisely replicate even in laboratory conditions [16, 62]. Thus, depending on the ambient neutral dust density, the major metallic composition of the neutral dust particles, and the difference between the major neutral dust constituent and the payload surface metal one could expect varying positive or negative charging results. Triboelectrification may have occurred on four recent sounding rocket flights from Poker Flat, Alaska, the results of which have been published earlier by Gelinas et al. [67]. Although these flights were flown into layers of metallic composition, the layers were not sporadic atom layers. Within these metallic layers, the Sodium density was about a factor of four lower than the Iron density (refer figure 5 in [67]). If we are to assume that both of these metal layers had mesospheric dust as their source, then Iron should have been the major constituent of the neutral dust on that night. Considering simply the work functions of aluminium ($\phi_{wk} = 4.2$ eV) and iron ($\phi_{wk} = 4.67$ eV), it is possible that the sudden bumps in the electron density profiles were generated by triboelectric charging of the payload and the charging would be in the opposite direction to what was observed on SAL flights. This shift of payload potential would have put the DCP further in electron saturation region, thus increasing the current observed.

Another significant implication of our analysis is that if the DCP on SAL payload had been more sensitive and observed currents down to $1{\times}10^{-11}$ amperes, we might have seen a "bite-out" in the electron density profile, even though the SIP and ground based datasets showed a sporadic-E layer. Arguing that these layers are patchy by nature, one cannot compare in situ observations with ground-based observations, unless they were made over

common volume. Thus, it is important to fly a fairly high resolution absolute electron density probe, such as the SIP, in order to correctly interpret the high resolution relative density profile from Langmuir type probes.

2.4 Summary and Conclusion

In this paper we have presented data from an RF Impedance Probe, a fixed bias DC Langmuir Probe, and a payload skin floating potential measurement on a sounding rocket flight investigating mesospheric sudden atom layers. We have used Balmain's theory for antenna in cold magnetoplasma to derive absolute electron density from the RF Impedance Probe data, and subsequently, used those to calibrate the fixed bias DC Langmuir Probe to derive high-resolution relative electron density. The coupled observations made by the three instruments presented in this paper imply very interesting payload charging dynamics that lead to anomalous DCP behavior. We have then developed and presented a charging circuit model and applied it to the sounding rocket payload. After investigating various reasons for the anomalous DCP behavior, including a detailed study of the neutral wake, we have concluded that the triboelectrification of the payload surface from mesospheric neutral dust was the reason for the anomalous DCP response.

Besides the SAL dataset, we have also discussed the phenomenon of triboelectrification of payload surface for another mesospheric sounding rocket campaign. Both of these datasets clearly indicate the importance for considering the effects of triboelectrification on the interpretation of Langmuir-type probe datasets in presence of dusty plasma. The circuit model simulation derived neutral dust density layer has a peak density that corresponds well with the existing theory. It is thus possible that triboelectrification effects may also be used as an instrumentation technique for observing the neutral dust composition, as well as neutral dust density.

Chapter 3

Floating Potential Measurement Unit Aboard the International Space Station: II. Data Analysis

3.1 Introduction

The Floating Potential Measurement Unit (FPMU) was developed by Utah State University's Space Dynamics Laboratory (USU-SDL) to study surface charging of the International Space Station (ISS). The surface charging of the ISS is a complex problem owing to its large size, its unknown conductive/dielectric areas, and the exposed interconnects on its high voltage solar arrays. Not only is severe charging of the ISS a hazard for astronauts on Extra Vehicular Activity, but any resultant surface arcing can lead to functional anomalies and surface degradation on the ISS. Thus, the FPMU was developed under intense oversite and reporting requirements as it was deemed critical for ISS safety operations.

Although the primary purpose of the FPMU remains to monitor charging levels of the ISS and provide a dataset that can be used to validate the ISS charging models [68], a secondary purpose is the measurement of electron density and temperature within the F-region of the ionosphere to aid in the understanding of why the ISS charges. Unfortunately, the FPMU is not operated continuously. It is activated by ground commands and data is recorded only for specific data campaign durations. Thus, it is essentially a "snapshot" instrument for ionospheric density and temperature measurements.

Presented in the remainder of this section is a brief overview of the FPMU instrument suite. The next section presents the acquired data quality and the steps taken to compensate for noise and errors. This is followed by descriptions of the data processing algorithms to reduce the acquired data to plasma parameters such as electron and ion density (n_e and n_i) and electron temperature (T_e). We conclude the paper with a discussion and comparison

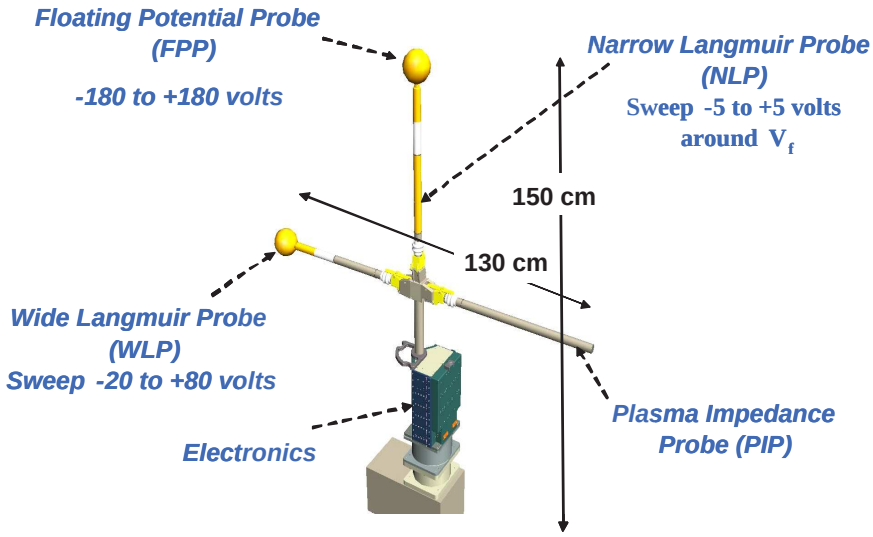

Fig. 3.1: Floating Potential Measurement Unit (FPMU) conceptual instrument layout.

between the FPMU derived plasma parameters and those derived from the International Reference Ionosphere (IRI) model and the Utah State University - Global Assimilation of Ionospheric Measurements (USU-GAIM) model.

As illustrated in figure 3.1, the FPMU is an instrument suite comprising of four separate instruments. Three of the instruments are based on Langmuir probe or DC electrical properties, while a fourth instrument is based on the radio-frequency (RF) properties of the probe.

The Floating Potential Probe (FPP) is a gold-plated sphere of radius 5.08 cm. The sphere is isolated from the chassis ground by a high impedance circuit $\geq 10^{11}$ ohms. The FPP measures the ISS floating potential ($\phi_{f_{ISS}}$) at the FPMU location within a range of -180 to +180 V at 128 Hz. The Wide-sweeping Langmuir Probe (WLP) is also a gold plated sphere of radius 5.08 cm and is swept with a triangular wave from -20 to +80 V relative to the chassis ground (i.e. the ISS structure) in 2048 voltage steps. The up-sweep is followed by a down-sweep of equal amplitude and sample length. The current resulting from the applied voltage sweep is measured on two different 12-bit channels: the low-gain channel and the high-gain channel. While the high-gain channel has sufficient sensitivity to observe both photo emission and ion collection currents, the low-gain channel is optimized

for observing thermal electron currents. The Narrow-sweeping Langmuir Probe (NLP) is a gold-plated cylinder with radius 1.43 cm and length 5.08 cm. The NLP is placed mid-way on the boom supporting the FPP and is guarded on each side by gold-plated cylinders with radius 1.43 cm and length 10.2 cm that are swept in synchrony with the NLP. A sweep from -4.9 to +4.9 V, in 512 equal steps, is applied to the NLP during one second, followed by a sweep down from +4.9 to -4.9 V the next second. This sweep voltage is referenced to the floating potential as measured by the FPP. Thus, even this small sweep range should cover the electron retardation region and some electron saturation region, enabling determination of n_e and T_e at 1 Hz. The resulting current is again measured on two channels with different gains.

The Plasma Impedance Probe (PIP) consists of an electrically short dipole antenna that is electrically isolated from the ISS. It is operated in two different modes. In the Plasma Sweeping Probe (PSP) mode, the instrument measures the electrical impedance (magnitude and phase) of the antenna at 256 frequencies over a 100 KHz to 20 MHz range. In the Plasma Frequency Probe (PFP) mode, the antenna tracks the frequency at which an electrical resonance associated with the upper-hybrid frequency occurs.

To avoid any interference between individual instruments the probe surfaces were set at least two Debye lengths apart for a worst-case rarified and cold ionospheric plasma. The tip-to-tip distance from the WLP to the PIP is 130 cm and the whole instrument stands about 150 cm tall. The FPMU interfaces with the ISS through the Video Distribution System (VDS) similar to an External TV Camera Group on the ISS. Thus, essentially the structural, electrical and communication interfaces of the FPMU with the ISS replicate an external video camera.

The FPMU was carried to the ISS on STS-121 and deployed on August 3, 2006, on the starboard (S1) truss of the ISS. There have been four data acquisition campaigns to date: August 3-9, 2006, January 22-30, 2007, March 1-3, 2007, and May 3-4, 2007. Only the results from August 2006 and March 2007 campaign shall be presented in this paper.

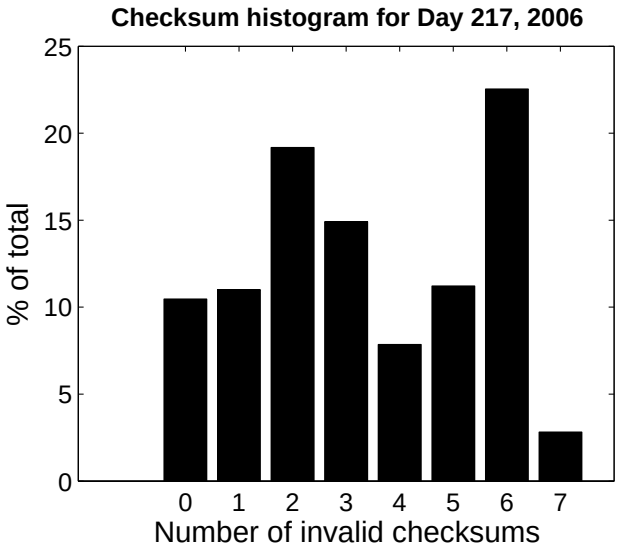

Fig. 3.2: Histogram of the number of invalid checksums when recalculated over the received page on the ground station. A value of 0 means all seven checksums were valid and the page were received uncorrupted.

3.2 Data Quality and Pre-processing

There are several factors that affect the quality of the FPMU dataset. We shall look at three different noise and error sources: telemetry system errors in data transmission and decoding from the ISS VDS, noise due to interference from other systems on the ISS, and errors due to contamination or non-uniform work function of probe surface.

Data from the FPMU is formatted and distributed as a video signal through the ISS VDS and is recovered at the NASA Johnson Space Center's ISS control center. In order to detect any noise induced in the data during transmission, the FPMU telemetry page has inbuilt checksums. Each telemetry page is divided into seven frames with a 32-bit CRC checksum calculated for each frame onboard the ISS and included within the frame. Thus, the first indication of noise in the dataset (noise that is not instrument related) comes when the checksum value included within the frame does not match the checksum value calculated on the ground for the received frame. Figure 3.2 shows a histogram of the number of invalid checksums per telemetry page for day 217 (August 5^{th}) 2006. Only 10.4% of the received telemetry pages were uncorrupted. An example of dataset from all four instruments for a telemetry page with six out of seven checksums being invalid when recalculated on the

ground station is shown in figure 3.3. As can be seen most of the noise in the WLP and the NLP I-V curves seems to be a bit-slip, hence, doubling (sometimes quadrupling), or halving the actual value. The telemetry noise for the FPP one second dataset shows the value to rail to the bottom of its operating range, i.e. -180 V. The telemetry noise in the magnitude channel of the PSP appears to be random.

We mitigate the effect of this noise by running a 7-point median filter through the WLP, NLP, and PSP sweeps. The FPP was sampling the ISS floating potential at 128 Hz. We reduce the sampling to 1 Hz by running a median filter over the entire one second sample set. The resultant filtered data is shown in green in figure 3.3.

Even for sweeps that were not affected by any VDS induced noise (i.e. all onboard calculated checksums were valid after reception at ground), the electron saturation region for the WLP and the NLP I-V curves is still noisy for intermittent time periods. Figure 3.4 shows unfiltered I-V curves from two different time periods for telemetry pages with all seven valid checksums. The I-V curves from 12:20:45 UTC are noisier than those from 06:58:26 UTC. We believe this noise to be due to interference from some other apparatus or activity onboard the ISS that occurs intermittently, thus, also affecting the FPMU intermittently. Any effect of this noise seems to be significant only for the electron saturation region and we expect to be able to derive plasma density and temperature from the ion saturation and electron retardation region without any significant problems.

It is interesting to note that the cylindrical NLP shows a "negative" characteristic in electron saturation region at the very top of the sweep for the curve from 06:58:26 UTC. This feature is observed in both the up-sweep as well as the down-sweep over long periods of time. Dote and Amemiya [69] have reported on such "negative" characteristic observations for cylindrical probes in strongly magnetized (hundreds of Gauss) plasma chambers. Rubinstein and Laframboise [23] have also theoretically predicted this feature for magnetized plasmas dependent on the strength and alignment of the magnetic field. However, in both of those cases, the "negative" characteristic occurs at ϕ_p, while we observe it well into the electron saturation region. This phenomenon in electron saturation region has also been seen on two

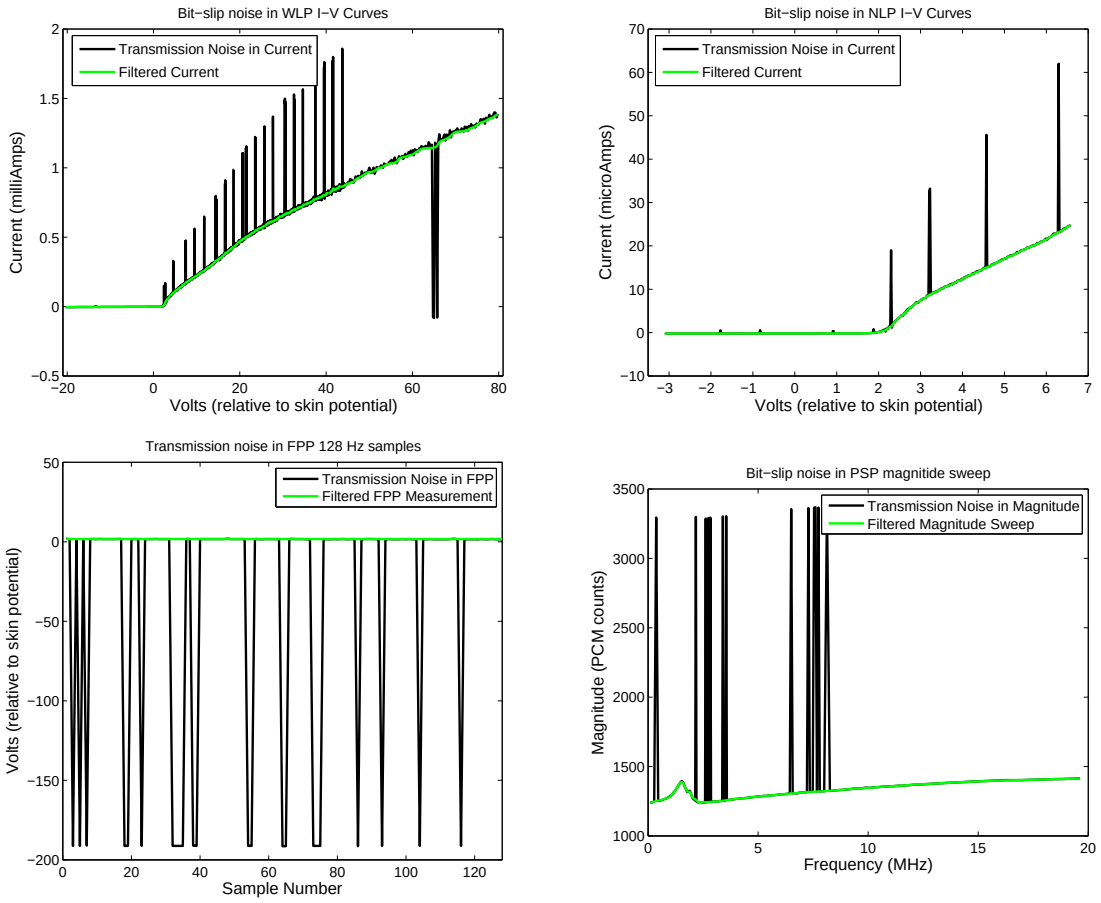

Fig. 3.3: Noise in the dataset of all four FPMU instruments due to telemetry errors. Median filtering mitigates most of the "spikes."

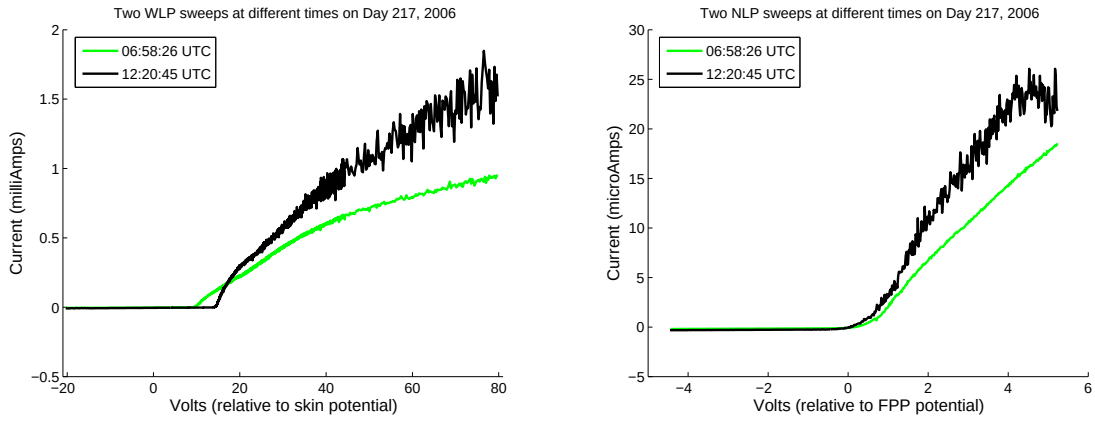

Fig. 3.4: Noise in the WLP and the NLP I-V curves possibly due to interference from some other apparatus or activity onboard the ISS.

separate rocket flights carrying heated cylindrical sweeping Langmuir probes [70]. At this time no satisfactory explanation for this phenomenon exists.

The effects of contamination and non-uniform work function of the probe surface on the measured I-V curves have been previously studied [22, 29]. The predominant effect has been described as the presence of hysteresis in the I-V curves as the voltage is swept up and down in a triangular waveform. This hysteresis is indicative of a disturbed retardation region leading to anomalously high electron temperature retrievals. Both the WLP and the NLP were gold plated to provide a uniform work function for the probe surface as well as to provide some stability in the corrosive atomic oxygen environment of Low Earth Orbit. Additionally the WLP can be heated with a small halogen lamp that was placed inside the hollow sensor sphere. The lamp is powered on and off from ground commands. The temperature of the WLP surface is a function of solar beta angle to the ISS. Without internal heating the temperature of the WLP surface will range from -58°C for low beta to 118°C for high beta. When the internal heater is turned on the temperature of the probe will approach 350°C after several orbits. This heating was done to boil off any contaminants from the probe surface [31, 33]. Figure 3.5 shows four consecutive filtered sweeps from the WLP which clearly show the absence of hysteresis, and hence a clean probe surface. The NLP was not internally heated and is expected to clean its surface with heat from the Sun as well as ion sputtering due to the ISS orbital speed of about 7.4 km/sec. Figure 3.5 also

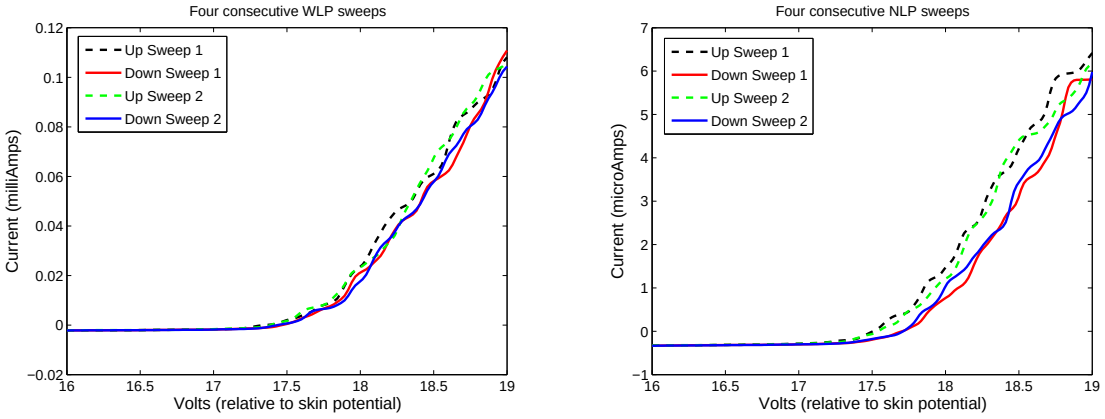

Fig. 3.5: Four consecutive I-V curves from the WLP and the NLP. There is no hysteresis in the internally heated WLP, while minimal hysteresis exists in the NLP indicating presence of some contamination.

shows four consecutive filtered sweeps of NLP at the same instant as that of the WLP. Only a minimal presence of hysteresis is visible in the NLP I-V curves.

3.3 Data Processing: Deriving n_i, n_e, and T_e from the WLP and the NLP Dataset

Langmuir probes were first used as diagnostic tools for plasma chambers by Irving Langmuir in the early 20^{th} century [5, 6]. Since then, the Langmuir class of electric probes has also been used on many sounding rockets, satellites, and inter-planetary spacecrafts to perform in situ measurements of plasma parameters such as electron density (n_e) and temperature (T_e), ion density (n_i), and as an indicator for spacecraft charging. We present a brief overview of the various analytic expressions that have been presented in the literature to describe the collected current by a Langmuir probe under various conditions. Unfortunately there are known limitations in the use of these expressions for flowing, magnetized and collisional plasmas, all of which are typically encountered when analyzing Langmuir probe data obtained from suborbital rockets and satellites. Detailed Langmuir probe theory can be read from several references [9, 12–14].

3.3.1 Review of Langmuir Probe Current Collection Expressions

The random thermal current to a surface for a charge species q_j primarily depends on the density (n_j), temperature (T_j), and mass (m_j) of the charge species, and the surface area (A) of the probe:

$$I_{th_j} = n_j q_j A \sqrt{\frac{k_B T_j}{2\pi m_j}}, \tag{3.1}$$

where k_B is the Boltzmann constant. While equation 3.1 governs the random current collected by a conducting surface at the potential of the surrounding plasma, a typical Langmuir probe collects current over a range of applied potentials. The resulting I-V curve can be divided into three regions of operation: electron retardation, ion saturation, and electron saturation. These regions are roughly divided by the plasma potential and the floating potential, and are named after the dominant collected charged species over that range of applied potentials. The plasma potential, ϕ_p, is the potential at which no electric fields exist between the probe and the plasma and the only current collected is the thermal current of the charge species, while the floating potential, ϕ_f, is the potential attained by a probe such that the total current of various charge species to the conducting surface sums to zero. The first region to be discussed is the electron retardation region that refers to the part of I-V curve that lies between ϕ_f and ϕ_p. In this region thermal electrons are repelled and ions are attracted. Despite being repelled, electrons are still the dominant collected species and the ions constitute only a minor portion of the collected current. For plasma with Maxwellian velocity distribution, the electron current in this region is exponential with probe potential and is scaled by the electron thermal current. It is given by

$$I_e(\phi) = I_{th_e} \exp\left(\frac{e(\phi - \phi_p)}{k_B T_e}\right), \tag{3.2}$$

where ϕ is the potential applied to the probe relative to ϕ_p, e is the fundamental electron charge and I_{th_e} is the electron thermal current given by equation 3.1. Note that the cur-

rent "from" the probe (i.e. electron collection) is referenced as positive in the presented equations.

The current collected in either the electron or ion saturation regions for a non-drifting, unmagnetized, and collisionless plasma is given by the Mott Smith-Langmuir Orbital Motion Limited (OML) theory [6] and is represented by

$$I_j(\phi) = I_{th_j}\left(1 + \frac{q_j(\phi - \phi_p)}{k_B T_j}\right)^{\beta}, \tag{3.3}$$

where

$\beta = 0$ Flat plate probe,

$\beta = 1/2$ Cylindrical probe,

$\beta = 1$ Spherical probe.

The parenthesized expression in equation 3.3 signifies the increase in collection current with the growth in effective collection area as the potential structure around curved probes changes when $|\phi - \phi_p| > 0$. It is important to differentiate this effective collection area from the term A in equation 3.1 which represents the physical surface area of the probe in contact with the plasma.

The saturation region theory becomes complicated as each of the above assumptions (non-drifting, unmagnetized, and collisionless) about the state of plasma are violated. In the case of spacecraft motion through plasma (i.e. plasma drift relative to probe) the thermal speed of ions is usually less than the spacecraft speed while the electron thermal speed is higher than the spacecraft speed. This situation is generally referred to as "mesothermal" plasma and primarily affects the ion saturation region. An approximate equation for the ion saturation current [20] is given by

$$I_i(\phi) = I_{th_i}\frac{2}{\sqrt{\pi}}\left(\frac{m_i v^2}{2k_B T_i} + \frac{1}{2} + \frac{q_i(\phi - \phi_p)}{k_B T_i}\right)^{\frac{1}{2}}, \tag{3.4}$$

where v is the spacecraft velocity, and ϕ is the applied probe potential. The first term is

the ion "ram" current and is the dominant term at orbital velocities. The other two terms refer to thermal motion and increase in collection due to attractive potentials, respectively. At orbital velocities the mesothermal situation creates a rarefied wake region behind the probe, thus, the surface area A in contact with plasma is the probe area projected normal to v.

Although one would expect that the electrons (having a much higher speed than the spacecraft) can still approach the probe from all directions, this is generally not so. The electrons can only penetrate into the ion wake region as much as ambipolar diffusion would allow, thus the mesothermal condition is expected to affect even the electron collection current. Katz et al. [21] have reported that for a mesothermal plasma a spherical probe collecting in the electron saturation region fits equation 3.3 with $\beta = 0.5$, which is unlike the value of β that OML theory predicts. Similarly, Piel et al. [22] also reported that their spherical probe observations aboard a sounding rocket fit equation 3.3 the best with $\beta = 0.58$.

With the addition of magnetic field the charged particle motion around the probe is constrained by the particle's gyro-radius and the alignment of the probe with respect to the magnetic field. The situation is best described as a "magnetic bottle" (see figure 6 of Rubinstein and Laframboise [23]). Parker and Murphy [24] first tackled the problem of current collection in magnetized plasma by neglecting particle thermal motion in addition to the assumption of nondrifting collisionless plasma. This effectively gives a canonical upper bound to the collected saturation current and is given by

$$I_j(\phi) = \frac{I_{th_j}}{2}\left(1 + \left(\frac{8\,|q_j(\phi - \phi_p)|}{m_j\omega_j^2 r^2}\right)^{\frac{1}{2}}\right), \tag{3.5}$$

where ω_j is the particle gyrofrequency and r is the probe radius. The calculation of the upper bound that includes the particle thermal motion is further complicated and was done by Rubinstein and Laframboise [23]. A simplified version in the limit of large attractive

potentials is given by

$$I_j(\phi) = I_{th_j}\left(\frac{1}{2} + \frac{1}{2}\left(\frac{8\left|q_j(\phi-\phi_p)\right|}{m_j\omega_j^2 r^2}\right)^{\frac{1}{2}} + \frac{k_B T_j}{m_j\omega_j^2 r^2}\right). \tag{3.6}$$

The first two terms are the same as Parker and Murphy equation. The last term is a result of orbital motion of the particles and vanishes for strong magnetic fields.

An asymptotic analysis of the effect of collisions in a non-drifting magnetized plasma has been done by Sanmartin [27]. However, due to the complexity involved, collisions in a magnetized plasma are generally ignored. Early computer simulation programs (NASCAP /LEO and POLAR) have shown the collisionless approximation to be good to within 5% [28] under low Earth orbit ionospheric conditions. The most complicated situation arises in the case of mesothermal magnetized plasma. Thompson's work on electrodynamics of conducting tethers in LEO [25] has treated this problem with a collisionless assumption, and shows that drifting effects cannot be ignored for electrons even if their thermal motion is much faster than the drift speed. There is however presently no theory for quantitative calculations of collected current in mesothermal magnetized plasma [26], short of a computer particle-in-cell (PIC) simulation.

3.3.2 Algorithm to Reduce the WLP and the NLP I-V Curves to Plasma Parameters

As discussed in the previous subsection, Langmuir probe theory is complex in the case of mesothermal magnetized plasma, a situation seen by probes on spacecrafts in low Earth orbit in the ionosphere. However, knowledge of the spacecraft orbital parameters and expected ionospheric plasma parameters can improve approximations during data analysis, thus making the problem tractable.

The ISS orbital speed is on an average about 7.4 km/s, its altitude is approximately 341 km, and the orbit inclination of 51.63 degrees is such that it rarely crosses into high latitude auroral conditions. The average thermal speed for O^+ ions at 2000 °K, a maximum expected

ion temperature at the ISS orbit altitude, is about 1.8 km/sec, which is significantly below the ISS orbital velocity. Thus, the predominant component of ion current at ϕ_p is expected to be the ram current. With the knowledge of the ISS velocity, probe cross section area, and the location of ϕ_p within the I-V curve, one can thus determine the ion density. The accuracy of the calculated n_i is limited only by the accuracy with which we determine ϕ_p. Furthermore, the accurate determination of temperature from the retardation region and determination of density from the saturation region are also significantly dependent on knowing the potential applied to the probe relative to the ϕ_p.

Thus, the single most important step in analyzing any Langmuir probe I-V curve is to first find the plasma potential, ϕ_p. In an ideal situation, ϕ_p is the point where the curve characteristics deviate from an exponential form, a point generally referred to as the "knee" in the I-V curve. However, both Sanmartin [27] and Rubinstein and Laframboise [23] have shown that in a magnetized plasma there is a decrease in collected current near the plasma potential thereby producing a "rounding of the knee" effect in the region where the I-V curve transitions from electron retardation to electron saturation region. Thus, determining ϕ_p as the last point that fits an exponential curve would be erroneous. Consequently we use an iterative procedure to determine ϕ_p.

In the first step we fit a line in the ion saturation region and subtract that from the total collected current. This approximately gives the electron collection current. We then take the first derivative of the electron current with respect to voltage. The location of the maxima within $dI_e/d\phi$ gives a very crude approximation of ϕ_p, akin to finding the "knee." We do not expect the plasma temperature to be larger than 5000°K, and thus we limit the search for the maxima to within 0.5 eV of ϕ_f, enough for the retardation region to transition into saturation region. The value of ϕ_f is determined by the point where the total collected current goes to zero. This limited point search avoids erroneous recognition of noise spikes that occur far from ϕ_f as the "knee." Subsequently, by equating the value of the ion saturation current linear fit at the location of ϕ_p to the ion ram current we get a first order approximation to the ion density.

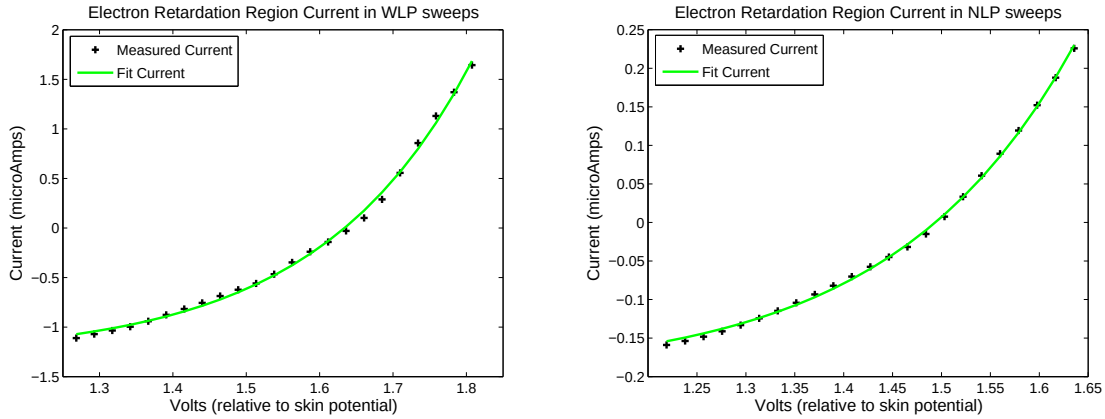

Fig. 3.6: Fits for T_e and ϕ_p to the electron retardation region using equation 3.7. Both the WLP and the NLP I-V curves are for the same second of data. The T_e and ϕ_p fits for the WLP I-V curve were 2420 °K and 2.12 V, while for the NLP I-V curve were 2670 °K and 2.01 V, respectively.

In the second step, we assume the plasma to be quasineutral and do a nonlinear least squares curve fit of the total collected current to

$$I_{total}(\phi) = -n_i e A V_{ISS} + I_{th_e} \exp\left(\frac{e(\phi - \phi_p)}{k_B T_e}\right), \tag{3.7}$$

which is just a combination of the ion ram current and electron retardation current, and where $n_i = n_e$, A is the probe ram projected area, and V_{ISS} is the ISS orbital velocity. This equation follows an idea similar to that behind equation 3.4. We use the density as calculated in the first step and fit equation 3.7 in a least square sense for only T_e and ϕ_p. This nonlinear fit is done only for points within ϕ_f-0.35 eV to ϕ_f+0.08 eV. The fit is done for the limited range of points because the farther positive relative to ϕ_f we go, the more the electron current is expected to deviate from an exponential form, and the farther negative we go the more the ion OML current becomes dominant. This nonlinear fit gives a much more accurate value of ϕ_p. Figure 3.6 shows the fits for typical WLP and NLP sweeps. We neglect photoelectron effects as it should only constitute a small current to the ion saturation region due to the expected high thermal plasma density at the ISS orbital altitudes.

We then further refine the value of n_i by evaluating the ion saturation current line fit at the ϕ_p determined in second step. Having now ascertained a much more accurate value of ϕ_p, we also make a second attempt at calculating the value of T_e by using the traditional method of line fits to the logarithm of the electron current for voltages below ϕ_p. This method generally corroborates the T_e values determined in the second step, however, the standard deviation of T_e values determined by this method is found to be slightly larger than that of values determined in the second step.

With the accurate knowledge of the plasma potential we can also compare the observed electron saturation region to the various current collection theories. Figure 3.7 compares the actual WLP and NLP I-V curves with the curves made from various current collection theories using the plasma density and temperature as derived in the previous steps. As is seen, none of the equations presented in the previous subsection even come close to the observed current. We then fit equation 3.3 to the observed current in a least squares sense for n_e and β using the values of T_e and ϕ_p as derived in second step. It is important to note that as per equation 3.3, the collected electron current is directly proportional to the density as well as the probe surface area A in contact with plasma. The accuracy of the fit for density, thus, depends on the accuracy of assumed surface area of the probe that is in contact with plasma. Initially the term "A" in the equation was taken to be the entire surface area of the probe. Although the subsequently acquired fit matched the observed current very well in the electron saturation region, the fit value of n_e is lower than the value of n_i that was calculated earlier. We believe this to be due to wake effects, wherein the portion of the probe surface that actually collects electrons is less than the entire surface area of the probe. Consequently, if we take the current collection surface area for the electron saturation current to be equal to only the surface area that is projected in the ram direction, then the value of n_e comes to within $\pm 10\%$ of the n_i value.

Thus, in the third step of WLP and NLP I-V curve data analysis, we derive electron density from the electron saturation region by fitting equation 3.3 for n_e and β assuming that only the projected probe surface area is in contact with plasma. The actual surface

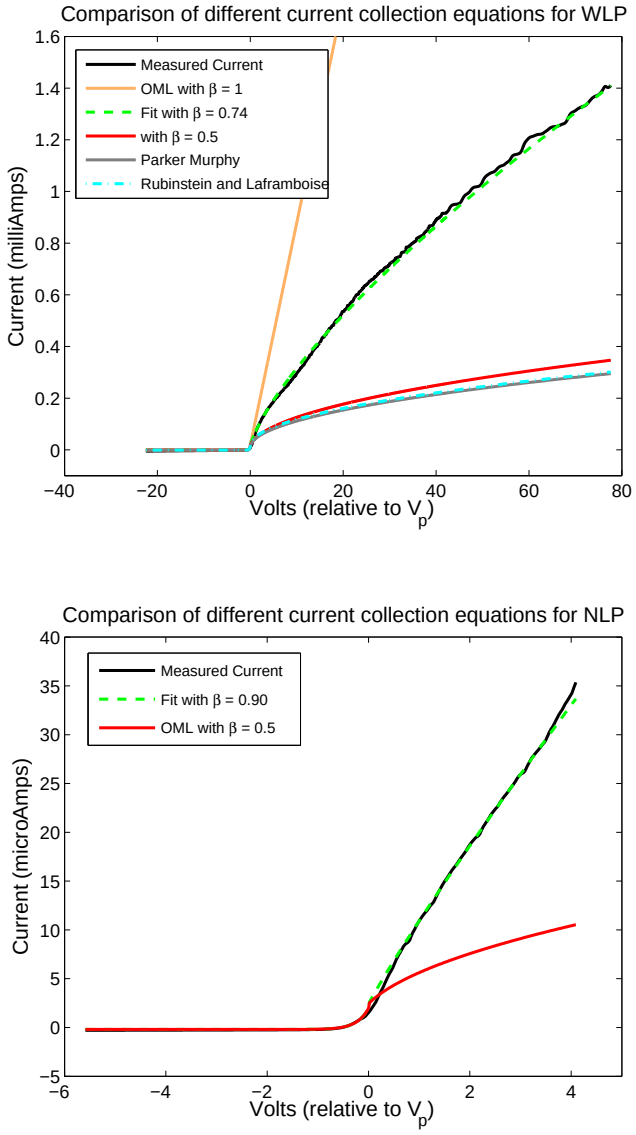

Fig. 3.7: Comparison of measured I-V curves with the I-V curves generated by analytical theory. The best match is acquired with a least squares fit of equation 3.3 to n_e and β. It is important to note that the fit value of β is different from that proposed by OML theory.

area that is in contact with plasma is expected to be larger than just the projected surface area due to minor ambipolar diffusion within the wake to the probe's anti-ram side. This additional area is assumed to be small but is expected to vary throughout an orbit. The value of n_e thus derived is not expected to be very accurate, unless a PIC simulation of wake effects is done to accurately determine the area in contact with plasma.

3.4 Data Processing: Deriving n_e from the PIP Dataset

The impedance characteristics of an antenna immersed in an ionospheric plasma were first used by Jackson [71] to determine ionospheric electron density in the late 1950's. Since then, there have been several significant efforts in further development of the theory [37, 72, 73] and in advancing the experimental technique [45, 50–52].

The principle behind the operation of an impedance probe is simple: the input impedance of an electrically short antenna immersed in a plasma varies and can be observed as the antenna is swept with a changing radio-frequency (RF) source. The observed impedance vs. frequency profile shows strong features as the antenna resonates with the fundamental plasma frequencies. The impedance profile achieves a minima near the electron cyclotron frequency, behaving like a series RLC tuned circuit, and achieves a maxima near the plasma upper hybrid frequency, behaving like a parallel RLC tuned circuit. The impedance vs. frequency profile along with an appropriate theory can then be used to determine various plasma parameters such as electron density, electron-neutral collision frequency, cyclotron frequency, etc. [45]. The most important benefit of an impedance probe is that the antenna input impedance is primarily sensitive only to the dielectric properties of the antenna and is largely independent of the grounding scheme as well as the surface properties of the antenna itself. The technique is thus immune to spacecraft charging.

The PSP operation mode of the PIP measures antenna admittance. An accurate calibration is required to convert the measured admittance (in PCM counts) to impedance in ohms. However, the calibration efforts for the PIP are still incomplete and maybe impossible. A crude measurement of plasma density can still be made based on the location of the parallel resonance (related to upper hybrid frequency) within the admittance profile. A single frequency sweep from the PSP operation mode of the PIP is shown in figure 3.8. As the PCM counts are a measure of the antenna admittance, the resonance related to the upper hybrid frequency shows up as a trough in the admittance vs. frequency profile. The assumption of upper hybrid frequency as the frequency at which the admittance trough occurs, along with an estimate of cyclotron frequency from the IGRF (International Geo-

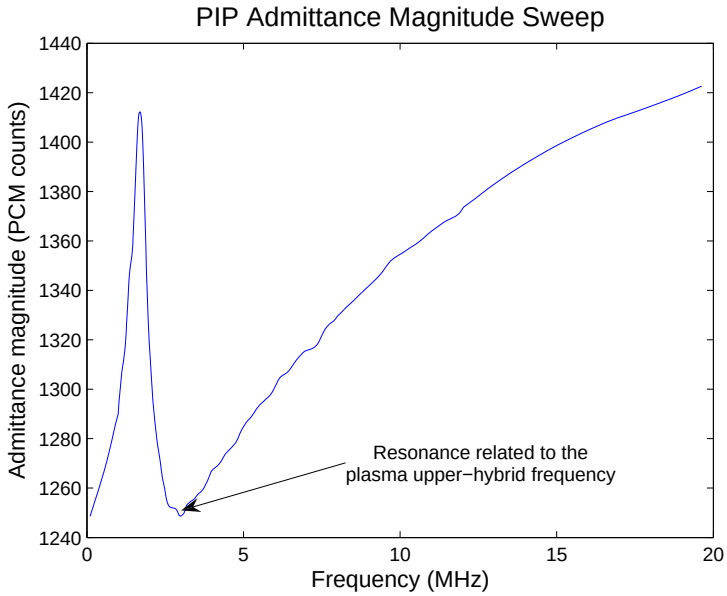

Fig. 3.8: A single admittance vs. frequency profile from the PIP dataset.

magnetic Reference Field) model, is then be used to determine a first-order approximation to electron density. The PFP mode of the PIP is also capable of giving high resolution electron density measurement once the phase locked loop gets locked on the upper hybrid resonance. However, the frequency locks on the upper hybrid resonance have been very sparse, and thus, no data from the PFP will be presented in this paper.

3.5 FPMU Data Analysis Results and Discussion

Figure 3.9 presents plasma densities derived from the WLP, the NLP, and the PIP over a several hour long segment on day 217 (August 5^{th}) of 2006. The data dropouts are a result of intermittent Ku-band downlink from the ISS. On August 5^{th} 2006, the acquisition of signal (AOS) was only 38%. The segment of time presented has one of the highest AOS to data drop-out ratio. The results from the analysis of the rest of the dataset are similar in nature. As the figures show, the Langmuir probe derived n_i and n_e values generally agree to within 10%, however, the n_i values have a slightly smaller standard deviation compared to the derived n_e values. This spread in n_e values is largely attributed to the changing collection area of the probes in electron saturation region as well as unavailability

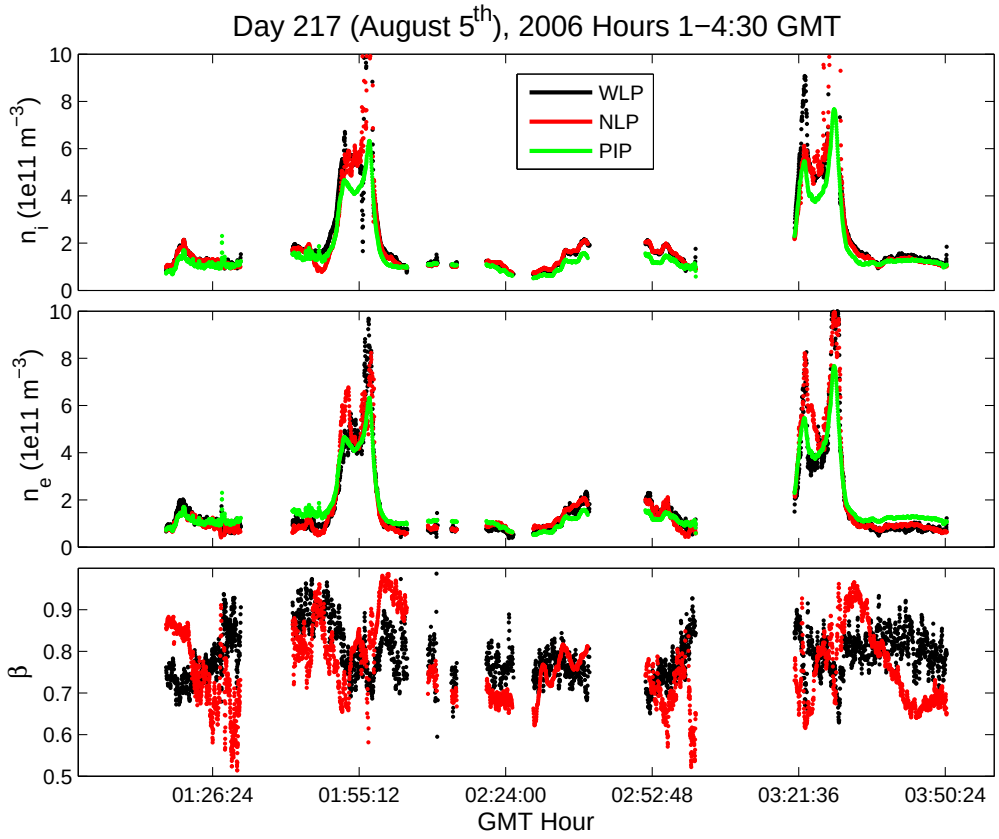

Fig. 3.9: Comparison of densities derived from different instruments.

of an accurate current collection theory. One measure of confidence we get in our method of least squares fitting for n_e and β over the electron saturation region is that both the WLP and the NLP give the same densities. This is despite the fact that the two probes are of different geometries and that their fits of β vary significantly over the range of 0.5 and 1. The seemingly random variation in the fit values of β indicates that the expression $\left(1 + \frac{e(\phi - \phi_p)}{k_B T_e}\right)$ is a poor representation of the growth in probe collection area with applied voltage. This can largely be attributed to the fact that the expression is for an isotropic potential distribution around the probe, while in reality, due to the plasma wake in the anti-ram side of the probe, the potential distribution is anisotropic. The large FPMU I-V curve database for two different probe geometries might be of help in determining a more accurate expression.

Although the method used to derive n_e from the PIP dataset is rather crude, the PIP

derived n_e generally agrees well with the Langmuir probe derived densities. While the PIP results can be used to confirm the density structure, the derived density itself is found to be always lower than that calculated by Langmuir probes. With the appropriate calibration of the PIP and the subsequent use of an impedance probe theory to derive the density, the PIP results are expected to improve.

The charging of the ISS is a function of ambient plasma density and temperature, as well as $V_{ISS} \times B$ induced potentials. A model of ISS surface charging, the Plasma Interaction Model (PIM), has traditionally used plasma densities and temperatures derived from the IRI model to predict the ISS charging levels [68]. The IRI empirical model [74] is an international project that provides users with global and temporal variations of electron density, electron temperature, ion temperature, ion composition (O^+, H^+, He^+, NO^+, O_2^+), ion drift, and Total Electron Content. However, the model only provides average climatologies of the ionosphere parameterized by solar activity, season and geomagnetic activity indices. Due to the nature of parameters the model is based upon, the actual day-to-day variability of the ionosphere can approach up to 30% of the model provided averages [3]. Thus, in situ instrumentation becomes important for high spatial and temporal resolution observations of local plasma parameters that should eventually be used to validate the ISS surface charging model PIM.

The USU-GAIM program is a newer physics-based model of the ionosphere that incorporates a Gauss-Markov Kalman Filter while assimilating a diverse set of near real-time ground based measurements [4]. Due to the data assimilative nature of the model it is expected to be more accurate in ionospheric specification than IRI. However, unlike the IRI model, the USU-GAIM model only provides global electron density and does not produce temperatures. As the USU-GAIM model is fairly new, the FPMU dataset provides an excellent triple redundant measurement of electron density for comparison and a model's validation. Figure 3.10 shows sites that provided the ground based ionospheric density measurements for assimilation into the GAIM model, the results of which are presented in this paper.

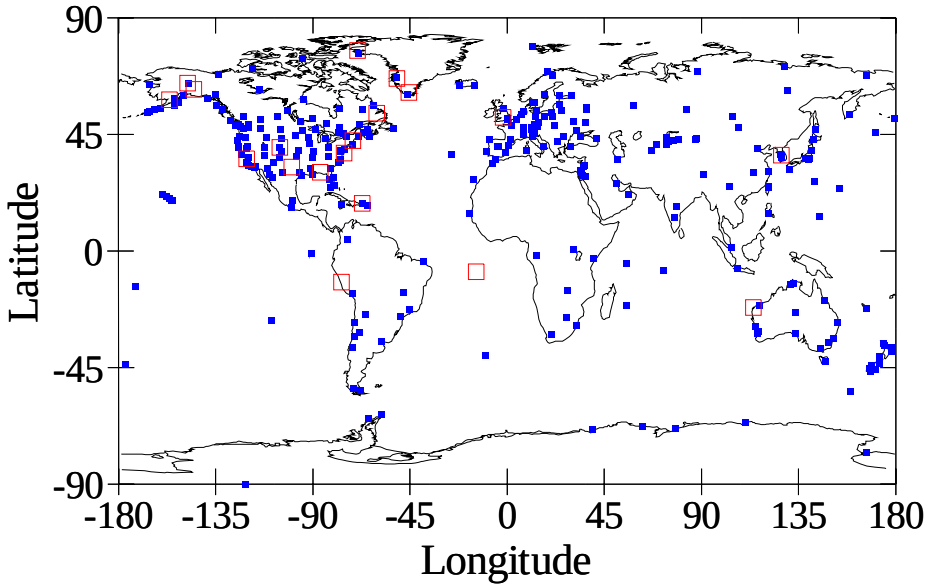

Fig. 3.10: Ground locations from where the data was assimilated into the USU-GAIM model run. The filled blue squares are GPS ground stations and red empty squares are ionosondes.

Figures 3.11 and 3.12 present data from the FPMU over two several hour long segments on day 217 (August 5^{th}) of 2006 and day 62 (March 3^{rd}) of 2007, respectively. The top rows in both figures show the ISS floating potential at the FPMU location on the ISS structure. Note that the ISS floating potential is plotted as "-$\phi_{f_{FPP}}$", which is a positive number. The figures also compare the plasma density and temperature derived from the FPMU with that generated using IRI and USU-GAIM models. Finally, the ISS latitude and longitude are also presented.

All three instruments (FPP, WLP, and NLP) give the same floating potential to within ± 2 volts, thus meeting the NASA requirements for FPMU success. There are a few outlier floating potential points derived from the WLP and the NLP and are assumed tobe due to noisy I-V curves. Between the two figures, there are three important characteristics discernible in the ISS surface charging: (1) $V_{ISS} \times B$ background due to the motion of ISS through the Earth's geomagnetic field, (2) charging due to additional electron collection on the exposed interconnects of solar cell panels as the ISS passes from eclipse to sunlight, (3) charging due to high densities and low temperatures of the Equatorial Anomaly as the ISS passes through Earth's geomagntic equator region.

The FPMU is located on the extreme end of starboard S1 truss. This location experiences varying degrees of charging due to $V_{ISS} \times B$ as the ISS attitude relative to the Earth's geomagnetic field changes over one orbit. As such, the maximum charging levels of the ISS surface are determined by the location of ISS eclipse exit within the charging profile of $V_{ISS} \times B$. In figure 3.11 the ISS eclipse exit occurs when the charging due to $V_{ISS} \times B$ is high, thus, taking the overall charging to about -25 V. While in figure 3.12, the eclipse exit occurs when the $V_{ISS} \times B$ charging at the FPMU location is only a few volts, thus, the overall charging level at eclipse exit in this case is only about -15 V, which is almost entirely due to additional electron current collection on the ISS solar panels. A future paper will delve more into the charging physics of the ISS surface along with PIM simulation results.

As expected, n_i values derived from the WLP agree more with USU-GAIM than with IRI. It is important to note that the USU-GAIM model employs a coarse grid, so the model peak tends to smooth, or average, the sharp anomaly peaks. This is most clearly seen in figure 3.12 where the model shows a tendency to fill in between the anomalies. The discontinuities in the GAIM density profile are a result of the way data is extracted from the coarse-grid global model. The model produces an electron density specification every 15 minutes. To plot the GAIM density profiles at the exact location of ISS, the density interpolation is done in position but not in time. Thus the extracted data uses the "closest" specification in time. A smooth transition could be obtained by interpolating between two time specifications, as well as in position space, but this hasn't been implemented yet.

Accurate measurement of T_e using Langmuir probes is always difficult. Ferguson et al. [75] analyzed a predecessor instrument suite on the ISS for electron temperatures and reported that the probe reduced temperatures were generally higher than that predicted by the IRI model. In the case of FPMU dataset, although the WLP and NLP derived temperatures have a little spread in values, the general trend does agrees well with the IRI model. At the same time the reduced data also provides small scale features that deviate from the IRI results which should be expected given the averaging nature of the IRI model [3]. For example see the feature around 0330 hrs of day 217, 2006.

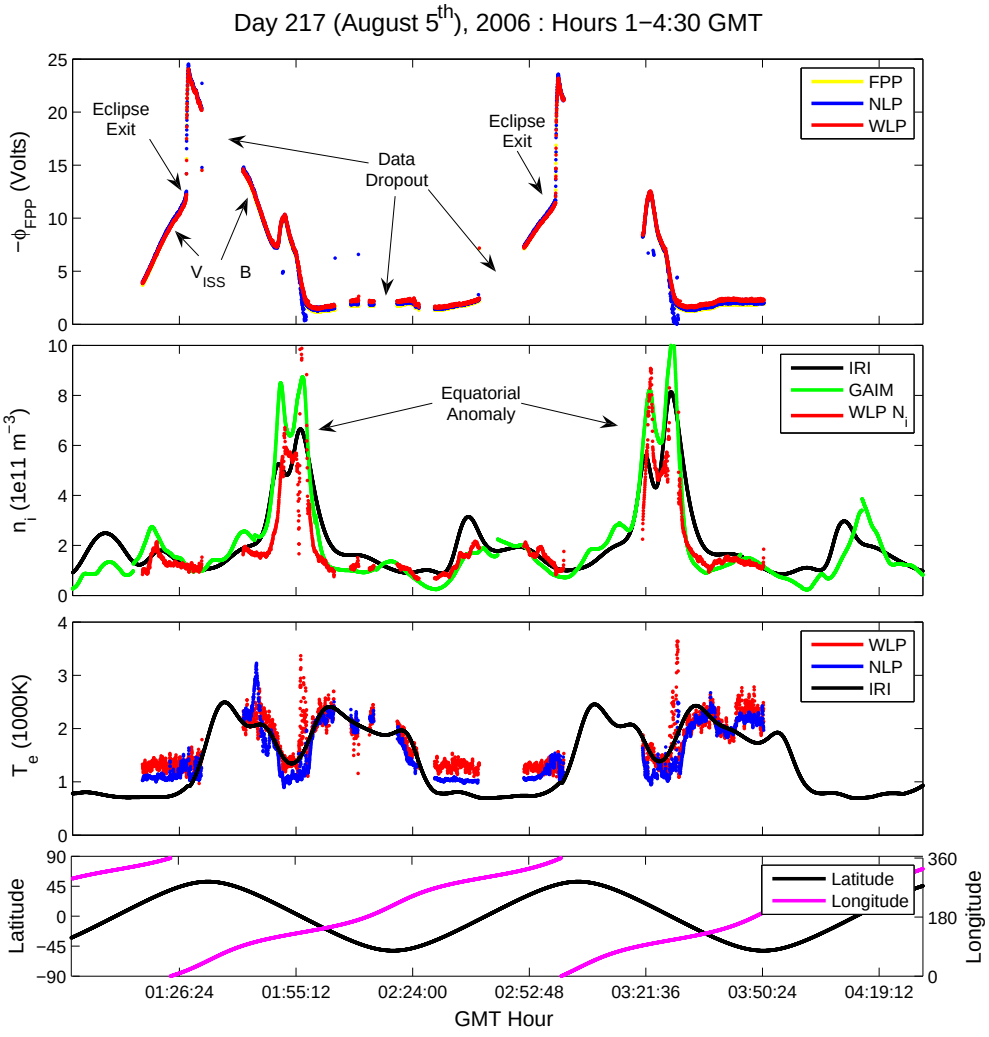

Fig. 3.11: The first row shows FPMU floating potential as measured by the FPP, the WLP, and the NLP. The second row compares the ion density (n_e) derived from the WLP with density from USU-GAIM and IRI model runs. The third row compares the WLP and the NLP derived temperatures with IRI model results. The fourth row shows the ISS latitude and longitude.

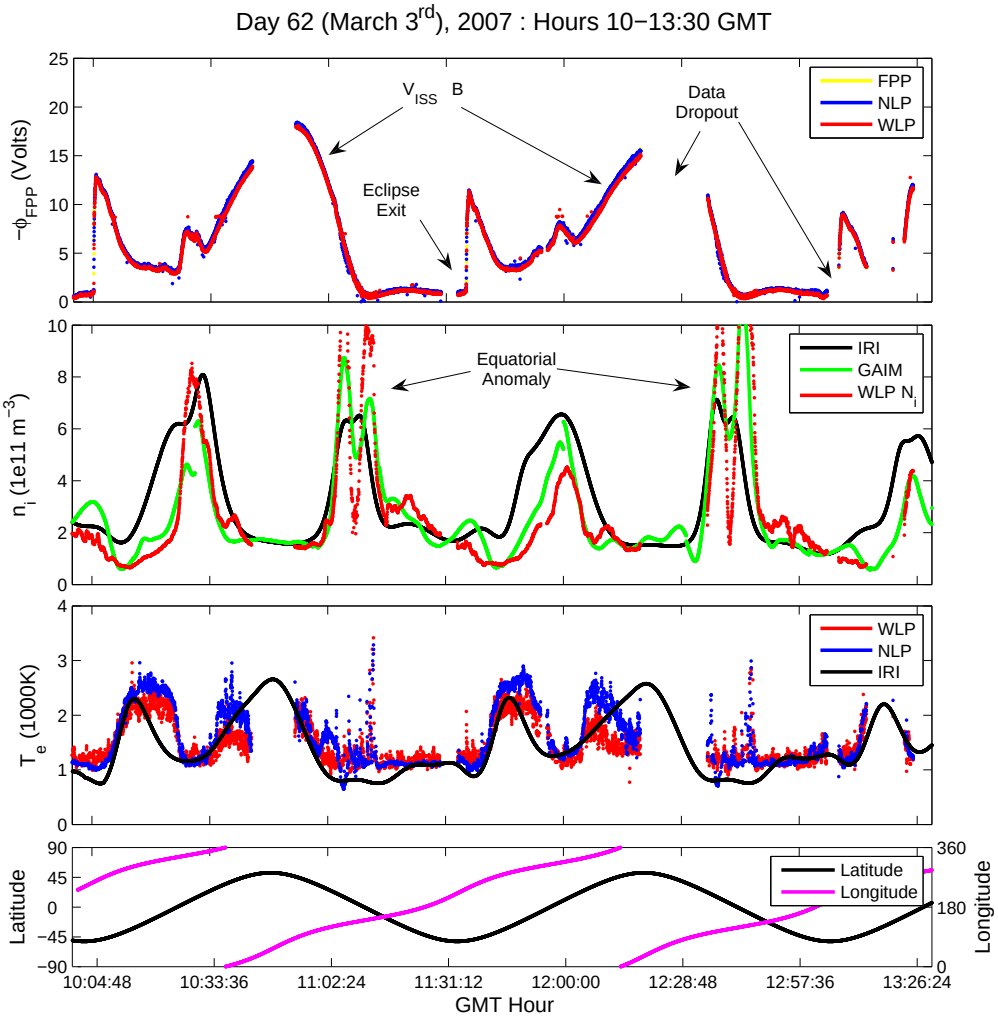

Fig. 3.12: The caption is the same as for figure 3.11.

3.6 Summary

The primary objective of the FPMU instrument suite was to provide a triple redundant, "no false alarm", measurement of the ISS floating potential. All three Langmuir probe instruments (FPP, WLP, and NLP) provide the ISS floating potential value to within ± 2 volts of each other, thus fulfilling NASA's requirement of FPMU. The n_i and T_e values provided by the WLP and the NLP also agree to within $\pm 10\%$ of both probes. This provides a doubly redundant measurement that can be used as an input for the ISS charging model or for validation of USU-GAIM model. The first results presented in this paper show that the in situ density measurements agree better with USU-GAIM than with IRI. The derived in situ temperatures are in good agreement with IRI predictions and also show small scale structures that are not visible within the IRI results due to the model's averaging nature.

The FPMU I-V curves from the WLP and the NLP also present an unprecedented dataset where two Langmuir probes of different geometries are probing ionospheric plasma in the same volume. As presented in this paper there is a lack of theory that can be used to accurately analyze the saturation regions of Langmuir probes in mesothermal magnetized plasma. Our analysis of the electron saturation region provides a simple procedure to derive absolute electron density. The accuracy of the derived electron density values is evident as they agree very well between the two different instrument geometries, as well as with the results from ionospheric models.

The seemingly random variation in the fit value of β points towards the lack of an accurate saturation region current expression. Furthermore, the NLP I-V curves intermittently show a "negative" characteristic in the far electron saturation region that remains unexplained. These topics will be investigated in a future paper. Thus, in the long run, the large FPMU I-V curve dataset shall shed a unique insight into probe physics.

Chapter 4
Derivation of Temperature and Density from Langmuir Probe Observations with a Small Surface-to-Probe Area Ratio

4.1 Introduction

The Langmuir probe has been the most widely used in situ instrument for the measurement of plasma parameters such as electron density (n_e) and temperature (T_e), ion density (n_i), and as an indicator for spacecraft charging [7–9]. Although the technique itself is simple and straightforward, the accuracy of derived plasma parameters is determined by the applicability of the theory used to analyze the data and the engineering quality of the probe. To date there has been no theory developed that can address any typical probe geometry in a magnetized mesothermal collisional plasma; the typical conditions experienced by a Langmuir probe in the ionosphere. While the limitations of the theoretical understanding of the probe physics can be overcome using appropriate assumptions or by exhaustive numerical kinetic particle simulations, the restraints imposed by the engineering design and implementation are harder to counter when reducing I-V curves to plasma parameters.

There are several challenges in engineering a Langmuir probe such that the probe's data is suitable for analysis. We briefly list a few here: (a) The most commonly used theory for Langmuir probe data analysis, the Orbital Motion Limited (OML) theory [9], assumes infinite planar probes, infinite cylindrical probes, and isolated spherical probes. Since this is not attainable in practice, it is typically countered by placing electrically isolated guard electrodes around the actual probe that are driven at the same potential as the probe. The guards help mitigate end and edge effects for finite probe systems. (b) Work function patchiness of the probe surface, due to the metal's own surface properties or because of

surface contamination, leads to hysteresis in the I-V curve as a probe sweeps up and down. This is known to affect the derived T_e measurements [22, 29]. This is countered by coating the probe with an inert conductive metal/alloy layer, such as gold, titanium nitride [30], rhenium, or molybdenum [7], and by employing in-flight cleaning of the probe surface to remove any surface contamination [31, 33]. (c) The instrument also needs to be designed to observe over the expected range of plasma conditions with sufficient resolution in the observations for analysis. (d) The probe needs to be physically deployed sufficiently far away from the spacecraft surface so as to not be influenced by the spacecraft wake or the plasma sheath around the spacecraft. (e) Finally, the probe, plasma, and the spacecraft chassis ground create a closed current loop. As a result, the surface area of the spacecraft has to be much larger than that of the Langmuir probe operating in the electron saturation region to provide for return ion currents to the plasma. If the area ratio of spacecraft surface to probe surface is not on the order of 1000 or greater, then the spacecraft floating potential will charge significantly negative to attract more ions to balance the electron current collected by the probe [34]. Boyd [76] lists several early Langmuir probe measurement attempts in space plasmas that were severely affected by inadequate payload surface area.

Of all the Langmuir probe design constraints, the hardest challenge in a sounding rocket payload is to ensure a favorable surface-to-probe area ratio. The probe cannot be made large due to the small payload skin area on a typical sounding rocket. This in turn limits the magnitude of current collection, thereby imposing strong requirements on the sensitivity and noise floor of the electronics. Within this paper we describe the data analysis of a sweeping Langmuir probe flown aboard two separate sounding rocket payloads where the ratio of the Langmuir probe area to that of the payload skin was about 250.

Presented in the next section is a brief overview of the rocket campaign and the details of the instrument suite. This is followed by the analysis of the payload floating potential and instrument behavior using a charging model implemented in SPICE (Simulation Program with Integrated Circuit Emphasis), a circuit analysis tool widely used by electrical engineers. We conclude the paper with a discussion and the data analysis of the I-V curves to derive

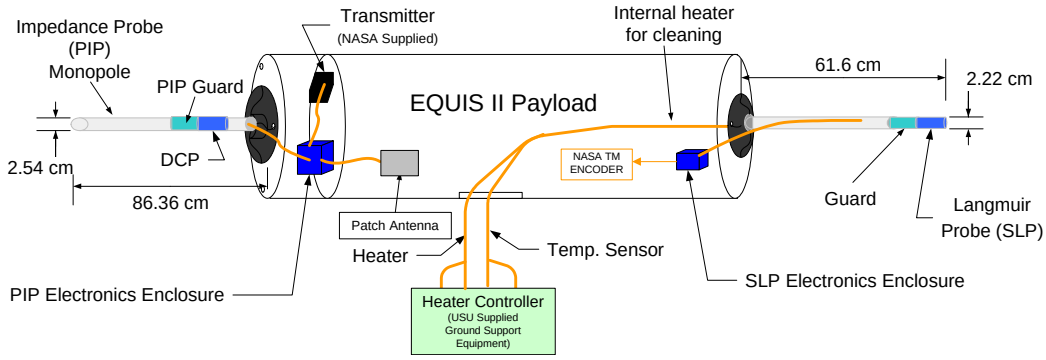

Fig. 4.1: The EQUIS II payload showing USU built instruments.

absolute plasma density and temperature.

4.2 Experiment Background and Instrument Description

The rocket investigation "Scattering Layer in the Bottomside Equatorial F-region Ionosphere" was part of the NASA EQUIS II campaign [77]. It was an investigation of the electrodynamics of the post-sunset equatorial F-region ionosphere and the bearing this has on the development of thin radar scattering layers that are observed in the bottom-side of the F-region ionosphere. These thin layers appear to be a precursor to equatorial spread F and are difficult to study with satellites due to their occurrence at low altitudes. The EQUIS II campaign was the first sounding rocket investigation of these layers. Two salvos of sounding rockets were launched from Roi Namur in Kwajalein atoll on August 7^{th} and 15^{th} of 2004. Each of the salvos consisted of one instrumented and two chemical release payloads. The instrumented rockets were launched westward into an equatorial spread F precursor that was first observed from ground using the Altair radar. The instrumented rockets reached an apogee of about 420 km. The instruments consisted of a Sweeping Langmuir Probe (SLP), a fixed-bias DC Langmuir Probe (DCP), a Plasma Impedance Probe (PIP) operating in two different modes: Plasma Frequency Probe (PFP) and a Plasma Sweeping Probe (PSP). All of these instruments were built at Utah State University (USU). The payload also carried four floating spheres as part of an Electric Field Probe (EFP) built by Penn State University.

Figure 4.1 shows a schematic of the payload representing only USU built instruments. The PIP boom was 86.36 cm long, 2.54 cm thick, and built out of aluminium. Of the total boom length, the last 50.48 cm were used as the monopole PIP antenna, making it electrically short for frequencies below 600 MHz. The antenna was used in two different instrumentation modes of the PIP. As a PFP, the instrument was used to lock-on and track the upper hybrid resonance of plasma with a phase-locked loop at a time resolution of 0.28 ms and a frequency resolution of 1 KHz. As a PSP, the instrument swept over a frequency range of 0.1 MHz to 20 MHz in 257 steps observing the antenna impedance in magnitude and phase. The entire frequency sweep was completed in 70 ms. An accurate calibration is needed to convert the digitized data in counts to impedance in ohms. The resultant frequency vs. impedance profile can then be analyzed with an appropriate theoretical model such as that proposed by Balmain to derive plasma density [45]. However, due to some engineering design issues the calibration of the PSP will require more calibration efforts and the results are not presented in this paper.

The DCP was a 5.08 cm long cylinder located at the base of the PIP boom. It was driven at +3 volts relative to the payload chassis ground to operate it in the electron saturation region. In order to keep the ion sheath around the DCP from interfering with the operation of the PIP (PIP being the higher priority instrument), the PIP was separated from the DCP by a 7.93 cm long cylinder that was electrically isolated from the PIP but operated at the same frequencies as the PIP.

The SLP was built out of aluminium with a length of 6 cm and a diameter of 2.22 cm. It was guarded on one side with an element of the same dimensions and at the same potential as the SLP. The combined probe and guard assembly was at the end of a 61.6 cm boom. With the exception of the probe and the guard, the rest of the boom was coated with a non-conductive paint. The SLP was internally heated via a cartridge heater for several hours before launch at $150°C$ to boil off surface contamination and was launched hot. The probe was swept in 549 equal steps from -1 to +5 volts relative to the payload chassis ground in a triangular waveform pattern at 25 Hz, giving 50 I-V curves every second.

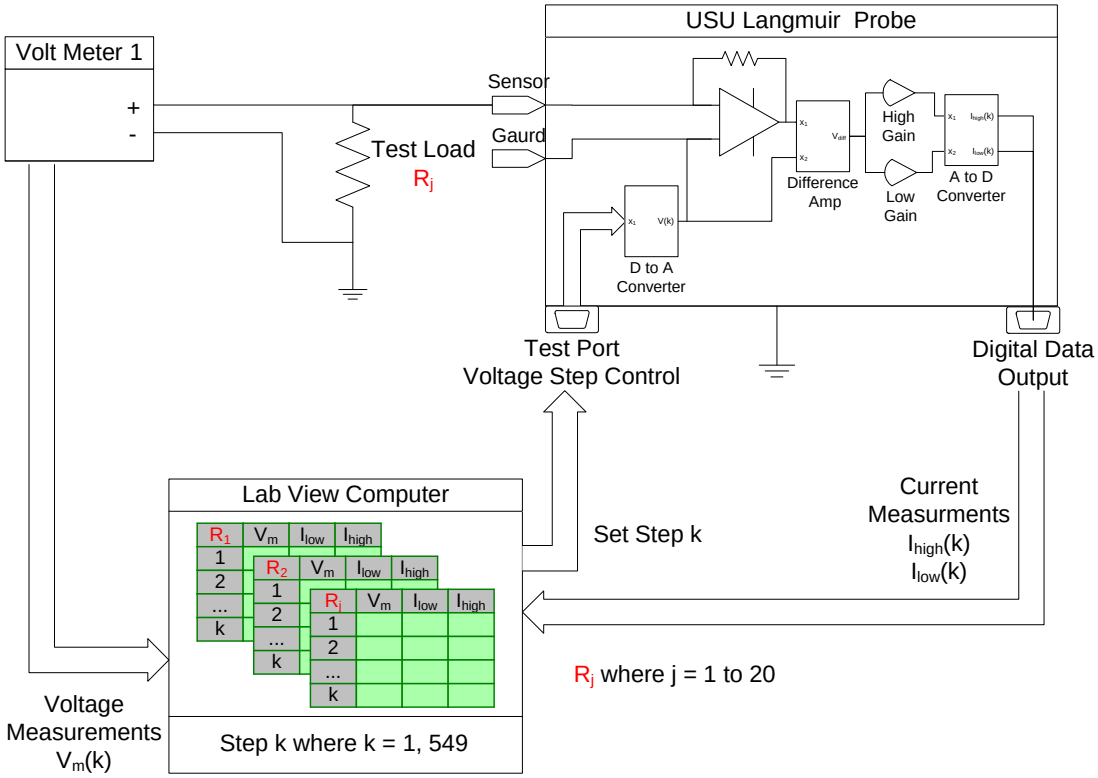

Fig. 4.2: Calibration setup for the SLP: At each applied voltage step, the potential across the resistor load was measured using a sensitive voltmeter and the observed current by the low gain and the high gain channels was recorded in PCM counts.

The instrument used 16-bit A to D converters and measured the current in two different channels: the High-Gain channel at a resolution of 57.9 pA/count with a range of 1.897μA and the Low-Gain channel at a resolution of 5.85 nA/count with a range of 191.6μA.

The SLP was meticulously calibrated in a thermal-vacuum chamber over a range of resistor loads and temperatures. The load values were chosen so as to exercise each of the gain channels through their entire dynamic range of operation. The calibration process is shown in figure 4.2. The SLP included a test port by which the voltage sweep of the instrument could be computer controlled. At each step of the sweep, the voltage across the resistive load was observed with a high-precision NIST traceable Keithley electrometer. The on-board temperature and current observations of the load under test were also recorded and the entire process was automated. The observed current in amperes was designed to be directly proportional to the measured PCM counts with an added offset. The calibra-

tion procedure determined the coefficients in the following equations, separately for both payloads and each gain channel:

$$V_{inst}(volts)[Step\#] = K_1[\#] + K_2[\#]I_{LowGain}(PCM) + K_3[\#]Temperature(^{\circ}C), \quad (4.1)$$

$$\begin{aligned} I_{LowGain}(amperes) &= \alpha_1 + \beta_1 I_{LowGain}(PCM), \\ I_{HighGain}(amperes) &= \alpha_2 + \beta_2 I_{HighGain}(PCM). \end{aligned} \quad (4.2)$$

The rocket actively controlled its attitude to align the spin axis parallel to the magnetic field while the rocket trajectory was nearly perpendicular to the magnetic field. Thus, the SLP and the PIP sensors were never in the payload wake with the booms transverse to the ram direction.

4.3 Understanding Payload Charging Through Simulations

We now develop a charging model for the EQUIS II (29.036 and 29.037) rocket payloads to qualitatively understand the charging due to small surface-to-probe area ratio. The model development is similar to the model developed by Barjatya and Swenson [45] for the Sudden Atom Layer rocket payload. Based on the OML theory, the ion and electron thermal currents (I_i, I_e) to a probe are given by

$$\begin{aligned} I_e(\phi) &= Ane\sqrt{\tfrac{k_B T_e}{2\pi me}}\left(1 + \tfrac{e(\phi-\phi_p)}{k_B T_e}\right)^{\beta} \\ I_i(\phi) &= -Ane\sqrt{\tfrac{k_B T_e}{2\pi m_i}}\exp\left(\tfrac{-e(\phi-\phi_p)}{k_B T_e}\right) \end{aligned} \qquad \phi > \phi_p, \quad (4.3)$$

$$\begin{aligned} I_e(\phi) &= Ane\sqrt{\tfrac{k_B T_e}{2\pi m_e}}\exp\left(\tfrac{e(\phi-\phi_p)}{k_B T_e}\right) \\ I_i(\phi) &= -Ane\sqrt{\tfrac{k_B T_e}{2\pi m_i}}\left(1 - \tfrac{e(\phi-\phi_p)}{k_B T_e}\right)^{\beta} \end{aligned} \qquad \phi \leq \phi_p, \quad (4.4)$$

where

A	Surface area	T_e	Electron temperature
n	Plasma density	e	Elementary charge
ϕ	Applied potential	ϕ_p	Plasma potential
m_e	Electron mass	m_i	Ion mass
k_B	Boltzmann Constant		
$\beta =$	0 for planar; 1/2 for cylinder; 1 for sphere.		

The current due to electrons is modeled as positive current and the current due to ions as negative current. Equation (4.3) models the electron saturation and ion retardation region, whereas equation (4.4) models the electron retardation and ion saturation regions. We also model the ion ram current by

$$I_{i_{ram}}(\phi) = -A_{ram} e n V_{ram} H[\varepsilon - e(\phi - \phi_p)], \tag{4.5}$$

where A_{ram} is the ram projected surface area, V_{ram} is the rocket ram velocity, and ε is $\frac{1}{2} m_i V_{ram}^2$.

Each of the above three current sources has been coded in SPICE as a voltage-controlled-current-source. All equations collectively make up a single sub-circuit model, as shown in figure 4.3. We model the contamination present on a current collecting surface as a parallel combination of a capacitor C_d and resistor R_d [22]. The sheath is modeled as another capacitance C_s in parallel with the current sources. The payload skin is modeled as a cylinder 194.31 cm in length and 35.56 cm in diameter, and the instruments are modeled with dimensions as presented in section 4.2. While the SLP was modeled without any contamination, the payload skin and the DCP were modeled with contamination. Another difference between the sub-circuit model used for the DCP, the SLP, and the payload skin is manifested by different collecting areas, which are passed to the sub-circuit in a function call. Figure 4.3 also shows the electrical circuit model of the entire payload as implemented in SPICE.

The model was run for a plasma density of $2.5 \times 10^5 cm^{-3}$ and plasma temperature of

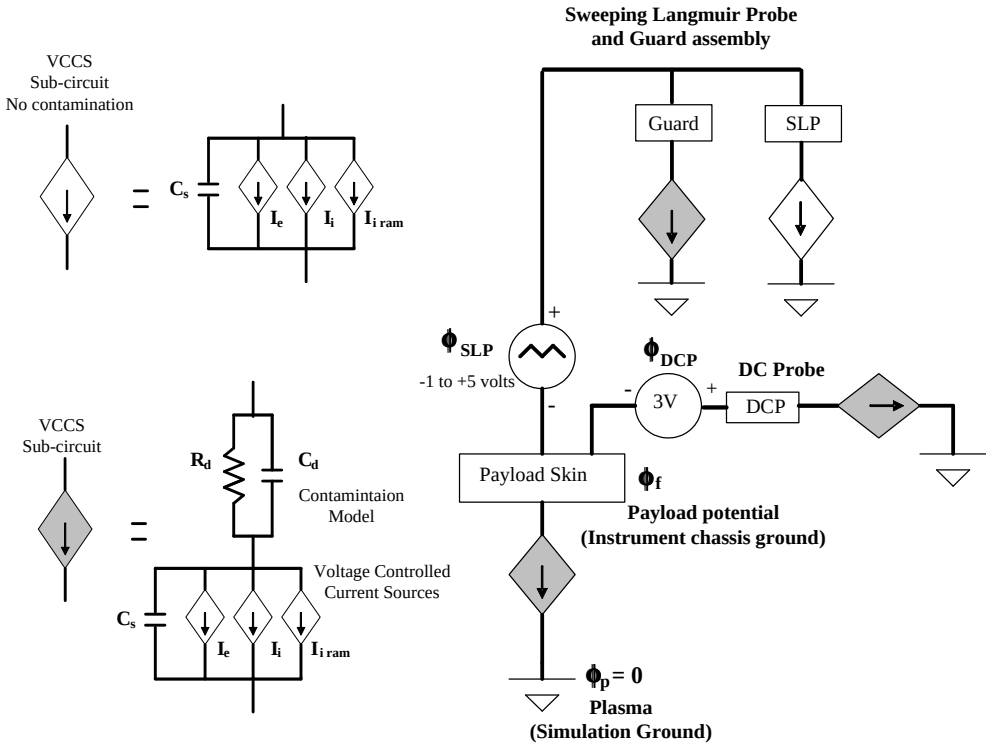

Fig. 4.3: Charging model of the payload as implemented in SPICE. On the left are two different sub-circuit models. One includes contamination effects while the other does not. The SLP which was internally heated is modeled as contamination free, but the payload skin and the DCP are modeled with contamination.

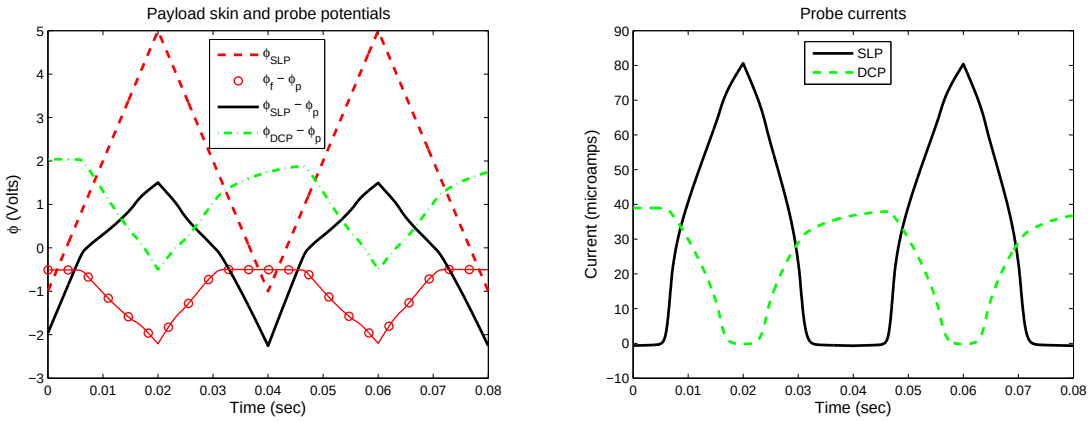

Fig. 4.4: Simulation results for the EQUIS II charging model. As the voltage applied to the SLP (ϕ_{SLP}) is swept from -1 to +5 volts relative to the payload chassis (ϕ_f), the payload floating potential charges more negative relative to the plasma potential (ϕ_p). This reduces the SLP and DCP collected currents.

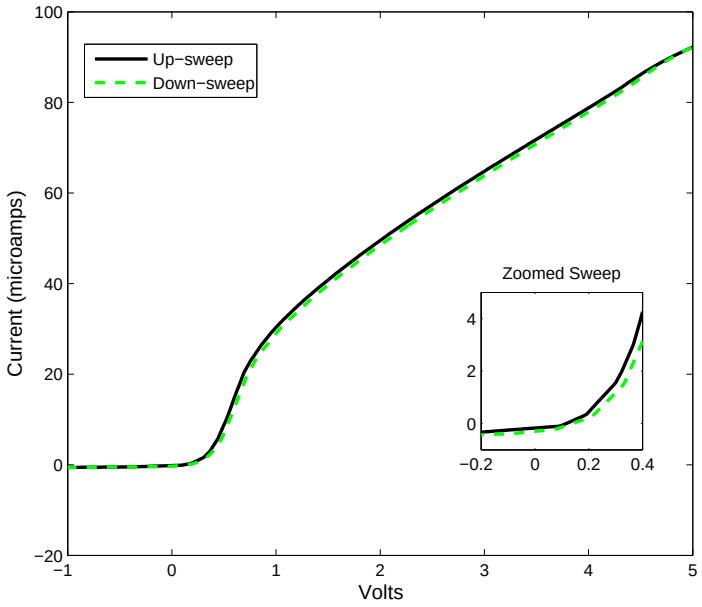

Fig. 4.5: Hysteresis in the SLP sweeps due to contamination on the payload skin.

$1100°K$, and the results are shown in figure 4.4. The simulation time span covered four SLP voltage sweeps (80 ms). The results show that while the voltage applied to the SLP (ϕ_{SLP}) varied linearly from -1 to +5 volts relative to the payload chassis ground, the variation relative to the plasma potential ($\phi_{SLP} - \phi_p$) was nonlinear. Thus, the SLP I-V curve is "warped" in the upper electron retardation region and the entire electron saturation region. As the payload charges increasingly negative, the DCP moves its operation from electron saturation to electron retardation and eventually into ion saturation. As the current by the DCP is measured only in one direction, the instrument effectively shuts off for any negative charging of the payload greater than 3 volts. The SLP and DCP currents are plotted in right column of figure 4.4. Figure 4.5 plots an overlay of SLP up-sweep and down-sweep. As the SLP was modeled clean, one would not expect any hysteresis within consecutive SLP sweeps. However, figure 4.5 shows that due to the small area ratio the contamination of the payload skin results in some minor hysteresis in the SLP data.

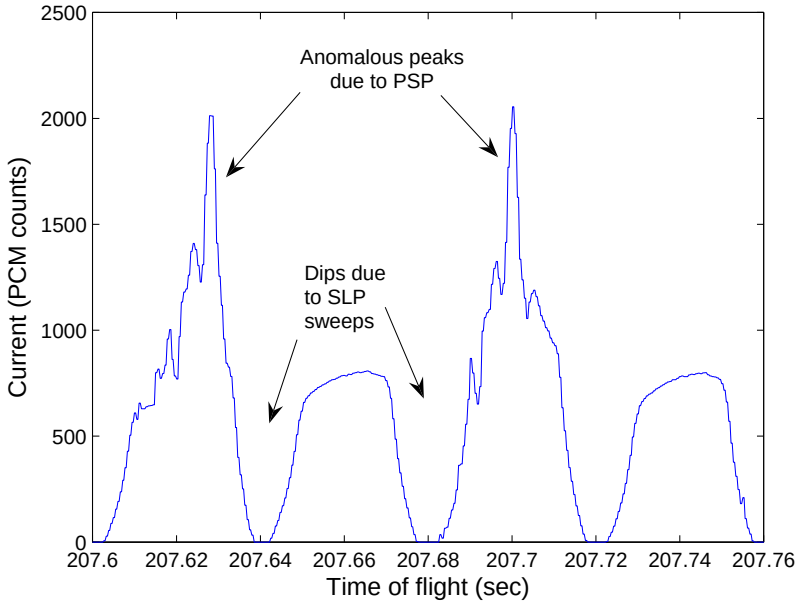

Fig. 4.6: The DCP data is affected by the SLP sweeps as well as by the PSP sweeps.

4.4 Data Analysis and Discussion

The PFP acquired a lock on the plasma upper hybrid resonance for several tens of seconds only in the upleg portion of both the rocket flights. Thus, it provided absolute electron density for several tens of kilometers in the F-region ionosphere. A widely used method to acquire density measurement for the entire flight duration is to normalize the DCP data to the PIP data, thereby providing high resolution density measurements. Figure 4.6 shows a portion of the DCP dataset. As predicted by the charging model, the DCP data was heavily influenced by the oscillations in the payload chassis ground. Furthermore, as the DCP was on the same boom as the PIP antenna, the PSP frequency sweep affected the plasma sheath around the DCP. This resulted in anomalous peaks in the DCP data whenever the PSP was operating at frequencies below the plasma upper hybrid resonance. Due to these disturbances, the DCP data is not suitable for use as a density measurement.

Another quasi-DC measurement made over the entire flight comes from the SLP by considering only a constant voltage step. Thus, the SLP can be considered as a set of low spatial resolution fixed-bias DCPs. The quasi-DC data can then be normalized to the PFP

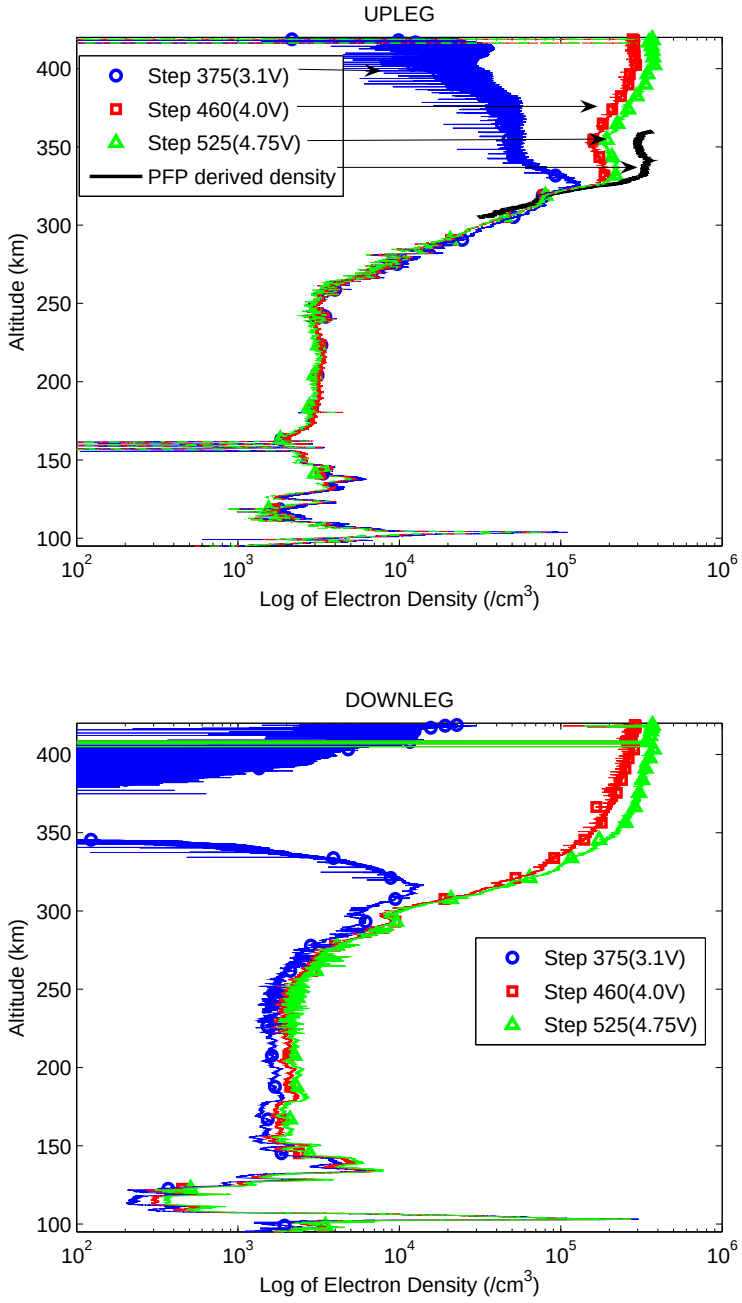

Fig. 4.7: Quasi-DC plot of the SLP data to derive relative density profile. On the upleg, where the PFP locked, the absolute density from the PFP does not match the Quasi-DC density except at 305 km, the point of normalization.

derived absolute density to get the density profile for the entire flight. Figure 4.7 shows the August 15^{th} flight's (29.037) quasi-DC data at several different voltage steps normalized to the PFP lock derived density at 305 km altitude. Similar to the DCP that was biased at +3 volts, the +3.1 volts quasi-DC data is heavily influenced by negative payload charging due to small surface-to-probe area ratio. For higher quasi-DC voltages the effect seems to be less drastic. However, it is important to note that while the normalized density below 300 km seems to be constant between different quasi-DC voltages (which is expected of fixed-bias Langmuir probe operation), the quasi-DC derived relative density profile does not exactly match the PFP derived density except at the point of normalization.

This observation brings into question the accuracy of the DCP method of relative density measurement that is used frequently on rocket flights. The premise of DCP operation is that the electron saturation current is directly proportional to density, and that the measurement is made at the same potential relative to plasma potential. In actuality, the probe is applied a potential relative to the payload chassis ground. As long as the payload chassis ground remains stable relative to the plasma potential the DCP technique works.

The problem arises due to two reasons. First, in a typical rocket flight, the plasma temperature can change by an order of magnitude within the 100-400 km altitude range. This changes the floating potential of the payload. Second, any additional current source to the payload-probe system, such as electron collection by exposed potentials or triboelectric current collection [45], will change the payload floating potential significantly. Thus, the technique of fixed-bias DCP derived relative density measurements can be prone to significant errors that are dependent upon the stability of the payload chassis ground relative to the plasma.

Of further concern is a "negative" characteristic observed in the electron saturation region of the SLP I-V curves as shown in figure 4.8. This phenomenon was observed only in the lower altitude region I-V curves. It is present in both the upleg and downleg trajectories for both of the rocket flights. It has also been seen intermittently on a cylindrical Langmuir probe aboard the International Space Station (see Chapter 3). This phenomenon

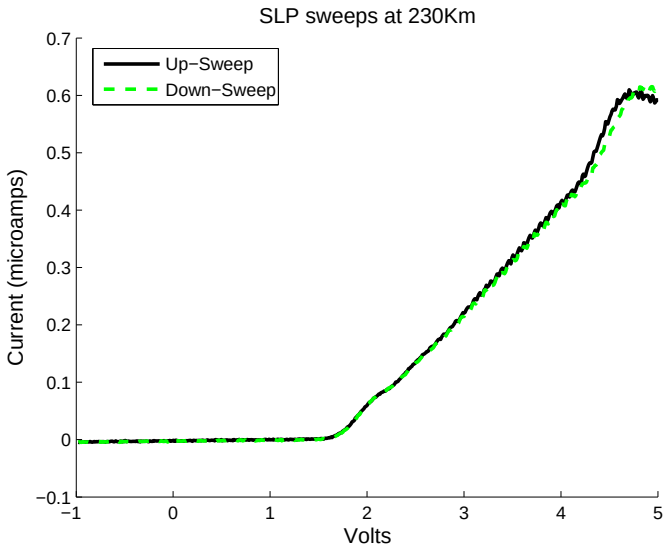

Fig. 4.8: A typical SLP up-sweep and down-sweep observed on both flights at low altitudes (< 250 km). The current shows a "negative" characteristic and drops with applied higher voltages.

occurs at the very top of the voltage sweep and thus makes suspect any DCP type relative density data obtained with large fixed-bias voltages. However, it is quite possible that these "negative" characteristic I-V curves correspond to a non-Maxwellian plasma encountered by both probes. At this time no fully satisfactory explanation for this phenomenon exists.

In the absence of a PFP lock on the upper hybrid resonance that lasts throughout the rocket flight, and of the lack of accurate calibration to make use of the PSP dataset, the only option that remains to derive accurate density profiles is to use the SLP I-V curves. Figure 4.9 shows two consecutive I-V curves of the SLP. The minor hysteresis predicted by the charging model due to payload surface contamination is evident. We counter this minor hysteresis by averaging the two consecutive sweeps. While the electron saturation region is expected to be corrupted by the "warping" of the I-V curve, the ion saturation region and the lower part of electron retardation region is expected to remain undisturbed. We thus use a modified version of the technique presented in Chapter 3 to analyze the SLP I-V curves.

The Chapter 3 technique analyzes the electron saturation region of an I-V curve to

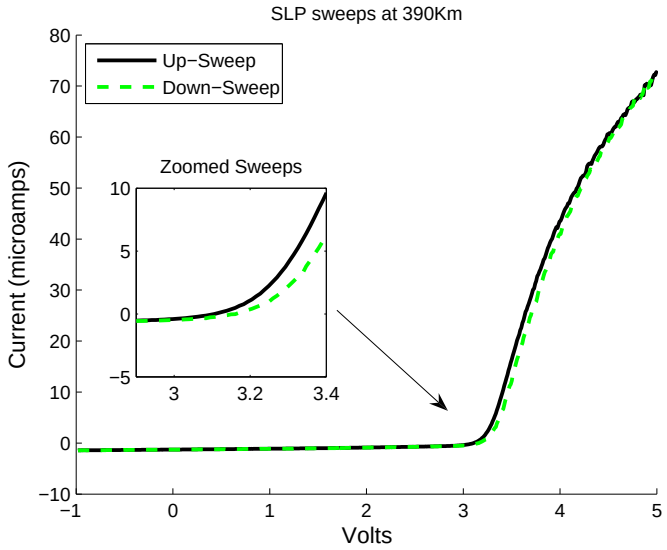

Fig. 4.9: Two consecutive SLP sweeps, at an altitude of 390 km from the 29.037 rocket upleg trajectory, showing the presence of minor hysteresis.

derive absolute electron density. We use a modified multi-step procedure to derive absolute ion density from the EQUIS II SLP I-V curves. In the first step, subtraction of a line fit to the ion saturation region from the total collected current approximately gives the electron collection current, I_e. The location of the $dI_e/d\phi$ maxima within 0.4 eV of the floating potential (ϕ_f) gives a first order approximation to the plasma potential (ϕ_p). The value of ϕ_f is determined by the point where the total collected current goes to zero. By equating the value of the ion saturation current linear fit at the location of ϕ_p to ion ram current we get a first order approximation to the ion density.

In the second step, we assume the plasma to be quasineutral ($n_i = n_e$) and do a non-linear least squares fit of the total collected current to

$$I_{total}(\phi) = -n_i e A_{ram} V_{ram} + n_e e A \sqrt{\frac{k_B T_e}{2\pi m_e}} \exp\left(\frac{e(\phi - \phi_p)}{k_B T_e}\right), \tag{4.6}$$

where the first term is the ion ram current and the second term the electron retardation current. We use the density as calculated in the first step and fit equation 4.6 in a least squares sense for only T_e and ϕ_p. The nonlinear fit is done only for points within ϕ_f-0.05

eV to ϕ_f+0.02 eV. This nonlinear fit gives a more accurate value of ϕ_p than that derived in the first step.

In the third step, we fit the ion saturation current region of the I-V curve to equation 4.4 in a least squares sense for n_i and β. In the fourth step, with the improved value of n_i and the fit value of β, we do another least squares fit for points within ϕ_f-0.05 eV to ϕ_f+0.02 eV to

$$I_{total}(\phi) = -n_i e A_{ram} V_{ram} + n_e e A \sqrt{\frac{k_B T_e}{2\pi m_e}} \exp\left(\frac{e(\phi - \phi_p)}{k_B T_e}\right) - n_i e A \sqrt{\frac{k_B T_e}{2\pi m_i}} \left(1 - \frac{e(\phi - \phi_p)}{k_B T_e}\right)^{\beta}. \tag{4.7}$$

This is similar to the second step, but the inclusion of the OML-type ion saturation current expression gives a better fit for T_e and ϕ_p. Finally, in the fifth step, we use the latest fit values of T_e and ϕ_p to recalculate step three and get the final value of n_i. The results of this multi-step iterative procedure to derive density and temperature are shown in figures 4.10 and 4.11.

The absolute density derived from the SLP I-V curves using the above multi-step procedure matches the PFP derived density for the entire duration the PFP had a lock on the plasma upper hybrid frequency. However, the density resolution at lower altitudes suffers due to lower sensitivity of the SLP to ion current. The "bumps" in the temperature profile above 250 km in both upleg and downleg trajectories of the 29.037 rocket are coincident with strong shear flow of about 190 m/s as observed in the E-field data [77]. Of most interest is the anti-correlation between density and temperature within and around the double layer sporadic-E observed on the 29.036 rocket flight. This is shown in figure 4.12. We do not have a satisfactory explanation for this phenomenon yet.

4.5 Summary and Conclusion

In this paper we have presented data from two sounding rocket payloads of the EQUIS II campaign, 29.036 and 29.037. The rockets were launched into the precursor conditions of a full-blown equatorial spread-F. The payloads carried USU built RF Plasma Impedance

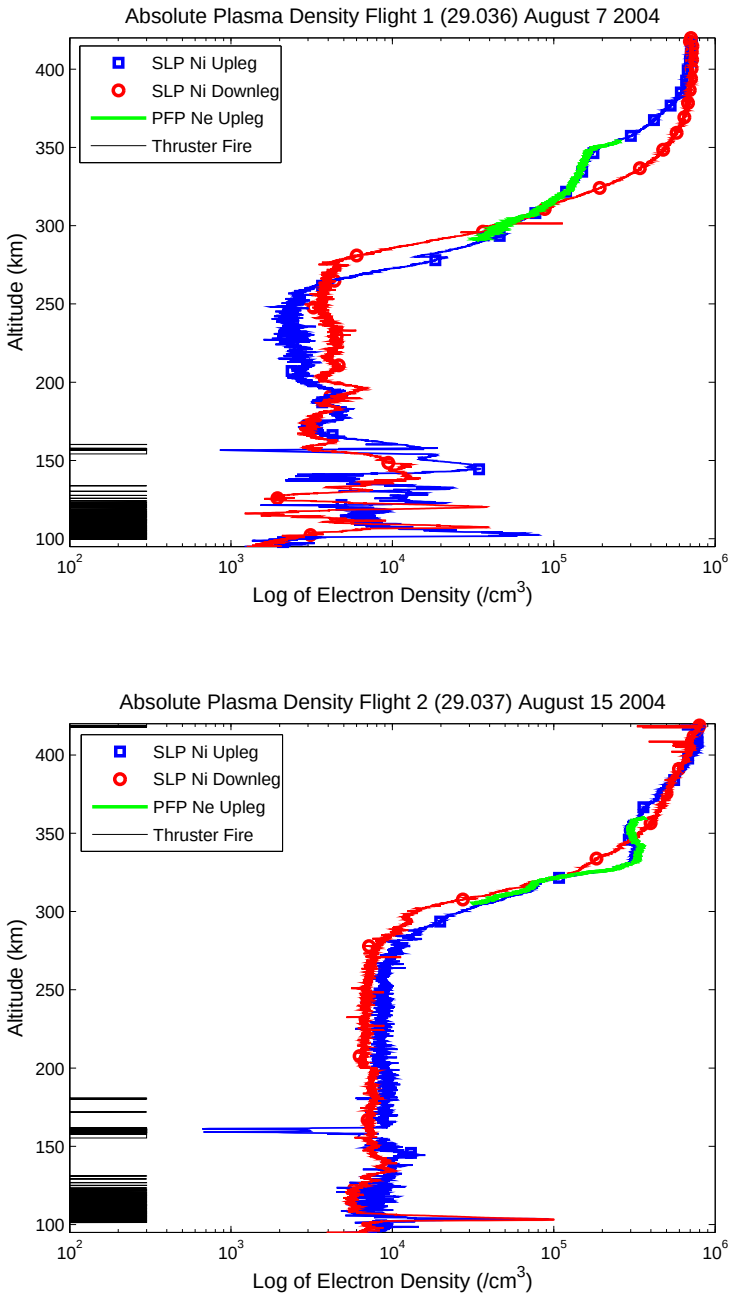

Fig. 4.10: Plasma density for both the EQUIS II (29.036 and 29.037) rocket flights.

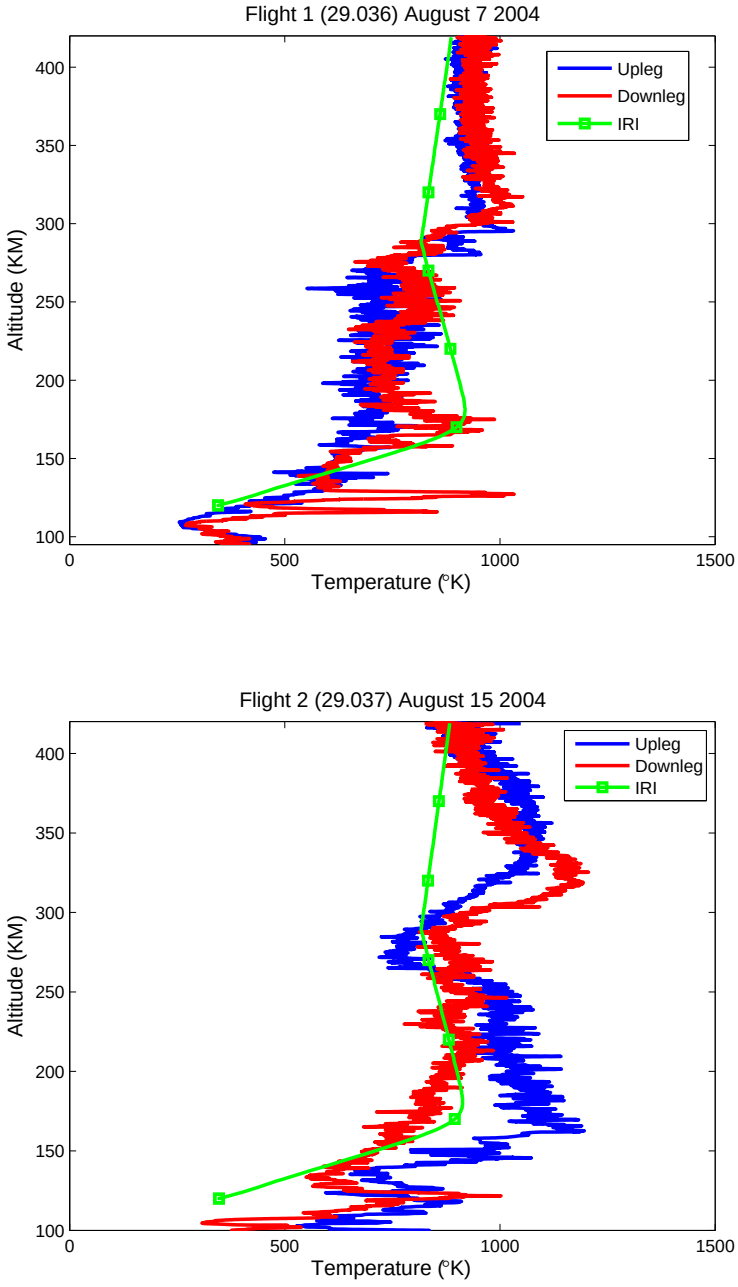

Fig. 4.11: Plasma temperatures for both the EQUIS II (29.036 and 29.037) rocket flights.

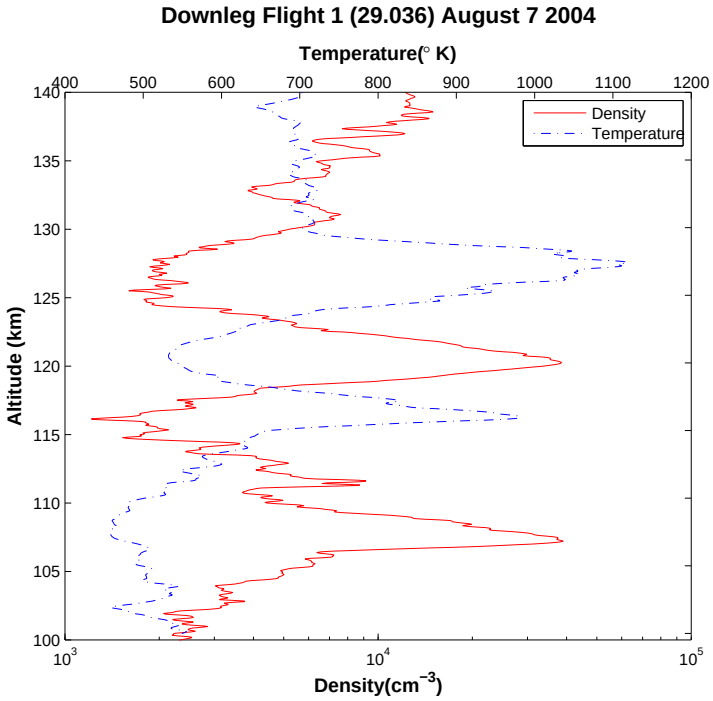

Fig. 4.12: Anti-correlation in density and temperature observed within and around double sporadic-E layer on the downleg of 29.036 rocket flight.

Probe (PIP), a fixed-bias DC Langmuir Probe (DCP) and a Sweeping Langmuir Probe (SLP). The ratio of the payload surface area to the cumulative area of the SLP and its guard was about 250. This small area ratio created problems with the return current to space plasma as the SLP swept into the electron saturation region. We have developed and presented a charging model for the entire payload and instrument combination to qualitatively understand the effect of the small area ratio on the DCP and SLP behavior. The model simulation showed significant charging of the payload skin as the SLP swept into the electron saturation region. This explained the observation of the DCP shutting off as the SLP swept into higher voltages. The simulation also showed "warping" of the SLP I-V curves in the electron saturation region, but showed the ion saturation region and the initial part of electron retardation unaffected. We then analyzed the ion saturation region using an iterative procedure to determine absolute ion density and electron temperature. The derived absolute ion density matches very well with the electron density derived from

the PIP when it locked onto to the plasma upper hybrid frequency.

The data presented in this paper has several implications. First, it shows that on small sounding rocket payloads the DCP technique of relative density measurement is not very accurate. Second, we have shown that even with a small area ratio it is possible to derive absolute plasma density and temperature from a sweeping Langmuir probe, provided that it is engineered to be sensitive enough to measure ion saturation current with high resolution. Finally, the derived density and temperature profiles for the two EQUIS II rockets have shown peculiar phenomenon both within the ionosphere as well as in instrument behavior. On the instrument side, our dataset shows a "negative" characteristic well into the electron saturation region where the collection current drops with higher applied voltage, while on the ionospheric physics side, the dataset shows the presence of density and temperature anti-correlation within and around a double layer sporadic-E. The reasons for these phenomena are still under investigation and will be discussed in a future paper.

Chapter 5

Summary and Future Work

In this chapter we first summarize the work done and the resulting conclusions for each of the three projects that are presented in this dissertation. We then conclude with some ideas for future projects.

5.1 Summary

This dissertation has consistently emphasized one thing, that although the Langmuir probe technique for in situ measurement of plasma parameters has been around for eight decades, deriving the parameters with accuracy from the data acquired by a Langmuir probe immersed in space plasma is a challenging task. Chapter 2 presented the efforts on understanding the anomalous behavior of a fixed-bias DC Langmuir probe (DCP) aboard the Sudden Atom Layer rocket payload. Its mission objective was the investigation of sporadic sodium layers that form almost explosively (rise-time in several minutes) in the Earth's mesosphere and have a full-width-half-maximum of about 1 km. Besides the DCP the payload also carried an RF Swept Impedance Probe (SIP) that measured the input impedance of an electrically short antenna over a range of applied RF frequencies. The SIP data was analyzed by comparison with Balmain's model for impedance of a short dipole antenna in magnetoplasma to derive absolute plasma density. While both the ground-based observations and the SIP saw a sporadic-E (E_s) layer at 92 km altitude, the DCP dataset did not show any signature of the E_s layer. The absence of the E_s layer in DCP data appears similar to an electron "bite-out" that has been reported to occur in the mesosphere region due to electron attachment to dust and ice particles.

In order to investigate the reasons for the anomalous behavior of DCP, we did an aerodynamic simulation of the payload to understand neutral flow in the payload vicinity,

as well as developed a charging model to understand the causes of payload charging and the resulting behavior of DCP. Consequently, we have shown that the negative charging of the payload surface due to triboelectric charge transfer from the meteoric neutral dust present in the Earth's mesosphere was the reason that the DCP did not observe the E_s layer. Although all ionospheric rockets fly through the Earth's mesosphere, our work is the first reported observation of the triboelectrification of a payload surface in this altitude region. We have then further discussed another more recent mesospheric sounding rocket campaign that USU was not involved with and presented the possibility of those payloads charging via triboelectrification in order to explain their observed DCP dataset. In conclusion, the work on the Sudden Atom Layer project has clearly indicated the importance of considering the effects of triboelectrification on the interpretation of Langmuir type probe datasets in the presence of dusty plasma, such as seen in the Earth's mesosphere.

In Chapter 3 we presented the first data analysis results of the Floating Potential Measurement Unit (FPMU) instrument suite that is deployed aboard the International Space Station (ISS). The FPMU was deployed to closely monitor the ISS charging levels as new solar panels are added to the ISS assembly and the structure grows towards its full size. Severe charging of the ISS is a hazard for astronauts on Extra Vehicular Activity, and any resultant surface arcing can lead to functional anomalies and surface degradation on the ISS. All of the three Langmuir probe instruments (FPP, WLP, and NLP) provided the ISS floating potential value to within ± 2 volts of each other, thus fulfilling NASA's requirement of FPMU.

However, the unique and remarkable achievement of the FPMU is that it provides a doubly redundant measurement of ionospheric plasma density and temperature from two different geometries of Langmuir probe that agree to within $\pm 10\%$. These in situ measurements can now be used as an input for the ISS charging model and for the validation of USU-GAIM model. A technique was developed to derive absolute electron density from the electron saturation region of the I-V curves in a mesothermal magnetized plasma. The accuracy of the procedure is evident as the derived electron density values agree well between

the WLP and the NLP, as well as with the results from the USU-GAIM and IRI ionospheric models. The first results presented in this paper show that the in situ density measurements agree better with USU-GAIM than with IRI.

Chapter 4 presented the dataset from two separate sounding rockets of the EQUIS II campaign launched into thin radar scattering layers which were observed as precursors to nighttime Equatorial Spread-F. The EQUIS II payloads carried an RF Plasma Impedance Probe (PIP) and a DCP on one axial boom, and an internally heated Sweeping Langmuir Probe (SLP) that was guarded on one side on a second axial boom. The ratio of the payload surface area to the cumulative area of the SLP and its guard was about 250. This small area ratio led to negative charging of the rocket payload as the SLP swept into the electron saturation region. We have developed and presented a charging model for the entire payload and instrument combination. The model simulation explained the observation of the DCP shutting off as the SLP swept into higher voltages, and also showed "warping" of the SLP I-V curves in the electron saturation region while the ion saturation region and the initial part of electron retardation remained unaffected. We then analyzed the ion saturation region using an iterative procedure, similar to the FPMU data analysis, to determine absolute ion density and temperature. The derived absolute ion density matched very well with the absolute electron density derived from the PIP when it locked onto to the plasma upper hybrid frequency in the lower F-region ionosphere.

The data analysis efforts on the EQUIS II dataset showed that on small sounding rocket payloads the DCP technique of relative density measurement is not very accurate. A more important conclusion was that even with a small surface-to-probe area ratio it is possible to derive absolute plasma density and temperature from a sweeping Langmuir probe, provided the instrument is sensitive enough to measure ion saturation current with high resolution.

5.2 Future Work

The work on the SAL dataset has indicated the importance for considering the effects of triboelectrification on the interpretation of Langmuir-type probe datasets in the presence of dusty plasma. However, the triboelectric current from neutral dust or neutral meteoric

smoke particles (MSP) to a DCP can also be used to determine a crude estimate of the particles' number density and their primary metallic content.

It has been estimated that between 10 to 100 tons of meteoric material enters the Earth's atmosphere every day. The meteoric material evaporates upon high speed entry, settles and is distributed over a variety of particle sizes ranging from neutral metallic atoms and metal ions, to neutral and charged MSP. The existence of neutral and ionized metal layers in the Mesosphere-Lower Thermosphere (MLT) region is well known and has been observed with ground-based instruments like radar and lidar. Recently, heavier charged dust particles have also been observed using in situ instrumentation [38, 67]. However, the neutral MSP have never been observed in situ or by ground based observations, although their number densities have been proposed by models [66, 78] and are widely accepted in the science community. Further, this material is thought to be extremely important to the dynamics and chemistry of the MLT by providing the seeds for enhanced radar echoes from the polar summer mesosphere region (PMSE) and noctilucent clouds (NLC). The observations of sporadic metal layers at altitude above 100 km could also imply the adsorption of unoxidized metals on the smoke particle surface. Thus, any instrument that can provide in situ observations of the MSP density and composition will be of significant value to the science community.

If two surfaces come merely in contact with each other and then separate, the surface with lower work function loses an electron to the surface with higher work function [16]. Based on this simple principle of triboelectric charge transfer we present here an idea for a new measurement technique that utilizes fixed-bias Langmuir probes to approximately determine the density and the primary constituent of the meteoric smoke at the instance of the payload passage. Figure 5.1 shows a conceptual layout of such an instrument suite designed primarily to detect neutral iron metal content of the MSP. The instrument suite consists of three DCPs, all of which are heated to keep their surfaces clean. The instrument suite should ideally be mounted on a boom extending far out from the any payload wake. The three DCPs will have their surfaces coated with materials that have different work

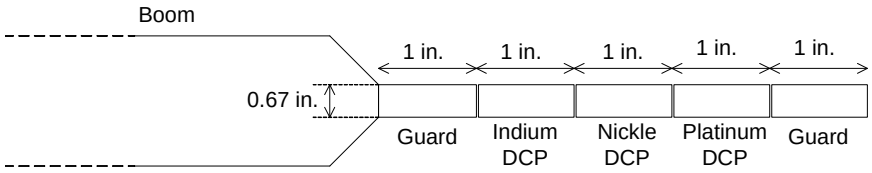

Fig. 5.1: An instrument suite of three DCPs with different metal coatings on their surface.

functions, ϕ_{wk}: platinum 111 ($\phi_{wk} = 5.9$ eV), nickle 110 ($\phi_{wk} = 5$ eV), and indium ($\phi_{wk} = 4.1$ eV). The DCPs will be biased +3 volts relative to the payload skin. These cylindrical probes are to be mounted on a 7-bore-hole extruded alumina rod that can be internally heated using a nichrome wire.

The triboelectric current to a surface passing through a dusty environment is given by $I = eNAV_{ram}$, where e is the unit elementary charge (electron) transfer between two surfaces, N is the density of the smoke/dust particles, A is the cross section area, and V_{ram} is the velocity of the surface passing through the dusty environment. Assuming the metallic composition of dust to be similar to that in meteorites [59,60], the smoke particles will most probably be composed of potassium ($\phi_{wk} = 2.29$ eV), sodium ($\phi_{wk} = 2.36$ eV), calcium ($\phi_{wk} = 2.87$ eV), magnesium ($\phi_{wk} = 3.66$ eV), and iron ($\phi_{wk} = 4.67$ eV). All oxidized metals behave, as far as contact charging is concerned, like a different metal with a work function equal to the depth of the acceptor levels in the adsorbed oxygen, which is about 5.5 eV and is largely independent of the nature of the metal [61,62]. Although most of the constituents in the neutral MSP will be oxidized, the observations of sporadic metal layers (eg. iron layers) could also imply the adsorption of unoxidized metals on the smoke particle surface. This hypothesis can be tested by noting the difference in triboelectric current among the three DCPs. The various metallic components of dust can be divided into two categories, one with $\phi_{wk} < 4.1$ eV, and the other with 4.1 eV $< \phi_{wk} <$ 5.5 eV. The presence of unoxidized iron, as a primary metallic constituent adsorbed on the smoke particles, will lead to deposition of electrons on the nickel-coated DCP and the acceptance of electrons from the indium-coated DCP. This difference in triboelectric current will help us determine the neutral smoke particle density that is carrying unoxidized iron atoms. The presence

of unoxidized metals with work function lower than 4.1 eV can be detected by little or no difference in triboelectric current to the nickel- and indium-coated DCPs. The triboelectric current to the platinum-coated DCP will give us total neutral smoke particle density as even the oxidized particles will leave an electron on the high work function platinum DCP. The spacecraft payload will also be required to carry an RF impedance probe to determine the background absolute plasma density so that the current to the DCPs can be differentiated between thermal current and triboelectric charge transfer current.

The FPMU and EQUIS II datasets open up a few questions regarding Langmuir probe physics and behavior. First, both the datasets show I-V curves that have a "negative" characteristic in the electron saturation region for a cylindrical probe that is not well understood. While the FPMU-NLP sees this phenomenon only intermittently, the "negative" characteristic is prominently visible in low altitude regions during upleg and downleg of both the EQUIS II payloads. Second, from both the datasets we have derived absolute plasma density utilizing OML-type equations, fitting for density and β. The value of beta varies in a seemingly random fashion between 0.5 and 1.0. This variation in β is most likely the result of anisotropic potential distribution around the probe due to plasma wake effects. Additional work on both these datasets addressing these questions will bring unique insight into Langmuir probe behavior. Furthermore, the derived density and temperature profiles during the EQUIS II campaign have also shown the presence of density and temperature anti-correlation within and around a double layer sporadic-E. More work needs to be done in order to understand this phenomenon.

Finally, the charging model developed in the course of this dissertation is a powerful tool to simply and easily simulate the charging dynamics of a spacecraft. Although OML equations were used to model the collection current, other equations can also be used as the understanding of probe physics progresses. While mesothermal effects are easily incorporated into the model, it will be interesting to see if rudimentary wake effects as well as magnetic field effects can be incorporated as well.

References

[1] F. J. Rich and S. Basu, "Ionospheric physics," in *Handbook of Geophysics and the Space Environment*, A. Jursa, Ed. New York: Air Force Geophysics Laboratory, 1985, ch. 9.

[2] R. W. Schunk and A. F. Nagy, *Ionospheres- Physics, Plasma Physics, and Chemistry*, ser. Atmospheric and Space Science Series. Cambridge: Cambridge University Press, 2000.

[3] D. Bilitza, W. R. Hoegy, L. H. Brace, and R. F. Theis, "Evaluation of the International Reference Ionosphere with the large AE-C and DE2 databases," *Advances in Space Research*, vol. 8, no. 4, p. 209, 1988.

[4] L. Scherliess, R. W. Schunk, J. J. Sojka, D. C. Thompson, and L. Zhu, "Utah State University Global Assimilation of Ionospheric Measurements Gauss-Markov Kalman Filter model of the ionosphere: Model description and validation," *Journal of Geophysical Research*, vol. 111, A11315, doi:10.1029/2006JA011712, 2006.

[5] I. Langmuir and H. M. Mott-Smith, "Studies of electric discharges in gas at low pressures," *General Electric Review*, p. 616, 1924.

[6] H. M. Mott-Smith and I. Langmuir, "The theory of collectors in gaseous discharges," *Physical Reviews*, vol. 28, p. 727, 1926.

[7] L. H. Brace, "Langmuir probe measurements in the ionosphere," in *Measurement Techniques in Space Plasmas: Particles*, ser. Geophysical Monograph Series, R. F. P. et al., Ed. Washington, D.C.: American Geophysical Union, 1998, vol. 102, pp. 23–35.

[8] D. C. Ferguson, B. Hillard, and T. L. Morton, "The Floating Potential Probe (FPP) for ISS: Operations and initial results," in *7th Spacecraft Charging Technology Conference at ESTEC, Noordwijk, The Netherlands, ESA SP-476*, R. A. Harris, Ed., p. 3655, 2001.

[9] F. F. Chen, "Electric probes," in *Plasma Diagnostic Techniques*, R. Huddlestone and S. Leonard, Eds. New York: Academic Press, 1965, pp. 113–200.

[10] F. F. Chen, *Plasma Physics and Controlled Fusion*. New York: Plenum Press, 1984.

[11] L. H. Brace and R. F. Theis, "The cylindrical electrostatic probes for Atmospheric Explorer -C, -D, and -E," *Radio Science*, vol. 8, no. 4, p. 341, 1973.

[12] L. Schott, "Electrical probes," in *Plasma Diagnostics*, W. Lochte-Holtgreven, Ed. New York: AIP Press, 1995, pp. 668–731.

[13] N. Hershkowitz, "How Langmuir probes work," in *Plasma Diagnostics*, O. Auciello and D. Flamm, Eds. New York: Academic Press, 1989, vol. 1, pp. 113–184.

[14] J. D. Swift and M. J. R. Schwar, *Electrical Probes for Plasma Diagnostics*. London: Iliffe Books, 1970.

[15] D. Hastings and H. Garrett, *Spacecraft-Environment Interactions*, ser. Cambridge Atmospheric and Space Science Series. Cambridge: Cambridge University Press, 1996.

[16] W. R. Harper, *Contact and Frictional Electrification*, ser. Monographs on the Physics and Chemistry of Materials. London: Oxford University Press, 1967.

[17] J. Lowell, "Contact electrification of metals," *Journal of Physics D: Applied Physics*, vol. 8, p. 53, 1975.

[18] C. Stow, "Dust and sand storm electrification," *Weather*, vol. 24, no. 4, pp. 134–140, 1969.

[19] A. K. Kamra, "Measurements of electrical properties of dust storms," *Journal of Geophysical Research*, vol. 77, no. 30, pp. 5856–5869, 1972.

[20] W. R. Hoegy and L. E. Wharton, "Current to a moving cylindrical electrostatic probe," *Journal of Applied Physics*, vol. 44, no. 12, p. 5365, 1973.

[21] I. Katz, G. Jongeward, V. Davis, T. Morton, and D. Ferguson, "Current collection by a large Langmuir probe in a mesothermal (ram) plasma," in *Measurement Techniques in Space Plasmas: Particles*, ser. Geophysical Monograph Series., R. F. P. et al., Ed. Washington, D.C.: AGU, 1998, vol. 102, pp. 37–41.

[22] A. Piel, M. Hirt, and C. T. Steigies, "Plasma diagnostics with Langmuir probes in the equatorial ionosphere: I. The influence of surface contamination," *Journal of Physics D: Applied Physics*, vol. 34, pp. 2643–2649, 2001.

[23] J. Rubinstein and J. G. Laframboise, "Theory of a spherical probe in a collisionless magnetoplasma," *Physics of Fluids*, vol. 25, p. 1174, 1982.

[24] L. W. Parker and B. L. Murphy, "Potential buildup on an electron-emitting ionospheric satelite," *Journal of Geophysical Research*, vol. 72, p. 1631, 1967.

[25] W. B. Thompson, "Preliminary investigation of the electrodynamics of a conducting tether," in *Spacecraft Environmental Interactions Technology, AFGL-TR-85-0018/NASA Conf. Publ. 2359*, C. Purvis and C. Pike, Eds., pp. 649–662, 1983.

[26] J. G. Laframboise and L. J. Sonmor, "Current collection by probes and electrodes in space magnetoplasmas: A review," *Journal of Geophysical Research*, vol. 98, p. 337, 1993.

[27] J. R. Sanmartin, "Theory of a probe in a strong magnetic field," *Physics of Fluids*, vol. 13, p. 103, 1970.

[28] I. Katz, G. Jongeward, V. Davis, M. Mandell, R. Kuharski, J. Lilley, W. Raitt, D. Cooke, R. Torbert, G. Larson, and D. Rau, "Structure of the bipolar plasma sheath generated by SPEAR I," *Journal of Geophysical Research*, vol. 94, no. A2, p. 1450, 1989.

[29] K. I. Oyama, "A systematic investigation of several phenomena associated with contaminated Langmuir probes," *Planetary and Space Science*, vol. 24, p. 183, 1976.

[30] M. Wahlstrm, E. Johansson, E. Veszelei, P. Bennich, M. Olsson, and S. Hogmark, "Improved Langmuir probe surface coatings for the Cassini satellite," *Thin Solid Films*, vol. 220, p. 315, 1992.

[31] W. E. Amatucci, P. W. Schuck, D. N. Walker, P. M. Kintner, S. Powell, B. Holbeck, and D. Leonhardt, "Contamination-free sounding rocket Langmuir probe," *Reviews of Scientific Instruments*, vol. 72, no. 4, p. 2052, 2001.

[32] W. E. Amatucci, M. E. Koepke, T. E. Sheridan, M. J. Alport, and J. J. C. III, "Self cleaning Langmuir probe," *Reviews of Scientific Instruments*, vol. 64, no. 5, p. 1253, 1993.

[33] D. Strele, M. Koepke, R. Schrittweiser, and P. Winkler, "Simple heatable Langmuir probe for alkali plasmas," *Reviews of Scientific Instruments*, vol. 68, no. 10, p. 3751, 1997.

[34] E. P. Szuszczewicz, "Area influences and floating potentials in Langmuir probe measurements," *Journal of Applied Physics*, vol. 43, no. 3, p. 874, 1972.

[35] W. Sanderson, "The history and dynamics of the Plasma Impedance Probe," Master's thesis, ECE Dept., Utah State University, Logan, 2007.

[36] K. G. Balmain, "The impedance of a short dipole antenna in a magnetoplasma," *IEEE Transactions on Antennas and Propagation*, vol. AP-12, p. 605, 1964.

[37] K. G. Balmain, "Dipole admittance for magnetoplasma diagnostics," *IEEE Transactions on Antennas and Propagation*, vol. AP-17, p. 389, 1969.

[38] L. G. Gelinas, K. A. Lynch, M. C. Kelley, S. Collins, S. Baker, Q. Zhou, and J. S. Friedman, "First observation of meteoric charged dust in the tropical mesosphere," *Geophysical Research Letters*, vol. 25, no. 21, pp. 4047–4050, 1998.

[39] J. H. Hecht, S. Collins, C. Kruschwitz, M. C. Kelley, R. G. Roble, and R. L. Walterscheid, "The excitation of the Na airglow from COQUI DOS rocket and ground based observations," *Geophysical Research Letters*, vol. 27, no. 4, pp. 453–456, 2000.

[40] M. C. Kelley and L. G. Gelinas, "Gradient drift instability in midlatitude sporadic E layers: localization of physical and wavenumber space," *Geophysical Research Letters*, vol. 27, no. 24, pp. 457–460, 2000.

[41] C. Fish, "Design, development, test, and calibration of the Floating Potential Measurement Unit sensor suite," Master's thesis, ECE Dept., Utah State University, Logan, 2005.

[42] C. Carlson, "Next generation Plasma Frequency Probe instrumentation technique," Master's thesis, ECE Dept., Utah State University, Logan, 2004.

[43] O. Morales, "Digital design for a Sweeping Langmuir Probe," Master's thesis, ECE Dept., Utah State University, Logan, 2004.

[44] S. Humphries, "Calibration and results of the EQUIS II Plasma Impedance Probe," Master's thesis, ECE Dept., Utah State University, Logan, 2005.

[45] A. Barjatya and C. M. Swenson, "Observations of triboelectric charging effects on Langmuir-type probes in dusty plasma," *Journal of Geophysical Research*, vol. 111, A10302, doi:10.1029/2006JA011806, 2006.

[46] H. B. Garrett and A. C. Whittlesey, "Spacecraft charging, an update," *IEEE Transactions on Plasma Science*, vol. 28, no. 6, pp. 2017–2028, 2000.

[47] P. K. Shukla and A. A. Mamun, *Introduction to Dusty Plasma Physics.* London: IoP Publishing Ltd, 2002.

[48] U. von Zahn, P. von der Gathen, and G. Hansen, "Forced release of sodium from upper atmospheric dust particles," *Geophysical Research Letters*, vol. 14, pp. 76–79, 1987.

[49] W. J. Heikkila, N. Eaker, J. A. Fejer, and K. R. Tipple, "Comparison of several probe techniques for ionospheric electron concentration measurements," *Journal of Geophysical Research*, vol. 73, no. 11, pp. 3511–3535, 1968.

[50] K. G. Balmain and G. A. Oksiutik, "RF probe admittance in the ionosphere: Theory and experiment," in *Plasma Waves in Space and in the Laboratory*, J. Thomas and B. Landmark, Eds. New York: American Elsevier, 1969, vol. 1, pp. 247–261.

[51] K. D. Baker, J. Labelle, R. F. Pfaff, L. C. Howlett, N. B. Rao, J. C. Ulwick, and M. C. Kelley, "Absolute electron density measurements in the equatorial ionosphere," *Journal of Atmospheric and Terrestrial Physics*, vol. 47, p. 781, 1985.

[52] C. T. Steigies, D. Block, M. Hirt, B. Hipp, A.Piel, and J. Grygorczuk, "Development of a fast impedance probe for absolute electron density measurements in the ionosphere," *Journal of Physics D: Applied Physics*, vol. 33, pp. 405–413, 2000.

[53] P. M. Banks and G. Kockarts, *Aeronomy.* New York: Academic Press, 1973, vol. Part A.

[54] L. G. Gelinas, *An in situ measurement of charged mesospheric dust during a sporadic atom layer event.* Ph.D. dissertation, University of New Hampshire, Durham, 1999.

[55] J. Keown, *OrCAD PSpice and Circuit Analysis*, 4th ed. New Jersey, NJ: Prentice Hall, 2001.

[56] G. D. Earle, T. J. Kane, R. F. Pfaff, and S. R. Bounds, "Ion layer separation and equilibrium zonal winds in midlatitude sporadic E," *Geophysical Research Letters*, vol. 27, no. 4, pp. 461–464, 2000.

[57] P. A. Roddy, G. D. Earle, C. M. Swenson, C. G. Carlson, and T. W. Bullett, "Relative concentrations of molecular and metallic ions in midlatitude intermediate and sporadic-E layers," *Geophysical Research Letters*, vol. 31, L19807, doi:10.1029/2004GL020604, 2004.

[58] R. Godard and J. Laframboise, "Total current to cylindrical collectors in collisionless plasma flow," *Planetary and Space Science*, vol. 31, no. 3, pp. 275–283, 1983.

[59] J. M. C. Plane, "A new time-resolved model of the mesospheric Na layer: constraints on the meteor input function," *Atmos. Chem. Phys. Discuss.*, vol. 4, pp. 39–69, 2004.

[60] W. J. McNeil, E. Murad, and J. M. C. Plane, "Models of meteoric metals in the atmosphere," in *Meteors in the Earth's Atmosphere*, E. Murad and I. P. Williams, Eds. Cambridge: Cambridge University Press, 2002, pp. 265–287.

[61] N. Cabrera and N. F. Mott, "Theory of the oxidation of metals," *Reports on Progress in Physics*, vol. 12, pp. 163–184, 1949.

[62] Z. Sternovsky, M. Horanyi, and S. Robertson, "Charging of dust particles on surfaces," *Journal of Vacuum Science and Technology*, vol. 19, no. 5, pp. 2533–2541, 2001.

[63] G. A. Bird, *Molecular Dynamics and the Direct Simulation of Gas Flows*. New York: Oxford Univ. Press, 1994.

[64] Z. Sternovsky, R. H. Holzworth, M. Horanyi, and S. Robertson, "Potential distribution around sounding rockets in mesospheric layers with charged aerosol particles," *Geophysical Research Letters*, vol. 31, L22101, doi:10.1029/2004GL020949, 2004.

[65] U. von Zahn and T. Hansen, "Sudden neutral sodium layers: a strong link to sporadic-E layers," *Journal of Atmospheric and Terrestrial Physics*, vol. 50, pp. 93–104, 1988.

[66] D. M. Hunten, R. P. Turco, and O. B. Toon, "Smoke and dust particles of meteoric origin in the Mesosphere and Stratosphere," *Journal of Atmosspheric Science*, vol. 37, pp. 1342–1357, 1980.

[67] L. G. Gelinas, K. A. Lynch, M. C. Kelley, R. L. Collins, M. Widholm, E. MacDonald, J. Ulwick, and P. Mace, "Mesospheric charged dust layer: Implications for neutral chemistry," *Journal of Geophysical Research*, vol. 110, A01310, doi:10.1029/2004JA010503, 2005.

[68] R. Mikatarian, H. Barsamian, J. Kern, S. Koontz, and J. F. Roussel, "Plasma charging of the International Space Station," in *53rd International Astronautical Congress The World Space Congress, Houston, Texas*, pp. IAC–02–T.2.05, 2002.

[69] T. Dote and H. Amemiya, "Negative characteristic of a cylindrical probe in a magnetic field," *Journal of Physical Society of Japan*, vol. 19, no. 10, p. 1915, 1964.

[70] A. Barjatya, C. M. Swenson, and D. Hysell, "Observations of non-Maxwellian plasma in the bottom-type scattering layer precursor to equatorial spread-F," in *AGU Fall Meeting, San Francisco, California*, 2005.

[71] J. E. Jackson and J. A. Kane, "Measurement of ionospheric electron densities using an RF probe technique," *Journal of Geophysical Research*, vol. 64, p. 1074, 1959.

[72] R. H. Bishop, *Antenna impedance in the lower ionosphere*. Ph.D. dissertation, University of Utah, Salt Lake City, 1970.

[73] J. Ward, C. Swenson, and C. Furse, "The impedance of a short dipole antenna in a magnetized plasma via a finite difference time domain model," *IEEE Transactions on Antennas and Propagation*, vol. 53, no. 8, pp. 2711–2718, 2005.

[74] COSPAR and URSI, "International Reference Ionosphere Home Page," [http://modelweb.gsfc.nasa.gov/ionos/iri.html], 2001.

[75] D. C. Ferguson, G. B. Hillard, T. L. Morton, and R. Peterson, "ISS FPP ionospheric electron density and temperature measurements - results, comparison with the IRI-90 model, and implications for ISS charging," in *41st Aerospace Sciences Meeting and Exhibit, Reno, Nevada*, pp. AIAA–2003–1083, 2003.

[76] R. L. F. Boyd, *Space Physics: The Study of Plasmas in Space.* Oxford: Clarendon Press, 1974.

[77] D. L. Hysell, M. F. Larsen, C. M. Swenson, A. Barjatya, T. F. Wheeler, M. F. Sarango, R. F. Woodman, and J. L. Chau, "Onset conditions for equatorial spread-F determined during EQUIS II," *Geophysical Research Letters*, vol. 32, L24104, doi:10.1029/2005GL024743, 2005.

[78] M. Rapp, B. Strelnikov, S. Wilms, F.-J. Lubken, J. Gumbel, and H. Henkel, "A new detector for the in situ measurement of meteoric dust particles in the middle atmosphere," in *Proceedings of the 16th ESA symposiumon European Rocket and Balloon Programmes and Related Research, St. Gallen, Switzerland (ESA SP-530)*, B. Warmbeina, Ed., pp. 379–384, 2003.

Appendix

AGU Article Republication Release

We are pleased to grant permission for the use of the material requested for inclusion in your thesis. The following non-exclusive rights are granted to AGU authors:

- All proprietary rights other than copyright (such as patent rights).
- The right to present the material orally.
- The right to reproduce figures, tables, and extracts, appropriately cited.
- The right to make hard paper copies of all or part of the paper for classroom use.
- The right to deny subsequent commercial use of the paper.

Further reproduction or distribution is not permitted beyond that stipulated. The copyright credit line should appear on the first page of the article or book chapter. The following must also be included, "Reproduced by permission of American Geophysical Union." To ensure that credit is given to the original source(s) and that authors receive full credit through appropriate citation to their papers, we recommend that the full bibliographic reference be cited in the reference list. The standard credit line for journal articles is: "Author(s), title of work, publication title, volume number, issue number, page number(s), year. Copyright [year] American Geophysical Union."

If an article was placed in the public domain, in which case the words "Not subject to U.S. copyright" appear on the bottom of the first page or screen of the article, please substitute "published" for the word "copyright" in the credit line mentioned above.

Copyright information is provided on the inside cover of our journals. For permission for any other use, please contact the AGU Publications Office at AGU, 2000 Florida Ave., N.W., Washington, DC 20009.

Michael Connolly

Journals Publications Specialist

American Geophysical Union

Vita

Published Journal Articles

- Barjatya, A., and C.M. Swenson (2006), Observations of triboelectric charging effects on Langmuir type probes in dusty plasma, *J. Geophys. Res., 111*, A10302, doi:10.1029/2006JA011806.

- Hysell D.L., M.F. Larsen, C.M. Swenson, A. Barjatya, T.F. Wheeler, M.F. Sarango, R.F. Woodman, J.L. Chau, D. Sponseller (2006), Rocket and radar investigation of background electrodynamics and bottom-type scattering layers at the onset of equatorial spread-F, *Annales Geophysicae, 24*, 5, 1387-1400.

- Hysell D.L., M.F. Larsen, C.M. Swenson, A. Barjatya, T.F. Wheeler, M.F. Sarango, R.F. Woodman, J.L. Chau (2005), Onset conditions for equatorial spread-F determined during EQUIS II, *Geophys. Res. Lett., 32*, L24104, doi:10.1029/2005GL024743.